UNIVERSITÀ
DEGLI STUDI
DI PADOVA

University of Padova
Department of Industrial Engineering DII
Faculty of Energy Engineering

Master thesis

Determination of the pressure distribution in the volute of a centrifugal compressor with CFD

Supervisor
Prof. Ing. Giorgio Pavesi (Università di Padova)
Co-supervisor
Dr.-Ing. Sebastian Schuster (Universität Duisburg-Essen)

Candidate
Lorenzo Cerato - 2041623

Academic Year 2022 - 2023

Acknowledgements

First and foremost, I wish to express my gratitude to my academic supervisors, Prof. Giorgio Pavesi and Prof. Dieter Brillert, for granting me the opportunity to pursue this thesis work at the University of Duisburg-Essen.
Additionally, I am also thankful to my co-supervisor Dr.-Ing. Sebastian Schuster for his support and guidance throughout the entire course of my thesis.
I extend my sincere thanks to all the colleagues at the Chair of Turbomachinery for their kindness and assistance. I truly appreciate the knowledge and insight they shared with me, which have significantly contributed to the achievement of my project's goals.

I am deeply appreciative of my family for their unwavering support, love, and belief in my abilities. Your understanding during the most challenging phases of this journey has been a constant source of strength. I could not have asked for a more supportive family.

To my friends, who provided emotional support, encouragement, and understanding throughout this academic endeavor, I extend my heartfelt thanks.

To everyone who has contributed to this academic achievement, I'm truly thankful. Your support has been invaluable, and I am profoundly grateful.

Grazie.

Padova, October 2023

Lorenzo Cerato

Lorenzo Cerato

Abstract

This study aims to develop a Computational Fluid Dynamics (CFD) configuration for the analysis of pressure fluctuations within the volute of a centrifugal compressor. The initial phase of the CFD analysis involved the concurrent use of Ansys® CFX and TRACE, followed by exclusive employment of CFX for the final computations. The reference compressor utilized for this investigation is the Demag® KG3.32, and all comparative assessments were conducted based on measurements acquired in the laboratory of the University of Duisburg-Essen.

The numerical model underwent development in three primary stages, commencing with the simplified geometry of the single-passage impeller and culminating in the full 360°domain encompassing the complete impeller and the volute.

Initially, a comparative evaluation was performed between the performance characteristics of the CFD model and the experimental data. Discrepancies observed in this comparison were predominantly attributed to uncertainties stemming from the geometric representation within the CFD model.

Subsequently, an unsteady time-resolved simulation was executed across the entire domain to detect pressure fluctuations occurring within the volute. Numerous monitoring points were strategically positioned within the volute to analyze the pressure distribution. Following this, analogous monitoring was conducted within the impeller to explore the interactions between the two components. The recorded pressure signals were subjected to analysis in both the time and frequency domains, and a comprehensive process of identifying predominant frequencies was undertaken. Successively, the frequency spectrum obtained was compared against experimental measurements obtained using an accelerometer positioned at the inlet section of the compressor. A concordance between CFD and experimental outcomes was observed within a specific region of the impeller characterized by pronounced flow instabilities.

Lastly, an examination of the flow field was undertaken, with particular attention to the impeller domain, in order to elucidate a plausible physical interpretation for the observed pressure non-uniformities within the compressor.

Sommario

Lo scopo del presente lavoro è quello di sviluppare una configurazione di Fluidodinamica Computazionale (CFD) per l'analisi delle fluttuazioni di pressione all'interno della voluta di un compressore centrifugo. La fase iniziale dell'analisi CFD ha coinvolto l'uso simultaneo di Ansys® CFX e TRACE, seguito dall'impiego esclusivo di CFX per i calcoli finali. Il compressore di riferimento utilizzato per questa indagine è il Demag® KG3.32, e tutte le valutazioni comparative sono state condotte basandosi su misurazioni acquisite nel laboratorio dell'Università di Duisburg-Essen.

Il modello numerico è stato sviluppato in tre fasi principali, partendo dalla geometria semplificata con solo la girante a passaggio singolo e concludendo con il dominio completo a 360°con la girante completa e la voluta.

Inizialmente, è stata eseguita una valutazione comparativa tra le caratteristiche di prestazione del modello CFD e i dati sperimentali. Le discrepanze osservate in questa comparazione sono state principalmente attribuite alle incertezze derivanti dalla rappresentazione geometrica del modello CFD.

Successivamente, è stata condotta una simulazione non-stazionaria su tutto il dominio al fine di rilevare le fluttuazioni di pressione che si verificano all'interno della voluta. Numerosi punti di monitoraggio sono stati posizionati strategicamente all'interno della voluta per analizzare la distribuzione della pressione. Successivamente, è stato effettuato un monitoraggio analogo all'interno della girante per esplorare le interazioni tra i due componenti. I segnali di pressione registrati sono stati sottoposti a un'analisi sia nel dominio del tempo che nel dominio delle frequenze, e si è proceduto a un processo completo di identificazione delle frequenze predominanti.

Successivamente, lo spettro di frequenze ottenuto è stato confrontato con le misurazioni sperimentali ottenute mediante un accelerometro posizionato nella sezione di ingresso del compressore. Si è osservata una concordanza tra i risultati CFD e sperimentali all'interno di una specifica regione della girante caratterizzata da pronunciate instabilità del flusso.

Infine, è stata condotta un'analisi del campo di flusso, con particolare attenzione al dominio della girante, al fine di fornire una plausibile interpretazione fisica delle non uniformità di pressione osservate all'interno del compressore.

Contents

List of Figures

List of Tables

1

Introduction

Centrifugal compressors play a vital role in a wide range of industries, including process engineering, oil and gas, refrigeration, compressed air networks, turbochargers, and aeration plants. They facilitate the continuous compression of gases to elevated pressures, making them fundamental machines for the functioning of these applications. Achieving high compressor efficiency is crucial for minimizing energy consumption and operational costs. However, the demand for optimal performance extends beyond peak efficiency, encompassing a broad operational range and favorable efficiency even under off-design conditions.

The proper functioning of these machines is essential to maintain productivity, minimize downtime, and prevent failures that could lead to significant financial losses or even compromise human safety.

Therefore, the continuous monitoring of turbomachine operations to detect potential failures, such as damaged bearings or misaligned inlet guide vanes, has gained prominence, since effective diagnostics aid operators in making informed decisions, potentially leading to maintenance interventions.

Failure detection in turbomachines, where they take place thermo-fluid dynamics and mechanical interactions, involves the deployment of sophisticated monitoring systems and diagnostic methodologies to properly identify anomalies, deviations, or deteriorations in machine performance by monitoring crucial parameters such as vibration levels, temperature differentials, pressure fluctuations, rotational speeds, and fluid flow patterns. In this way, the operators can gain real-time insights into the machine's health and operational condition.

This approach often involves the integration of various diagnostic methods, such as vibration analysis, thermal imaging, and computational fluid dynamics (CFD) simulations.

A current research project explores the feasibility of identifying various failures using non-intrusive measurement devices, where a one-stage radial compressor is operated to identify the influence of different parameters on the measurement

signal.
An in-depth investigation of flow dynamics holds the promise of deciphering distinctive measurement signals corresponding to various flow phenomena. For instance, the occurrence of vortex shedding might manifest as a measurement signal at the frequency of vortex shedding.

This thesis is dedicated to a comprehensive exploration of the influence of diverse parameters on the pressure distribution within the volute casing. The primary research approach involves employing Computational Fluid Dynamics (CFD), where two different solvers, such as TRACE and Ansys® CFX, were contemporarily used for this purpose. The initial phase involves comparing the computed performance map (relating pressure ratio and efficiency to volume flow rate) with experimental measurements. Subsequently, the CFD model will be extended to a full-annulus 360°representation, incorporating the volute, where unsteady and time-resolved flow computations will then be executed. Analysis of the volute's pressure distribution across both time and frequency domains will enable comparison with laboratory measurements, thereby contributing to a deeper understanding of volute behavior and its implications.
Moreover, additional monitoring points were implemented in the impeller domain in order to evaluate the pressure fluctuations and other possible frequency peaks. Then an investigation regarding the flow structure in the impeller was done in order to evaluate the interaction with the downstream components. Furthermore, the results of the flow behavior in the impeller were compared with the literature to find the flow structure's similarities and attribute a plausible physical explanation.

2

Centrifugal compressor and volute

2.1 Centrifugal compressor theory

A centrifugal compressor, also known as a radial compressor, is a type of dynamic compressor used to compress gases. It operates by transferring energy from a rotating impeller to the gas, increasing its kinetic energy and subsequently its pressure.

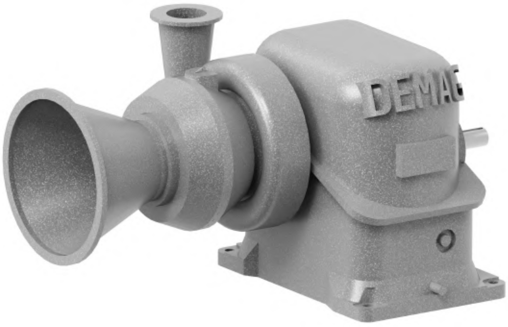

Figure 2.1: Rendering model of the Demag® KG3.32 centrifugal compressor.

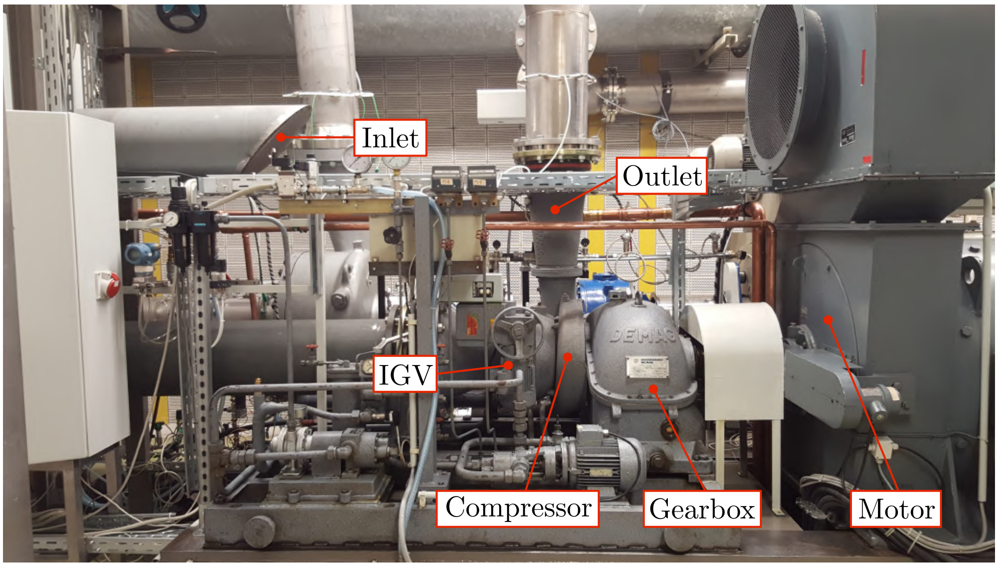

Figure 2.2: Physical model of the Demag® KG3.32 centrifugal compressor.

The centrifugal compressor typically consists of four major components:

- **Inlet**: The inlet is where the gas enters the compressor. It is designed to ensure a smooth and uniform flow of gas into the impeller. Inlet components may include flow straighteners or inlet guide vanes (IGV) to pre-swirl the flow properly into the impeller.
- **Impeller**: The impeller is a rotating wheel with curved blades or vanes attached to it. As the impeller spins at high speeds, it imparts kinetic energy to the gas, causing it to accelerate and move radially outward. This increase in kinetic energy results in an increase in the gas's velocity and pressure. The impeller exit flow velocity can reach transonic speeds.
  The type of impeller is determined by the exit blade angle.
- **Diffuser**: After leaving the impeller, the high-velocity gas enters the diffuser section. The diffuser is a stationary component with a gradually expanding passage. It converts the high-velocity gas into high-pressure gas by reducing its velocity and increasing its pressure. The diffuser slows down the gas and converts its kinetic energy into pressure energy. Diffusers can be vaneless or vaned depending on the case of application.
- **Volute**: The volute is the last component of the centrifugal compressor. It is a curved casing that collects the high-pressure gas from the diffuser and gradually expands the flow area. The volute helps to maintain a constant pressure while directing the gas towards the outlet of the compressor. The volute can take many different geometric shapes.

These four components work together to efficiently compress the gas and deliver it at the desired pressure and flow rate. Centrifugal compressors are known for their ability to achieve high pressure ratios, making them suitable for various applications in industries such as process, oil and gas, power generation, and transportation.

There are different types of blades in the impeller wheel with different advantages and usages. The impeller studied in this thesis consists of 15 inclined blades without any splitter blades. The configuration of inclined blades without splitters is commonly used in centrifugal compressors for specific design considerations. Regarding the operating range of centrifugal compressors, they are indeed limited by the surge and choke lines.

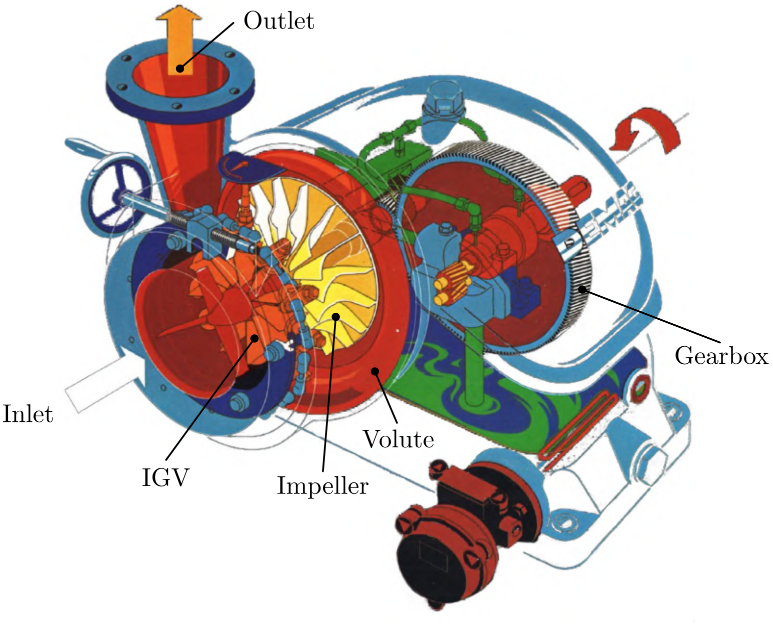

Figure 2.3: Main components of the Demag® KG3.32 centrifugal compressor in isometric view.

A compressor stage, which normally consists of a rotor and a stator, may be seen from the perspective of thermodynamics as an open system with mass and energy transfer occurring across system boundaries. The energy conversion that takes place during a compression process involves the transfer of mechanical energy from the rotor into the internal energy of the fluid. Even if the control system is not adiabatic, heat transfer across system boundaries is still included in the energy transfer. The working fluid continually entering and exiting the system is what defines mass transfer.

The 1^{st} Law of Thermodynamics may be used to describe the thermal process, especially for a steady-state compressor stage with a constant mass flow rate:

$$P + \dot{Q} = \dot{m}\left[h_2 - h_1 + \frac{1}{2}(c_2^2 - c_1^2) + g(z_2 - z_1)\right] \tag{2.1}$$

It shows that the quantity of energy changes between the system's intake and outlet, which are made up of static enthalpy, kinetic energy, and potential energy, is equal to the total of the work carried out by the rotor and the heat transfer across the boundaries. The majority of gaseous fluids have a low density, which makes the potential energy change minimal. The heat transmission coefficient Q is also 0 for an adiabatic system. The particular work of the rotor may be determined using the following two suppositions:

$$W = \frac{P}{\dot{m}} = h_2 - h_1 + \frac{1}{2}\left(c_2^2 - c_1^2\right) = h_{t2} - h_{t1} = \Delta h_t \tag{2.2}$$

Then, the ideal sum of moments caused by the fluid acting on a compressor's rotor blade is represented as follows:

$$M = \dot{m}\left(c_{u2} \cdot r_2 - c_{u1} \cdot r_1\right) \tag{2.3}$$

The specific work, often known as the Euler's turbomachinery equation W, may be determined as follows, assuming that the leakage caused by cavities and disk friction between the rotor and the shaft are negligible:

$$W = \Delta h_t = c_{u2} \cdot u_2 - c_{u1} \cdot u_1 \tag{2.4}$$

Knowing that:

$$c_{u2} \cdot u_2 = \frac{1}{2}(u_2^2 + c_2^2 - w_2^2) \qquad \text{and} \qquad c_{u1} \cdot u_1 = \frac{1}{2}(u_1^2 + c_1^2 - w_1^2) \tag{2.5}$$

Equation 2.4 can be transformed into:

$$\Delta h_t = \frac{u_2^2 - u_1^2}{2} + \frac{c_2^2 - c_1^2}{2} - \frac{w_2^2 - w_1^2}{2} \tag{2.6}$$

Where, $h_t = h + \frac{c^2}{2}$, and then:

$$h_1 + \frac{1}{2}w_1^2 - \frac{1}{2}u_1^2 = h_2 + \frac{1}{2}w_2^2 - \frac{1}{2}u_2^2 \tag{2.7}$$

The the physical propriety of *rotalphy* is defined as:

$$h_{rot} = h + \frac{1}{2}w^2 - \frac{1}{2}u^2 \quad \longrightarrow \quad h_{rot,1} = h_{rot,2} \tag{2.8}$$

It shows that under all simplifications mentioned above, the rothalpy remains constant throughout the rotor.

The static-to-static pressure ratio (Π_{ss}) and isentropic efficiency (η_{is}) are two dimensionless quantities used to characterize the idealized process of a compressor without heat exchange to the surroundings [1].

These quantities are defined as follows:

$$\Pi_{ss} = \frac{p_{s,out}}{p_{s,in}} \qquad \text{and} \qquad \eta_{is} = \frac{\Pi_{ss}^{\frac{(k-1)}{k}} - 1}{\frac{T_{s,out}}{T_{s,in}} - 1} \tag{2.9}$$

where p_s is the static pressure and T_s the static temperature at the compressor inlet and outlet, respectively.

Furthermore, the total proprieties are defined as:

$$p_{tot} = p\left(1 + \frac{k-1}{2} \cdot Ma^2\right)^{\frac{k}{k-1}} \quad \text{and} \quad T_{tot} = T\left(1 + \frac{k-1}{2} \cdot Ma^2\right) \tag{2.10}$$

with the isentropic exponent k and the Mach number Ma defined as the ratio of flow velocity u to local speed of sound c:

$$Ma = \frac{|u|}{c} \tag{2.11}$$

The overall isentropic efficiency is useful as a measure of the overall performance of a turbocompressor for the purpose of determining power. However, it is not always a true indication of efficiency regarding internal losses.
Since isentropic work (Fig.2.4) is proportional to temperature rise ($W_{ad} = c_p\Delta T$), the distance from point 1 to point 2_{ad} is proportional to the adiabatic work required to compress the gas from p_1 to p_2. The actual work, however, is proportional to the vertical distance from point 1 to point 2.

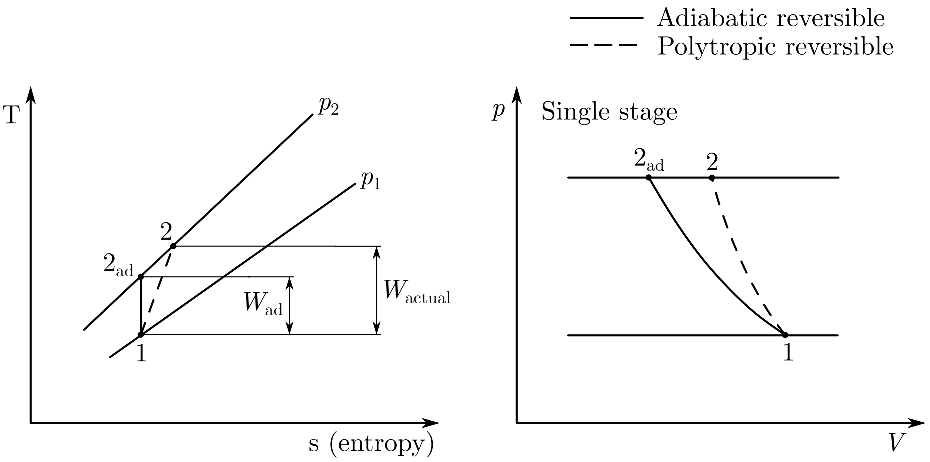

Figure 2.4: Isentropic versus polytropic process comparison [2].

This polytropic equation represents the true aerodynamic efficiency of a compressor for the compression of an ideal gas:

$$\eta_p = \frac{(\frac{k-1}{k})\ln(\Pi_{ss})}{\ln(\frac{T_{s,in}}{T_{s,out}})} \tag{2.12}$$

There are, however, limitations to this equation also, because real gases do not always have a constant k value. Therefore, the value of k for some gases at discharge conditions can vary significantly from the k value at suction conditions. The enthalpy (or Mollier) equation (Eq. 2.13) is the most accurate means of calculating the aerodynamic efficiency for any condition as it does not depend on the k value being a constant. In some cases, it is the only equation that can provide accurate results.

$$\eta_p = \frac{\text{Head}}{\text{Work input}} = \frac{H_p}{h_2 - h_1} \tag{2.13}$$

The compressor performance depends on the inlet conditions, and then the volumetric flow rate ($\dot{V}$) is a parameter used to compare compressor performance under different inlet conditions. It takes into account the ambient conditions and allows for a meaningful comparison of measurement data and numerical results. The formulation for the volumetric flow rate is as follows:

$$\dot{V} = \frac{\dot{m}}{\rho(p_{ref}, T_{ref})} \cdot 3600 \quad [\mathrm{m}^3/\mathrm{h}] \tag{2.14}$$

based on the inlet reference conditions:

$$p_{ref} = 103560 \text{ Pa} \qquad \text{and} \qquad T_{ref} = 297.533 \text{ K} \tag{2.15}$$

Subsequently, the work coefficient is defined as the fraction between total enthalpy change and u_2^2,

$$\tau = \frac{\Delta h_t}{u_2^2} = \frac{c_p(T_{t,out} - T_{t,in})}{u_2^2} \tag{2.16}$$

while the head coefficient is defined as the product between the polytropic efficiency and the work coefficient. The head coefficient is specifically applied for process compressors to evaluate its compression capability and energy consumption in combination.

$$h = \tau \cdot \eta_p \tag{2.17}$$

Afterwards the diffusion quality is typically measured using the following variables:

- Loss coefficient: the ratio of the dynamic pressure component at the intake to the overall pressure loss during diffusion.

$$K_p = \frac{p_{tot,in} - p_{tot,out}}{p_{tot,in} - p_{in}} \tag{2.18}$$

- Recovery factor: the ratio of the dynamic pressure portion at the intake to the static pressure rise brought about by diffusion.

$$C_p = \frac{p_{out} - p_{in}}{p_{tot,in} - p_{in}} \tag{2.19}$$

2.1.1 Choke condition

Choke, also known as stonewall, is a phenomenon where a significant increase in flow capacity leads to a substantial decrease in pressure. It represents the upper limit of the compressor's operating range, beyond which it cannot handle additional flow without a significant decrease in pressure ratio. This occurrence arises when the Mach number approaches to 1.

Operating a centrifugal compressor at excessively high flow rates can severely impact its performance and potentially cause damage. The stonewall effect in the centrifugal compressor stage with a vaneless diffuser is regulated by the impeller's inlet vector geometry.

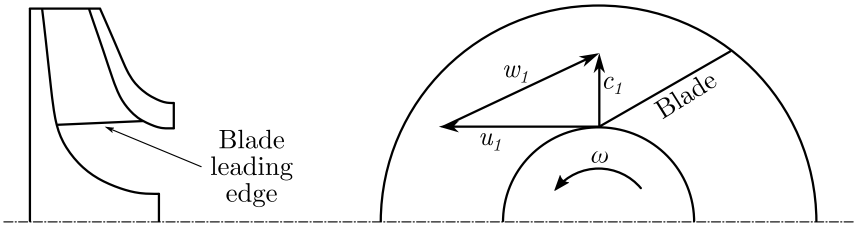

Figure 2.5: Velocity vectors in the impeller inlet

To draw an analogy using an aircraft's airfoil, surge and choke represent the points at which the airfoil stalls under very high positive flow incidence (i.e., high angles of attack) and very high negative flow incidence. In a compressor, choke is associated with a flow regime characterized by extremely high flows. Consequently, the flow channels between blade rows may encounter blockage effects caused by factors such as sonic flow shocks, wake areas, strong secondary flows, or simply inefficient utilization of the through-flow area. In practice, it is common to observe a combination of these factors contributing to choke conditions.

In figure 2.5, the u_1 represents the tangential velocity at the leading edge of the blade, while c_1 represents the absolute velocity of the fluid at the inlet. After making a 90° turn, the air now moves radially (in the absence of pre-whirl inlet guide vanes), hence referred to as a radial inlet.

Through vector analysis, w_1, which denotes the gas velocity relative to the blade, is depicted in magnitude and direction as shown. At the design flow rate, w_1 aligns with the blade angles.

However, as the flow exceeds the design point, c_1 increases, consequently elevating w_1. This leads to w_1 impinging on the blade at a negative angle, known as a negative angle of attack. The presence of high negative angles of attack exacerbates the stonewall phenomenon due to boundary-layer separation and a reduction in effective blade area. This reduction, combined with the already high w_1, causes the gas to reach Mach $= 1$ and triggers a corresponding shock wave, as illustrated in Figure 2.6

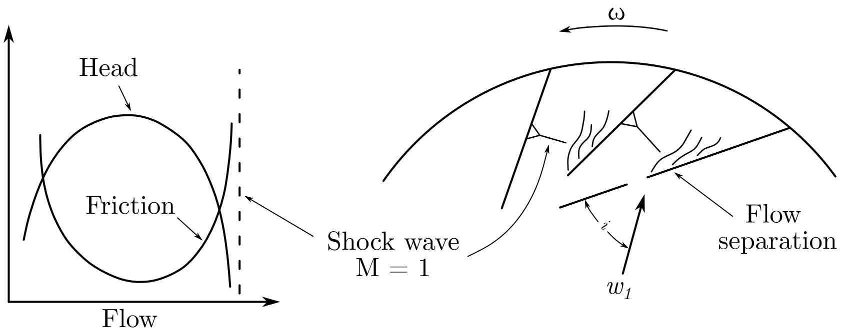

Figure 2.6: Stonewall effect with shock wave propagation [2].

2.1.2 Stall and Surge condition

Rotating stall

The two issues that influence centrifugal compressor performance the most are stall and surge. Stall can have a variety of effects and can range in severity from a slight loss of power to a total loss of compression with flow reversal (deep surge) towards the compressor's intake. The performance can be drastically reduced by surge, and the engine parts may also sustain permanent damage.

When the separation point of the flow on the top surface reaches the leading edge of a wing profile, a stall happens. Once stall conditions have been overcome, the flow around the plane generates less lift, which results in more aerodynamic drag. The major cause of stall is an unfavorable pressure gradient and the flow detached when the positive pressure gradient becomes too great to be overcome. Generally, a point is reached at which the pressure rise is a maximum and a further reduction in mass flow leads to an abrupt and definite change in the flow pattern. Beyond this point, the compressor enters into either stall or surge.
At very low mass flows, the amount of fluid flowing over the impeller is insufficient for the machine to operate properly because the flow is not evenly distributed

across the compressor's circular section, meaning some vanes receive more fluid than others.

There are two distinct categories of revolving stalls that may be described:

- **Progressive stall**: Performance (namely the pressure ratio) is only slightly reduced, but the device's noise and vibration levels rise. In this instance, a number of tiny stall cells that span a portion of the impeller annulus can be seen

- **Abrupt stall**: Performance and pressure ratio drastically decrease, accompanied by noise and vibrations. A distinct stall cell that extends from the hub to the shroud is what gives the impeller flow field its distinctive appearance.

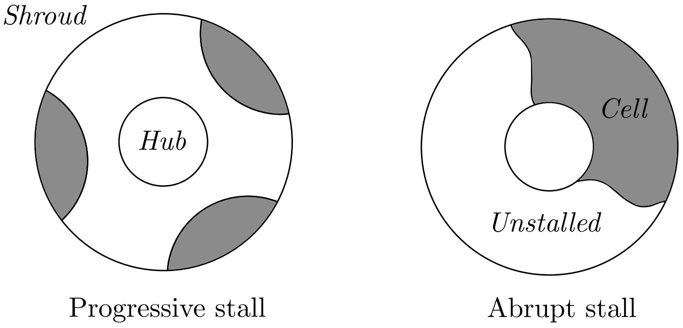

Figure 2.7: Different types of rotating stall [3]

The mass flow and compressor design have been shown to be the most crucial variables in determining which of the two forms of spinning stall would occur. Although the total time-averaged mass flow is maintained in both scenarios, the stopped cells rotate in the opposite direction from the impeller at a slower rate (20-40% for a sudden stall, 50% for a gradual stall). Only one blade is first impacted by the stall (Fig. 2.7), and flow divides across its suction surface. In the sense of rotation of the impeller, the obstruction brought on by the split flow causes an increase in incidence on the following blade and a reduction on the previous one.

Surge

Surge flow is characterized by the maximum head value. Below the surge point, a decrease in flow results in a decline in head (refer to Figure 2.8).
During surge, flow reversal transpires, causing nearly all compressor components to undergo reverse bending. The surge forces become more damaging as the pressure or energy level increases. Surge is often defined as the beginning of time-dependent mass flow changes at a predetermined frequency. Pulsating pressure and vibration in the system are also present along with these fluctuations in mass flow. Since the flow pattern within the compressor continually shifts from being stalled to unstalled due to the process' unsteadiness, it is not possible to distinguish separation cells as in the case of rotating stall.

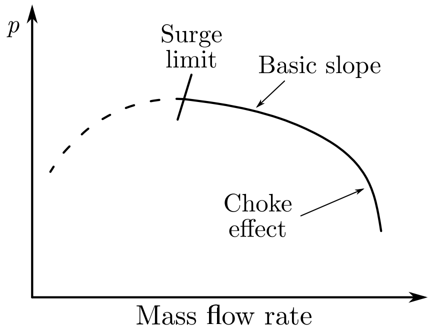

Figure 2.8: Traditional shape of a performance curve of a single stage radial compressor [2]

When flow is reduced while maintaining a constant speed, the magnitude of w_1 diminishes proportionally, leading to a decrease in the flow angle (see Figures 2.18). Additionally, the incidence angle increases (Figure 2.9).

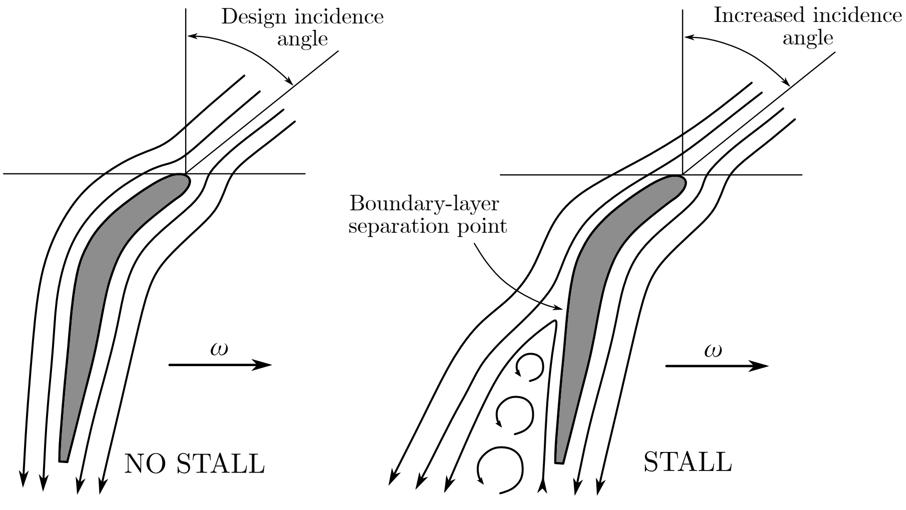

Figure 2.9: Mechanism of stall propagation within the stall cells.

The losses incurred during low flow conditions (see Figure 2.9) are partly attributed to a lower incidence angle i which can result in flow separation at the low-pressure side of the blade's leading edge. This flow separation often commences at one or more blades and progressively shifts around the impeller blades. This occurs at relatively low speeds, just before reaching full surge. At higher speeds, the compressor typically transitions directly from stable operation to flow separation on all blades, accompanied by complete reverse flow.

There are two distinct forms of surge that may be distinguished based on the intensity of the oscillations:

- **Mild surge**: pressure and mass ow fluctuate at a frequency that is consistent with the system's inherent frequency. On the compressor map, the operating point of the compressor does not fluctuate much, but for a fixed wheel speed, it tends to circle about the point closest to the surge line. Due to the relatively modest amount of oscillation, mild surge is typically tolerable. Deep surge often begins in tiny turbochargers first, followed by mild surge.
- **Deep surge**: oscillations have lower frequencies than the system's inherent frequency. However, the variations in mass flow and pressure are so great that the compressor becomes unstable. The flow is reversed and re-emerges out of the intake when the volume of fluid entering the compressor is insufficient to overcome the high pressure region downstream of the impeller during a portion of the surge cycle. Both the compressor blades and the parts upstream of the turbocharger unit may suffer severe damage as a result of this.

To operate a centrifugal compressor efficiently, it is important to maintain operation within the range between the surge and choke lines. This range is known as the stable operating range or the surge margin. Operating too close to surge or approaching choke conditions can lead to performance degradation, instability, and potential damage to the compressor. Therefore, proper control and monitoring systems are employed to ensure safe and efficient operation within the specified operating range of the compressor.

2.2 Volute principle

The vaneless diffuser and the volute have to be properly designed in order to collect the flow, reduce flow speed and convert the kinetic energy into potential energy/static pressure.

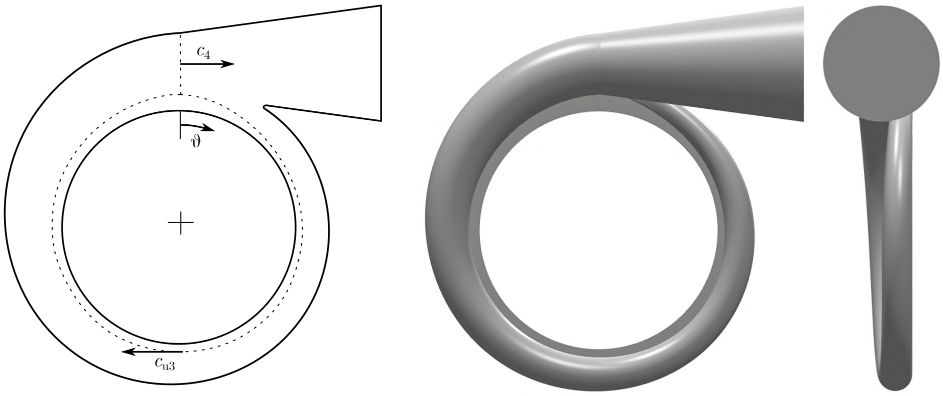

Figure 2.10: Left: a schematic view of the volute: right; 3D views of the fluid-swept surfaces of a volute.

It's important to note that the volute itself does not actively contribute to the energy transfer process onto the fluid. Instead, its design aims to minimize losses and facilitate smooth flow distribution.
Ideally, there should be a uniform static pressure distribution at the diffuser exit close to the nominal point and no strong once-per-revolution disturbance from any circumferential pressure gradients or from the tongue. By carefully designing the volute, the efficiency of the entire compressor system can be improved.
While the impeller plays a crucial role in imparting energy to the fluid, an optimal volute design can lead to improved efficiency, reduced losses, and better matching of the compressor characteristics to the system requirements.

The shaded area depicted in figure 2.11 comprises two distinct sections. The volute occupies the space between states 3 and 4, where it collects the flow surrounding the diffuser. The exit-cone, located between states 4 and 5, further decelerates the flow prior to its entry into the pipe system. The initial part of the exit-cone, situated between states 4 and 4', is partially connected to both the diffuser and the small volute channel through the tongue gap.
In literature, the term "volute" can refer to either the portion between states 3 and 4 or the entire shaded region encompassing states 3 to 5. However, in this study, volute specifically denotes the section between states 3 and 5. It is crucial to closely examine the volute and the exit cone together since the performance of

the exit cone heavily relies on the flow field generated by the volute, particularly the flow disturbances originating from the tongue area.

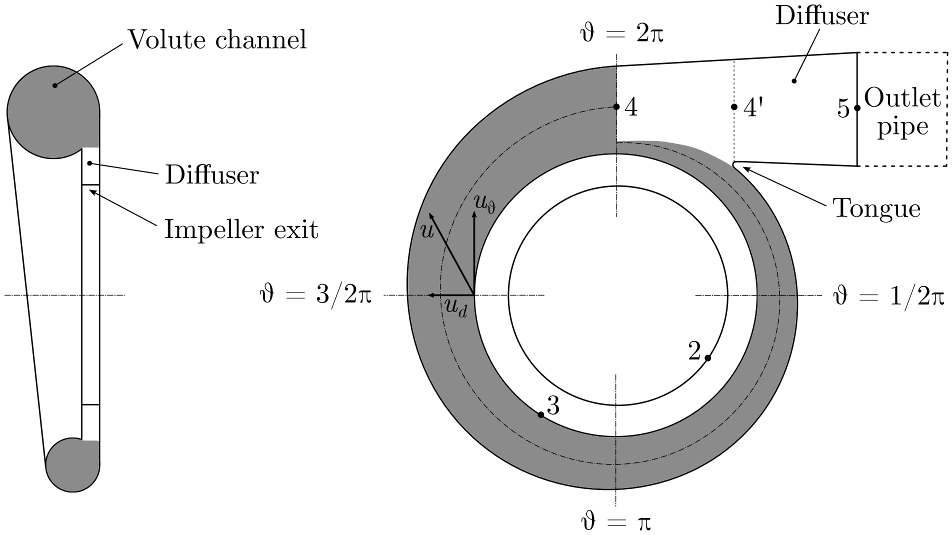

Figure 2.11: Schematic view of the sections in the volute domain.

The ratio of the cross-sectional area and radius (A/r) is often used to denote the size of a given volute. At the design point of the volute, A/r is defined by the diffuser outlet width and the flow angle at the diffuser outlet. With a vaneless diffuser (as in the tested compressor), the flow angle is larger and the volute has a higher inlet kinetic energy at inlet and is only matched to the exit flow angle of the vaneless diffuser at one operating condition. The difference in flow angle at diffuser exit between vaned and vaneless diffusers means the volutes are quite different in size for a given impeller.

In off-design conditions, the through-flow velocity in the volute can no longer remain constant. At lower mass flow rates, the volute receives less fluid compared to the design point, resulting in a reduction in through flow velocity and an increase in static pressure due to the faster expansion of the cross-sectional area than required. Conversely, at higher mass flow rates, the through-flow velocity accelerates, causing the static pressure to decline along the circumference. Even at the design flow, velocity and pressure non-uniformity may arise if the volute has been poorly designed. When utilizing a vaneless diffuser, the non-uniform pressure distribution affects both the diffuser and the impeller, becoming noticeable even at the leading edge of the impeller blades [4]. This phenomenon leads to oscillations in pressure, velocity, and flow angles within the diffuser and impeller blade passages, resulting in reduced efficiency and increased noise. The stable operating range of the compressor is also diminished [5]. The non-uniform pressure distribution exerts radial forces on the impeller and generates unsteady forces on the blades, potentially causing excessive loads on the bearings and blade vibrations.

The absolute size of the volute scroll, in terms of A/r value, can have an effect on the performance map of the compressor. The losses that occur in the volute depend on the kinetic energy at the outlet of the diffuser. This is higher with a vaneless diffuser than with a vaned diffuser.
Furthermore, if the volute is undersized, the performance curve is shifted towards lower flow rates. Sometimes this shift is made intentionally in order to fine-tune a machine to a desired flow range [6].

2.2.1 Flow inside a volute passage

The characteristics of the flow field in the passage depend on the vortex formation within the volute channel. According to Ayder et al. [5, 7] there are two distinct vortex patterns: forced vortex and free vortex flow.

In a forced vortex, the tangential velocity increases as the radius increases whereas the free vortex is defined by an inverse proportional tangential flow velocity with respect to the radius. The fluid near the tongue (at a small radius) starts swirling around the center of the volute cross-section. This results in large velocity gradients, shear stresses, and losses. The kinetic energy at the center of the volute is quickly dissipated until a forced vortex is fully developed. As a result, a drop in total pressure is observed in the center of the volute channel. The flow pattern downstream of this point depends on the operating conditions.

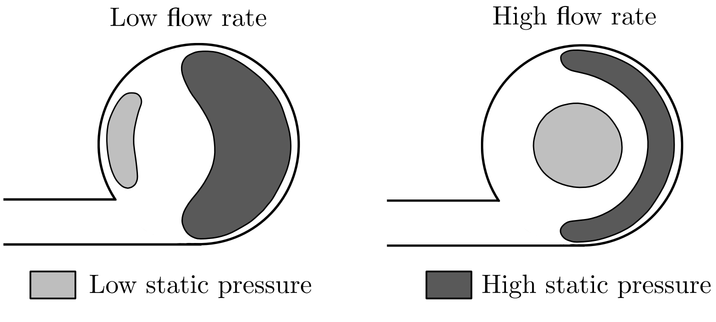

Figure 2.12: Characteristic static pressure distribution inside a volute channel for low and high flow rates.

At lower flow rates, there is reduced swirl in the volute channel due to small radial flow velocities at the volute inlet. In this case, a forced vortex is formed due to internal shear stresses in the center of the volute cross-section. The forced vortex gradually expands to cover the entire volute cross-section further downstream. This leads to a more uniform distribution of total pressure with a minimum in the center due to energy dissipation. Centrifugal forces are weak at low flow rates, resulting in decreased static pressure at the inner volute wall due to higher flow velocities resulting from the conservation of angular momentum in the volute cross-section (Fig.2.12-left).

At high flow rates, as the fluid moves downstream through the volute channel, it is wrapped around by fluid entering through the volute inlet, creating a forced vortex. In this case, the flow field and total pressure distribution are influenced by the volute inlet flow velocity distribution and the way the volute is filled, rather than energy dissipation in the center of the volute cross-section. Low-energy fluid accumulates in the center of the vortex, leading to a decrease in total pressure from the walls towards the center. The static pressure distribution is mainly affected by strong swirl velocities, resulting in low static pressure in the center of the volute cross-section (Fig.2.12-right). Internal shear stresses in a forced vortex are null. Therefore, a decrease in swirl within the volute can only be achieved through friction on the volute walls or an increase in radius at the exit diffuser.

2.2.2 Volute with vaneless diffuser

The matching of the volute to the impeller and diffuser it's very complicated because there is normally only one offtake and one tongue. Any non-uniformity generated by these is therefore going to contain a large harmonic at the fundamental, once per revolution, which will decay only slowly in the upstream direction. The disturbance from the tongue can be large right through the impeller and upstream of it as well, and therefore at some stalled operating conditions, we may have reverse flow forward out of the impeller at a fixed circumferential position related to the tongue. Furthermore, since the velocities are small, friction on the walls of the volute is not likely to generate much loss. Frictional losses will occur but, compared to the long narrow passages upstream in the compressor where the velocities are very much higher, this contribution from the volute is going to be small [8].

Once a volute geometry and size are chosen, the design condition of circumferentially uniform flow can only be achieved for one particular value of the ratio u_d/u_θ (Fig.2.11). This means that at a given rotational speed, there will be only one inlet volumetric flow rate which will give the uniformity designed for.

If the impeller rotational speed rises then the flow into the diffuser inclines more and more towards the tangential. The friction in the vaneless diffuser works so as to reduce the tangential momentum so that the mean tangential velocity decreases more rapidly than inversely proportional to the radius. The friction in the radial direction only drops the static pressure (and therefore also the density) so the mean radial velocity decreases slightly more slowly than inversely proportional to radius.

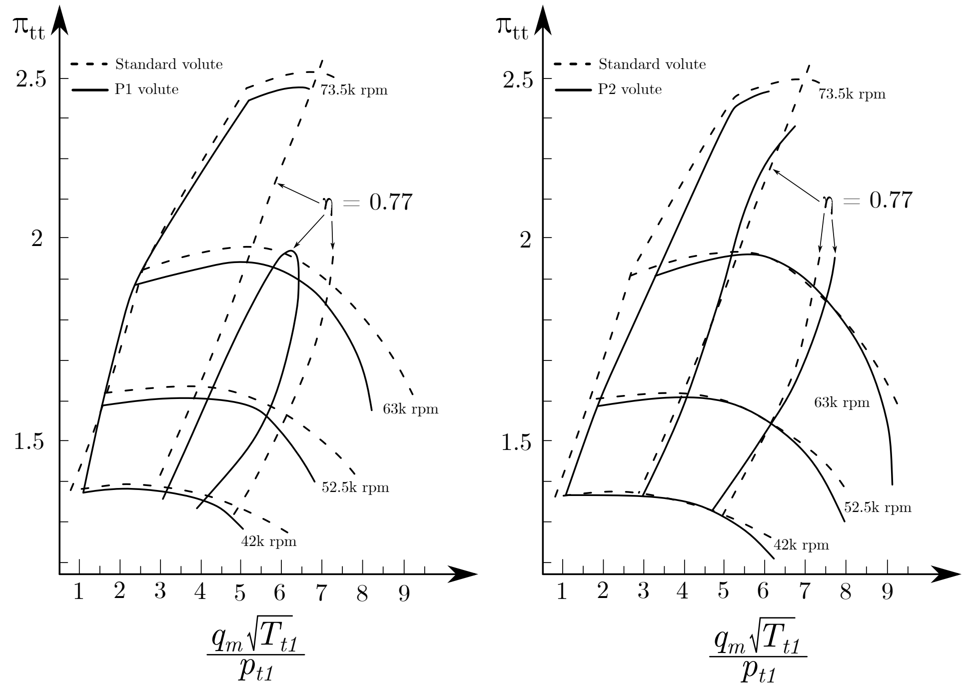

Figure 2.13: Performance maps of a radial compressor with two different volute sizes and comparison to the standard configuration [9].

In a research published by Whitfield and Roberts [9], two substitute volutes for a typical centrifugal compressor were produced and tested. The first volute P1, was created with no diffusion allowed inside the volute and thus the diffusion occurred in the exit cone. This was made possible by the cross-sectional area of the volute P1 being less than that of the conventional volute. Suddenly in order to facilitate diffusion inside the volute, the second volute P2, had a greater cross-sectional area than the conventional volute.

The performance maps of the compressor with the redesigned volutes are shown in Figure 2.13, along with a comparison to the standard setup. Both of the new configurations are observed to have a detrimental impact on performance. According to reports, the compressor with volute P1 produces a lower pressure ratio mostly as a result of greater volute losses brought on by the need to collect the fast-moving flow around the diffuser. The compressor with volute P2 produces a pressure ratio that is almost equal, but the stall limit is moved toward greater flow. This is mostly caused by the significantly higher pressure distribution non-uniformity during off-design circumstances.

The increasing pressure non-uniformity is what causes the performance of both new volutes to noticeably decline at high flow. Furthermore, the variation in tongue shape is another explanation for the subpar performance of the new volutes [9].

2.3 Geometry characteristics

Due to the existence of both fixed and rotating components, the flow in the compressor is highly unstable, which makes it challenging to analyze. A workaround for this issue is to describe the velocity triangles of the flow around the impeller by using a reference system for the rotating component. As a result, a reference stationary frame whose z-axis matches the rotational axis of the compressor wheel is used. The same axis is also used for a rotating reference frame, which will rotate around the z-axis at the same speed as the impeller. Figure 2.14 depicts the typical flow velocity triangles near the blade tip at the inducer and exducer portions. Three distinct velocity vectors in particular could be found:

- Absolute velocity $\vec{c}$: determines the flow velocity in relation to the stationary frame;
- Relative velocity $\vec{w}$: identifies the velocity vector on the impeller's relative coordinate system;
- Tangential velocity $\vec{u}$: identifies the local velocity of the wheel at a given location. Given the impeller speed ($\vec{w}$) the tangential blade velocity at location ($\vec{R}$) can be written as $\vec{u} = \vec{w} \wedge \vec{R}$.

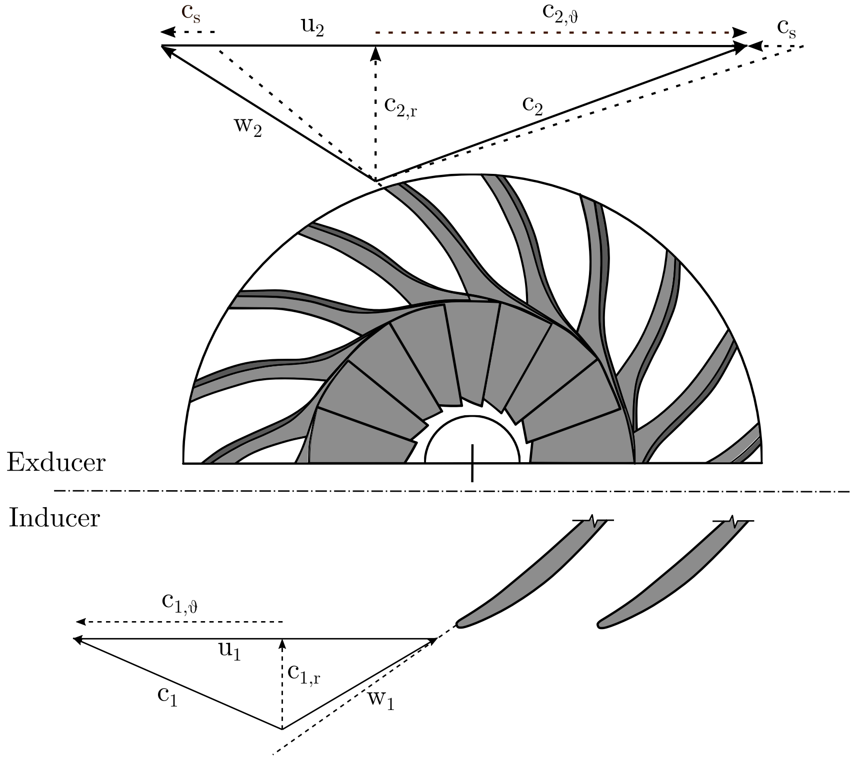

Figure 2.14: Velocity triangles on compressor's impeller [10].

The components along the axial (subscript z), radial (subscript r), and tangential (subscript ϑ) directions are used to determine each of these velocities. The Euler's turbomachinery equation for adiabatic and steady-state flows determines the work input in the compressor:

$$W_{1,2} = u_2 c_{\vartheta,2} - u_1 c_{\vartheta,1} \tag{2.20}$$

The compressor's purpose is to raise static pressure, which also raises static enthalpy. Equation 2.20 can be rewritten differently with reference to the rotating frame:

$$h_2 - h_1 = \int_{p_1}^{p_2} \frac{dp}{\rho} + \int_{T_1}^{T_2} T ds = \frac{1}{2}(u_2^2 - u_1^2) - \frac{1}{2}(w_2^2 - w_1^2) \tag{2.21}$$

where h and p stand for static enthalpy and pressure, respectively. In addition, heat transfer to and from the flow is disregarded, and no work needs to be done on the fluid. This equation, also known as the conservation of rotalphy, is only true for stable flows in the impeller rotating frame. The entropy-based integral cancels out when the assumption of isentropic flow is made, which means that losses primarily attributable to shear work and flow mixing are ignored.
Equation 2.21 then serves as a useful tool for assessing each factor that contributes to the pressure rise across the impeller.

It must be stressed that this contribution solely depends on the impeller design and does not cause any loss or irreversibility in the flow. In addition to the flow deceleration from w_1 to w_2, the compression process is also driven by an increase in tangential velocity at the blade tip from u_1 to u_2. Centrifugal compressors are distinguished from axial ones by this feature; in the latter, the variation in magnitude of the peripheral velocity u is small, and compression is mostly achieved through flow deceleration.

Furthermore, centrifugal machines have a larger operating range and higher efficiency than axial ones since the term $\frac{1}{2}(u_2^2 - u_1^2)$ is independent of flow separation and only depends on wheel speed. In other words, the flow will be less susceptible to boundary layer separation and flow reversal if the majority of the static enthalpy rise is attributable to the change in blade speed between the inlet and outlet; the main constraint on pressure rise then becomes the structural robustness of the wheel components. The ratio $R_2 = R_1$ between the blade radius at each of the inducer and exducer is one quick solution that manufacturers are using to reduce the disparity in tangential blade velocities at the inducer and exducer.

2.3.1 Impeller flow

The flow typically undergoes a velocity acceleration and a static pressure drop as it passes through the stage inlet components before it reaches the impeller. The flow must follow the radially outwards direction through the blade passage while being severely rotated in the circumferential direction at the impeller input section by the blade forces. The impeller's flow path is described as having a "pseudo-helical" pattern by Japikse [11].

Figure 2.2 shows the primary flow with simple untwisted blades in addition to the variations in the velocity triangles at the impeller leading edge due to various locations at the near-hub, midspan, and near-shroud. At meridional portions, the true flow is condensed into a two-dimensional flow.

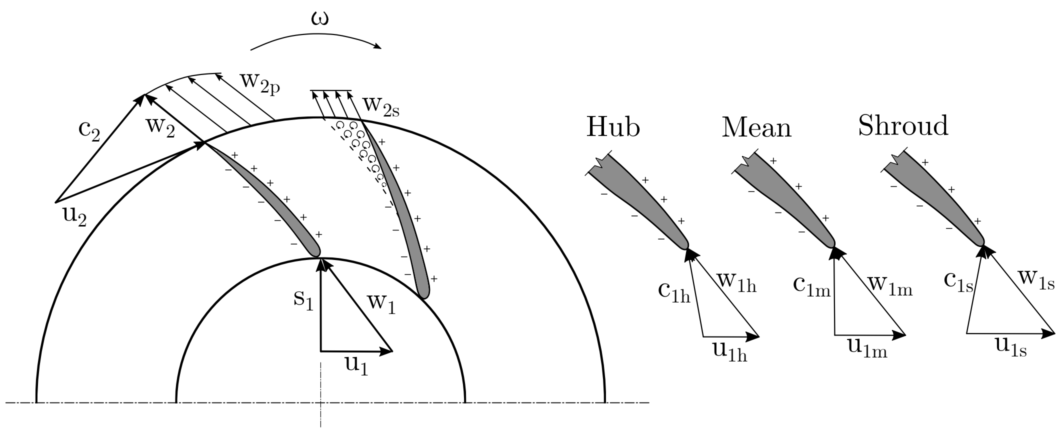

Figure 2.15: Impeller 2D primary flow with inlet and outlet velocities and jet-wake flow [11] and the velocity triangles under ideal operation at three spanwise sections [12].

The traditional two-zone model is shown between the entrance and exit by w_{2p} and w_{2s} using various vectors. They are a result of the secondary, non-isentropic flow that causes the suction-side flow to often diverge from the blade surfaces. The term "jet-wake" flow refers to this secondary flow pattern, which Dean [13] and Benvenuti [14] initially explored and Eckardt [15] extensively quantified. These studies identified the jet-wake flow as both a flow energization at the impeller hub on the pressure side and a flow momentum deficit near the impeller shroud on the suction side.

The three ideal velocity triangles in Figure 2.15 show that, under ideal operating conditions, the relative velocity w should follow the path dictated by the blade camber line direction at the leading edge. The optimal absolute inflow velocity c_1 must be adjusted as necessary since the circumferential velocity u grows continually from hub to shroud along with the expanding blade radius [12].

By placing an extra blade cascade in front of the impeller, such as an IGV stage as was mentioned in this paper, the direction of inlet velocity c can be changed in practical applications. The input velocity triangle must turn from its initial course for a true compressor stage with variable mass flow rates.

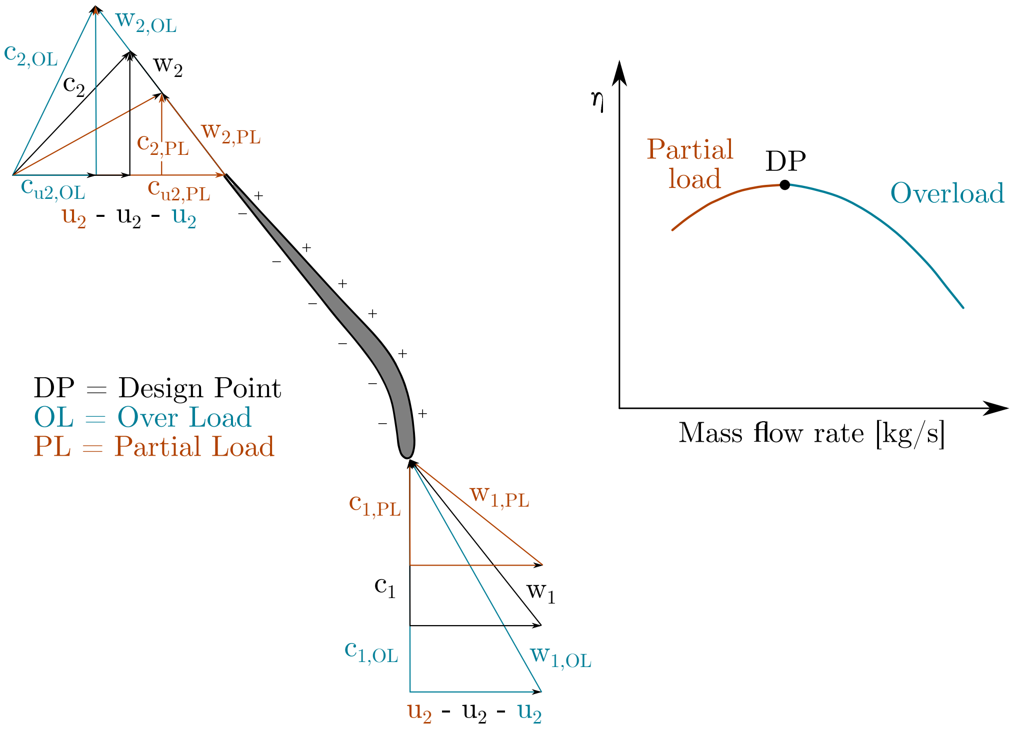

Figure 2.16: Impeller flow with velocity components at inlet and outlet for working at design point (DP), partial load (PL) and overload (OL) [12].

Figure 2.16 shows a schematic of the velocity triangles for the compressor flow at the impeller leading edge and trailing edge showing the changes in the mass flow at its partial load and overload to demonstrate the impacts of mass flow variations in the impeller flow directions. The impeller leading edge is depicted in the simplified schematic as having an axial inlet flow (also known as free-of-swirl) at its design position. In order for the impeller inducer to function optimally without incidence losses, the relative velocity $w_{1,DP}$ that approaches the blade leading edge should be perfectly aligned to the impeller camber line at the leading edge. An ideal situation would be for the impeller flow to completely match the impeller blade profile, producing a relative velocity at the trailing edge w_2 that is also aligned with the blade direction. In case of a partial load, the absolute inflow velocity c_1 must drop to a lower value, $c_{1,PL}$. A positive incidence increase $(+\Delta i)$ results from the relative intake velocity $(w_{1,PL})$ deviating from its initial alignment with the blade camber line while spinning at the same speed (u_1).

This incidence angle may result in a suction-side flow separation because it tends to push the flow away from the blade suction-side surface. Assuming that the impeller flow ultimately remains follows the blade profile despite the incidence deviation at the leading edge, the relative outlet velocity $w_{1,PL}$ therefore merely decreases in magnitude without altering its direction. The absolute outlet velocity $c_{2,PL}$ will be oriented towards the tangential direction as a result of this change in the $w_{2,PL}$ and the constant u_2, leading to a higher magnitude of $c_{2,PL}$ at the impeller trailing edge, as shown in Figure 2.16.

The greater $c_{1,OL}$ causes a negative incidence deviation $-\Delta i$, which provides the impeller flow a tendency for a pressure side flow separation if the impeller operates at overload with an excessive mass flow rate. Due to the absolute velocity $c_{2,OL}$ being directed towards the radial direction, the velocity triangle at the impeller trailing edge will change into a bigger and steeper shape. It is important to note that the impeller flow in Figure 2.16 is only studied in light of the main flow pattern.

Other potential secondary flow effects, such as the jet-wake flow discussed in the previous session, the potential for flow separation in the blade passages, the potential for leakage flow caused by tip clearance, and boundary layer flow causing slips at the impeller trailing edge, may still be present in the actual flow at the impeller trailing edge [3]. The true impeller flow is affected by these secondary flow parameters as well, making it more complex than what is depicted in Figure 2.16.

According to Japikse [11], the impeller work coefficient τ is directly associated with the c_{u2} and c_{u1} (Eq.2.16), with the latter being further directly impacted by a pre or counter swirl produced by IGVs. As a result, an existing IGV stage has a significant influence on the compression's overall pressure ratio.
As mentioned before, the reference compressor of this thesis is the Demag® KG3.32, which is equipped with Inlet Guide Vanes. However, for the purposes of this research, the IGV will not be taken into account in the simulation and analysis.

2.3.2 Diffuser flow

It is common for the flow to reach a high velocity level as it approaches the diffuser, which is made possible by the impeller's strong trailing edge rotation and the flow acceleration that occurs along the blade passages. This fraction of kinetic energy is then converted into further pressure increase by the application of a diffuser. Vaneless and vaned diffusers are two of the diffuser's common types. Since it lacks a throat that may choke early during an overload operation, a vaneless diffuser offers a broader operating range than a vaned diffuser of comparable size. Therefore, a vaneless diffuser is mostly used in process compressors and turbochargers where the mass flow rates significantly fluctuate due to wide fluctuations in operation modes.

The geometry of a vaneless diffuser is shown in Figure 2.17, that it consists of a straightforward annular tube that radiates outward from the impeller output but without vanes. The channel typically has the same width as the impeller, but as the radius grows, it may become narrower. A parallel walled channel is employed after a pinched diffuser in some applications because it narrows towards the impeller exit. The purpose of the pinch is to raise the meridional velocity, and as the casing side has the lowest meridional velocity. In the presented case, the studied diffuser is a parallel type vaneless diffuser. Two processes work together to reduce velocity in the vaneless diffuser. First, the meridional channel area increases with radius and reduces the meridional velocity component of the fluid velocity. Second, in the absence of blade forces and also neglecting frictional forces, the angular momentum of the fluid remains constant and so the circumferential velocity component also decreases with radius. The radial extent of the vaneless diffuser then fixes the ideal pressure recovery that can be achieved.

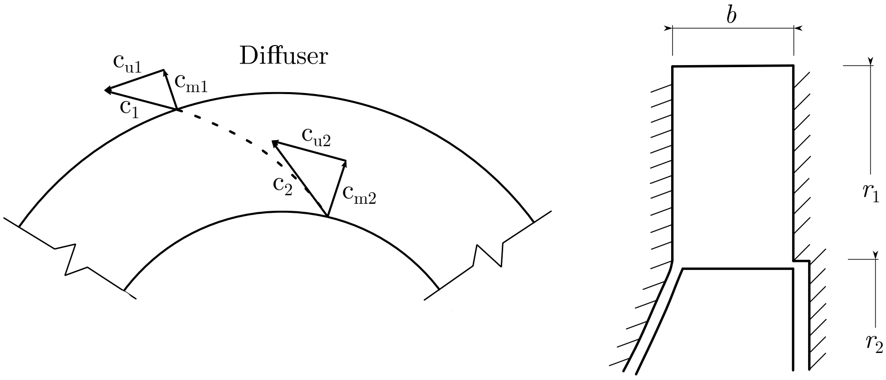

Figure 2.17: Flow in the vaneless diffuser with velocity components at the diffuser inlet and outlet.

For incompressible flow in an ideal diffuser with no losses and with constant width, the flow trajectory should follow a logarithmic spiral [11] and it is shown in Figure 2.18.

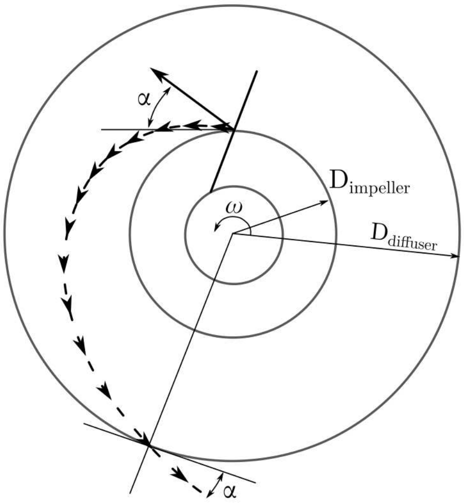

Figure 2.18: Flow through a radial diffuser [2]

This is due to the diffuser flow being restricted by angular momentum conservation ($r \cdot c_u = constant$). Thus, the circumferential velocity c_u should decrease in direct proportion to the increase in diffuser radius r from the intake to the exit. According to the principle of mass conservation, the meridional velocity c_m should decrease as a result of the expanding cross-sectional area.
The equation of continuity becomes:

$$c_{m1} \cdot r_1 = c_{m2} \cdot r_2 \quad \longrightarrow \quad c_{m1} = \frac{c_{m2} \cdot r_2}{r_1} \tag{2.22}$$

The moment of momentum equation (the Euler equation applied across the diffuser with no work input from inlet to outlet) gives:

$$c_{u1} \cdot r_1 = c_{u2} \cdot r_2 \quad \longrightarrow \quad c_{u1} = \frac{c_{u2} \cdot r_2}{r_1} \tag{2.23}$$

Combining these equations shows that the flow angle in the diffuser remains constant as the radius increases, giving rise to a flow path known as a logarithmic spiral:

$$\tan(\alpha_1) = \frac{c_u}{c_m} = \tan(\alpha_2) = constant \tag{2.24}$$

If there are no losses, the total pressure remains constant

$$p_{tot} = p_2 + \frac{1}{2}\rho c_2^2 = p + \frac{1}{2}\rho c_1^2 \tag{2.25}$$

The ideal static pressure recovery coefficient is given by

$$C_p^{id} = \frac{p_1 - p_2}{\frac{1}{2}\rho c_2^2} = \frac{\frac{1}{2}\rho c_2^2 - \frac{1}{2}\rho c_1^2}{\frac{1}{2}\rho c_2^2} = 1 - \frac{c_1^2}{c_2^2} = 1 - \frac{r_2^2}{r_1^2} \tag{2.26}$$

Thanks to the equation 2.26 it's possibile to highlight two important aspects of vaneless diffusers. First, the ideal static pressure recovery is a function of the diffuser radius ratio (Fig. 2.19). If the outlet radius is twice the inlet radius, the outlet velocity is halved, the kinetic energy drops to 25% and the ideal pressure recovery is 0.75. This represents a very good diffuser given the ease of manufacture and simplicity of the design with no vanes. It is able to match the performance of an optimal vaned diffuser. The disadvantage is that the outer diameter of the stage becomes large, although there are many industrial applications where outer diameter is not limited and, in these cases, the increased outer diameter is not relevant. Vaneless diffusers with a radius ratio above 2 tend not be used because the friction losses in such long diffusers are high, and this increased length offers only a negligible increase in pressure recovery. Brown and Bradshaw [8] showed that with a volute, no improvement is obtained with a radius ratio above 1.8, and in fact most vaneless diffusers accept a compromise at a ratio of 1.6 or below. Where space is limited, a reasonable pressure rise can be attained with a more compact vaneless diffuser.

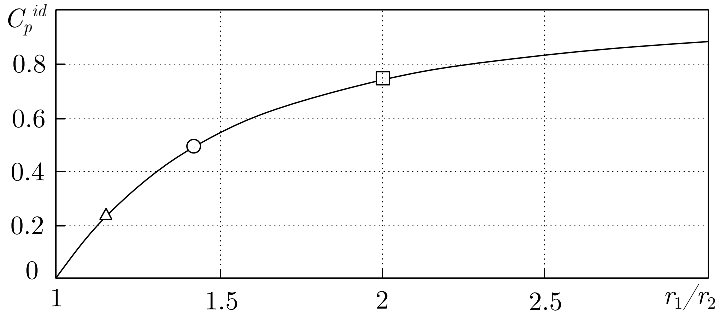

Figure 2.19: Ideal pressure recovery of a vaneless diffuser for different radius ratios [8].

2.4 Losses

During the operation of a centrifugal compressor, it's important to define all the different sources of losses that affect the process. As it's known, losses result in a rise in entropy [1] and in a reduction in stagnation pressure compared to the inlet value or to an ideal value. At a microscopic level the losses may be thought to have a single cause, viscous shearing leading to a rise in internal energy, but from the aerodynamic point of view working at a macroscopic level the sources of loss are very different. According to Cumpsty [3], a list of possible loss sources is:

- Drag losses
- Mixing losses
- Shock losses
- Shear losses

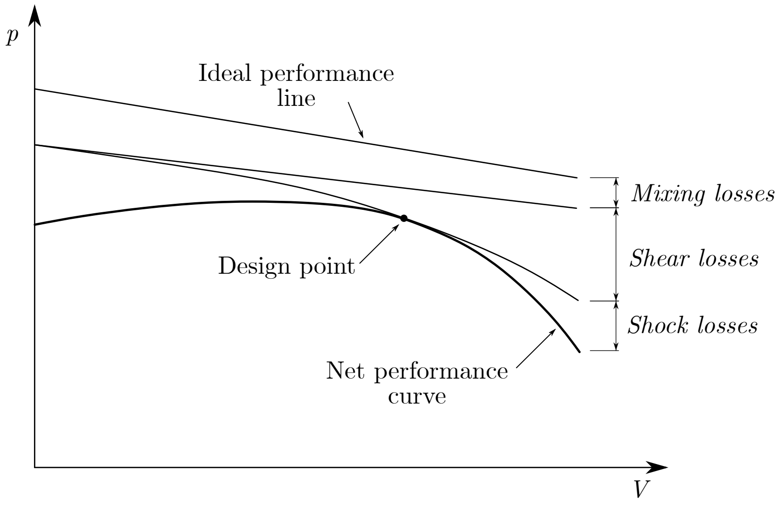

Figure 2.20: Pressure-volume diagram for a centrifugal compressor showing how the various losses give the characteristic curved shape [16].

Drag losses

The effect of drag alone may be seen by considering incompressible flow through a cascade of uncambered and unstaggered blades as illustrated in Fig. 2.4. Upstream of the cascade, the conditions are uniform while at the trailing edge, the velocity is not uniform anymore with a further variation of the downstream static pressure.

---

[1] Actually the equivalence of entropy rise and fall in stagnation pressure is only true for adiabatic flow, but this is usually an acceptable assumption for compressors.

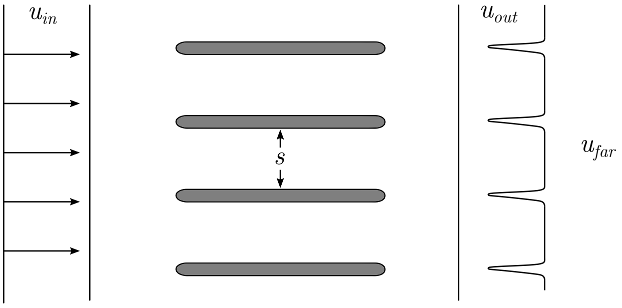

Figure 2.21: Loss production by a cascade of uncambered and unstaggereg plates [3].

This phenomenon, which is also known as blockage, can be thought of as a reduction of the effective section, relative to the actual geometric section available, within which the flow can pass. Flow separation is the primary factor in compressor aerodynamic blockages. Once split, the flow no longer follows the wall's surface and forms recirculation zones that limit the amount of space available for the upstream flow. Hence, separation and obstruction can alter the flow distribution locally, resulting in "virtual" zones of convergent or divergent flow that significantly alter the pressure levels developing throughout the compressor.

Mixing losses

The flow mixing usually occurs in very different and complicated ways in turbomachinery and the flow is generally three-dimensional. Mixing is normally recognized as the non-uniformity of the flow and can be encountered in several zones of the compressor: the most important ones are the tip clearances between impeller blades and shroud and the impeller exit characterized by a jet-wake type of flow. When a boundary layer separates after being accelerated or decelerated, mixing is likely to occur because the flow is no longer able to return to its initial conditions through a thermodynamically reversible process.

Shock losses

The shock loss is an irreversibility that occurs when a flow is decelerated by a single normal shock and the deceleration can be more nearly reversible if it takes place in a series of weaker oblique shocks. Transonic flow is a characteristic of impeller flow fields that occurs when velocity exceeds the limit of Mach = 1 in particular zones, resulting in the formation of enormous dissipative zones known as shock waves. An abrupt rise in pressure and a drop in speed are experienced by the flow over shock waves. When there is a choke present and there is a high rotational speed, transonic flow manifests. The flow via the compressor can not be increased at any point, particularly at choke. Losses resulting from shock waves and compressible flow effects grow quickly as the local Mach number rises. The combined actions of heat transmission [17] and viscous dissipation in a compression shock lead to a rise in entropy.

In addition, it's commonly known that boundary layers often divide after passing through a shock, making blocking effects very difficult to forecast. In experiments, shock waves and their effects are particularly difficult to record, and CFD simulations cannot capture their progression adequately (RANS models, in particular).

Shear losses

Shear loss takes place whenever there are very steep velocity gradients that its magnitude is of concern. These regions are shear layers including boundary layers, wakes, and the regions dividing fast and slow regions of separated flow.

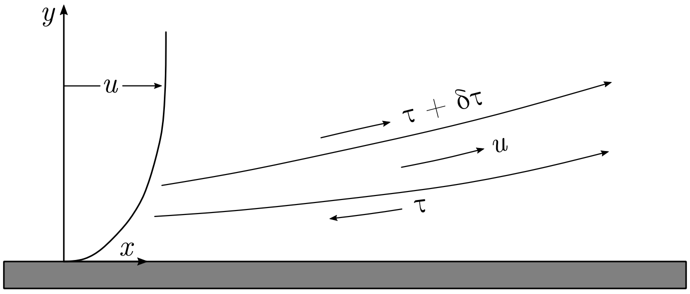

Figure 2.22: Velocity profile and shear stresses operating close to a solid surface [3].

Due to the no-slip situation, there is an extremely steep velocity gradient close to solid barriers, which results in significant frictional losses and the wall shear stress increases with increasing the velocity gradient:

$$\tau = \mu \frac{\partial u}{\partial y}|_{y=0} \tag{2.27}$$

Furthermore, the skin friction increases when a boundary layer is turbulent because the velocity profile at the wall is steeper. Indeed, the impeller and diffuser's free-stream flow, is incredibly turbulent and highly non-uniform, leading to enormous pressure and velocity gradients that have an impact on the shear stress and the progress of the boundary layer.

3

Numerical model

Fluid dynamics deals with the study of how fluids move. The microscopic behavior of a fluid is described by a set of complex mathematical equations that involve partial derivatives. These equations allow us to analyze changes in important properties of the flow, such as pressure, temperature, density, and velocity, throughout the entire fluid region. Fluid dynamics problems are often challenging because they involve intricate and highly nonlinear phenomena.
Additionally, there are no known mathematical solutions for the complete set of equations known as the Navier-Stokes equations.

The advent of Computational Fluid Dynamics (CFD) has transformed the field by enabling us to solve approximations of the governing equations using powerful computers. This computational approach allows us to investigate fluid flows in complex three-dimensional shapes that exhibit a high level of complexity. However, computational resources are limited, which means that we must make assumptions about the flow in order to reduce the number of variables and the time needed for calculations.

Inside a radial compressor, the flow cannot be considered incompressible because it reaches a very high velocity in the region close to the blades. Therefore, the condition $\mathrm{M} < 0.3$ is violated in a significant portion of the region and so indicating that the flow becomes transonic at high rotation rates and thus the variations in density cannot be neglected. Furthermore, both viscosity and turbulence are crucial factors in accurately estimating losses. Assuming that the flow is inviscid and fully laminar would lead to incorrect results.

In the upcoming sections, we will introduce the compressible Navier-Stokes equations. We will then shift the discussion to the Reynolds-Averaged Navier-Stokes (RANS) equations and models that account for the effects of turbulence. Finally, we will provide an overview of some fundamental aspects of Computational Fluid Dynamics.

3.1 Governing equations

Three essential equations are solved for in Ansys CFX in order to capture the flow characteristics and its evolution through the compressor. They are called the governing equations in the subject of fluid mechanics and are the unsteady Navier-Stokes equations. The Navier-Stokes equations are the conservation of mass (continuity), the conservation of momentum, and the conservation of energy, and are defined below in cartesian tensor notation.

The continuity equation

$$\frac{\partial \rho}{\partial t} + \frac{\partial}{\partial x_i}(\rho u_i) = 0 \tag{3.1}$$

The momentum equation

$$\frac{\partial}{\partial t}(\rho u_i) + \frac{\partial}{\partial x_j}(\rho u_i u_j) = -\frac{\partial p}{\partial x_i} + \frac{\partial \sigma_{ij}}{\partial x_j} + \rho F_i \tag{3.2}$$

The conservation of energy

$$\frac{\partial(\rho e_0)}{\partial t} + \frac{\partial(\rho u_i e_0)}{\partial x_i} = -\frac{\partial(p u_i)}{\partial x_i} - \frac{\partial q_i}{\partial x_i} + \frac{\partial(u_j \sigma_{ij})}{\partial x_i} \tag{3.3}$$

Where: t = time, ρ = density, u = fluid velocity, and i, j = 1,2,3 are cartesian coordinates, p = pressure, σ = stress tensor, F_i = external force in the system, q_i = heat flux.

It is assumed that no external forces are acting on the system, and thus $F_i = 0$. Furthermore, the operating gas considered in the analysis is air, which is assumed as calorically perfect, therefore the specific heat at constant volume(C_v) and at constant pressure (C_p) is constant. This gives the two relations:

$$e = c_v \cdot T \tag{3.4}$$

and then,

$$h = c_p \cdot T \tag{3.5}$$

The air is a Newtonian fluid meaning that the viscous stresses emerging from the fluid are linearly. This is true at every point in the fluid, so a constitutive relation for the Newtonian fluid can be described as:

$$\sigma_{ij} = 2\mu S_{ij} - \frac{2}{3}\mu S_{kk}\delta_{ij} \tag{3.6}$$

Where μ denotes the dynamic viscosity of the fluid, δ_{ij} is the Kronecker delta. δ_{ij} is always in unity for $i = j$ and zero for $i \neq j$. The rate of deformation, S_{ij} is described as:

$$S_{ij} = \frac{1}{2}\left(\frac{\partial u_i}{\partial}x_j + \frac{\partial u_j}{\partial x_i}\right) \tag{3.7}$$

The gas will because of the compression in the system get a rise in temperature, which leads to the assumption that the dynamic viscosity is temperature-dependent. This is described by Sutherland's law:

$$\frac{\mu}{\mu_0} = \left(\frac{T}{T_0}\right)^{1.5}\left(\frac{T_0 + T_s}{T + T_s}\right) \tag{3.8}$$

where $\mu_0 = 1.7231 \cdot 10^{-5}$ $[\frac{kg}{m \cdot s}]$ is the reference viscosity at $T_0 = 273.15$ K, and $T_s = 111$ K is the Sutherland's constant.

Reynolds-Average Navier-Stokes

The above equations are used for simpler cases with steady laminar flow. However, for the radial compressor, the flow is highly turbulent and chaotic, whereas the general flow type is in fact turbulent, with some small-scale regions with laminar flow.

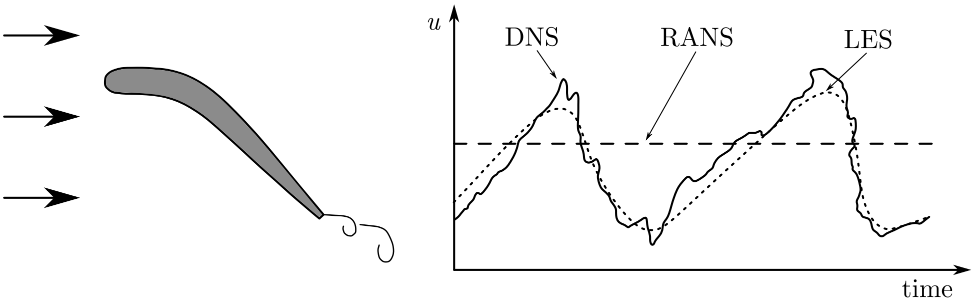

Figure 3.1: Principle of the DNS, RANS, and LES approaches. Typical time evolutions of velocity that these three methods would provide downstream of a trailing edge at a large angle of attack [18].

Currently, methods that resolve the large turbulent eddies (LES) are used for vehicle aerodynamics at moderate Reynolds numbers [19] and are rarely used on centrifugal compressor aerodynamics [20]. In academic research, small-scale issues are typically explored with direct numerical simulation (DNS), resolving the whole turbulence spectrum [21]. Reynolds-Averaged Navier-Stokes techniques (RANS) simulate the impact of the turbulence on the mean flow quantities rather than resolving the entire turbulence spectrum in order to minimize the computing work.

In a turbulent flow, the flow parameters vary with time in the form of unsteady fluctuations. To capture the characteristics of a turbulent flow, a method called Reynold's decomposition is used, where each quantity of the flow (i.e velocity or pressure) is split up into its time-averaged and time-dependent fluctuation part. For instance, the velocity:

$$u = \bar{u} + u' \tag{3.9}$$

where u denotes the time-averaged and u_0, the fluctuation part. In addition to Reynold's decomposition, when dealing with a compressible flow as in a compressor, density variations due to turbulent fluctuations have to be considered.
This introduces the Favre averaging, which is a density-weighted average that splits the previously mentioned quantity into a once again time-averaged and time-dependent fluctuating part:

$$u = \tilde{u} + u'' \tag{3.10}$$

where the difference between Reynold's decomposition and Favre averaging is the density-weighted averaging applied in the latter, so the velocity u is related to the density via:

$$\tilde{u} = \frac{\overline{\rho u}}{\bar{\rho}}$$

Applying Favre averaging to the Navier-Stokes equations (Eqs. 3.1-3.2-3.3) yields the Reynold-Averaged Navier-Stokes equations (RANS equations):

$$\frac{\partial \bar{\rho}}{\partial t} + \frac{\partial}{\partial x_i}\left(\bar{\rho}\tilde{u}_i\right) = 0 \tag{3.11}$$

$$\frac{\partial\left(\bar{\rho}\tilde{u}_i\right)}{\partial t} + \frac{\partial\left(\bar{\rho}\tilde{u}_i\tilde{u}_j\right)}{\partial x_j} = -\frac{\partial \bar{p}}{\partial x_i} + \frac{\partial \bar{\sigma}_{ij}}{\partial x_j} + \frac{\partial \tau_{ij}}{\partial x_j} \tag{3.12}$$

$$\begin{aligned} &\frac{\partial}{\partial t}\left(\bar{\rho}\left(\bar{e} + \frac{\tilde{u}_i\tilde{u}_j}{2}\right) + \frac{\overline{\rho u_i'' u_i''}}{2}\right) + \frac{\partial}{\partial x_j}\left(\bar{\rho}\tilde{u}_j\left(\bar{h} + \frac{\tilde{u}_i\tilde{u}_i}{2} + \tilde{u}_j\frac{\overline{\rho u_i'' u_i''}}{2}\right)\right) = \\ &= \frac{\partial}{\partial x_j}\left(\tilde{u}_i\left(\bar{\sigma}_{ij} - \overline{\rho u_i'' u_i''}\right)\right) + \frac{\partial}{\partial x_j}\left(-\bar{q}_j - \overline{\rho u_j'' h''} + \overline{\sigma_{ij} u_i''} - \rho u_j''\frac{u_i'' u_j''}{2}\right) \end{aligned} \tag{3.13}$$

The averaged version of the momentum equations (Equation 3.12) are often known as the Reynolds-Averaged Navier Stokes equations (RANS) with Favre averaging. One can instantly tell that the averaging introduces the new word τ_{ij}, which is defined as follows:

$$\tau_{ij} = -\overline{\rho u_i'' u_j''} \tag{3.14}$$

The Reynolds stress tensor, a symmetric matrix with six different components, is the name given to this expression. These elements explain the macroscopic momentum transfer at turbulent scales. The addition of the Reynolds stress tensor adds six more unknown variables to the problem, necessitating the use of modeling techniques to finish the system of equations.

Furthermore, the steady and unsteady RANS method was adopted for the present study as it is a sufficiently accurate numerical method to capture the pressure fluctuations in the volute of a centrifugal compressor.

3.1.1 Eddy-viscosity models

The Reynolds stress tensor can be modeled using the eddy-viscosity model. The eddy-viscosity closure model's time-averaged velocity gradients are described by the following formulation, which is credited to Boussinesq:

$$-\overline{\rho u_i'' u_j''} = 2\mu_T S_{ij} - \frac{2}{3}\mu_T S_{kk}\delta_{ij} \tag{3.15}$$

where μ_T is the turbulent eddy viscosity, which as it accounts for the momentum transfer generated by turbulent eddies, is a local quantity of the flow. The Stokes hypothesis for laminar flow is comparable to the Boussinesq eddy-viscosity assumption. Although it has a straightforward formulation, the assumptions it contains could restrict the accuracy of the findings this turbulence model produces.

Eddy-viscosity models, as proposed by Wallin and Johansson [22], are good for simulating attached thin boundary layers and two-dimensional flows, but they have a number of downsides when non-equilibrium flows, boundary layer separation, or effects due to swirl, rotation, and curvature are taken into account. Therefore, it appears that the application of this straightforward model is constrained to basic wall-bounded flows; strongly whirling flows, such as those that arise inside centrifugal compressors, could not be accurately anticipated. For this reason, the community of fluid dynamics has developed a number of sophisticated turbulence models for aeronautical and turbomachinery applications.

SST Turbulence model

The $k - \omega$ turbulence model is a popular method for solving RANS equations with eddy-viscosity models in industrial research. This model involves solving two transport equations for the turbulence kinetic energy k and the specific dissipation rate ω, which are used to model the turbulence. The $k-\omega$ model was first developed by Wilcox and is now widely used. The resulting $k-\omega$ model takes the form of transport equations for k and ω, which are used to predict turbulence and take the following form:

$$\left(\frac{\partial}{\partial t}+\bar{u}_i\frac{\partial}{\partial x_j}\right)K=P-C_\mu K\omega+\frac{\partial}{\partial x_j}\left[\left(\nu+\frac{\nu_T}{\sigma_K}\right)\frac{\partial K}{\partial x_j}\right] \tag{3.16}$$

$$\left(\frac{\partial}{\partial t}+\bar{u}_i\frac{\partial}{\partial x_j}\right)\omega=\left((C_{e1}-1)\frac{\omega}{K}\right)P-(C_{\omega 2}-1)C_\mu\omega^2+\frac{\partial}{\partial x_j}\left[\left(\nu+\frac{\nu_T}{\sigma_K}\right)\frac{\partial K}{\partial x_j}\right] \tag{3.17}$$

where C_μ, σ_K, C_{e1} and $C_{\omega 2}$ are experimental modeling coefficients [18]. Turbulent viscosity is here defined as $\nu_T=k/\omega$ while production of turbulent kinetic energy (P) and specific turbulence dissipation rate (ω) are defined as follows:

$$P=-\overline{u_i'u_j'}\frac{\partial\bar{u}_i}{\partial x_j}=2\nu_T S_{ij}S_{ij} \tag{3.18}$$

$$\omega=\frac{\nu}{C_\mu K}\,\frac{\partial\overline{u_i'}}{\partial x_j}\,\frac{\partial\overline{u_i'}}{\partial x_j} \tag{3.19}$$

The $k-\omega$ model has some advantages over other two-equation turbulence models, such as the $k-\varepsilon$ one. It first provides more accurate estimates of boundary layer flows with pressure gradients. Additionally, $k-\omega$ equations can be integrated into the wall even with small grid spacing, in contrast to $k-\varepsilon$ equations, which become singular at the wall and are invalid in the very near-wall area unless computationally expensive low-Re formulations are used ($y^+\sim 1$). This method's fundamental issue is how turbulent interfaces, specifically the boundary layer edge, are handled, which leads to an unphysical sensitivity to the free-stream values of k and ω. Additionally, it is difficult to estimate when and how much flow separation will occur when there are negative pressure gradients.

Menter [23] created the *Shear-Stress-Transport* (SST) $k-\omega$ model to address these issues. This model fixes the shortcomings of the traditional $k-\varepsilon$ model by including cross-diffusion components and production limiters in the formulation of the eddy-viscosity. Additionally, the $k-\varepsilon$ formulation in the free-stream can be utilized in place of the $k-\omega$ model to solve the boundary layer since it has been shown to be less sensitive to the characteristics of the inlet free-stream turbulence. Due to its ability to catch flow separation, this model has been adopted for this thesis work.

Turbulence boundary layer

The Reynolds number in a centrifugal compressor is usually determined as:

$$Re = \frac{\omega L^2}{\nu} \tag{3.20}$$

where ω denotes the rotational velocity and L is the height of the impeller outlet diameter. The Reynolds number associated with flows inside centrifugal compressors falls within the range of 10^6 to 10^7. High-turbulence flows are present here because turbulent boundary layers are forming along the walls.

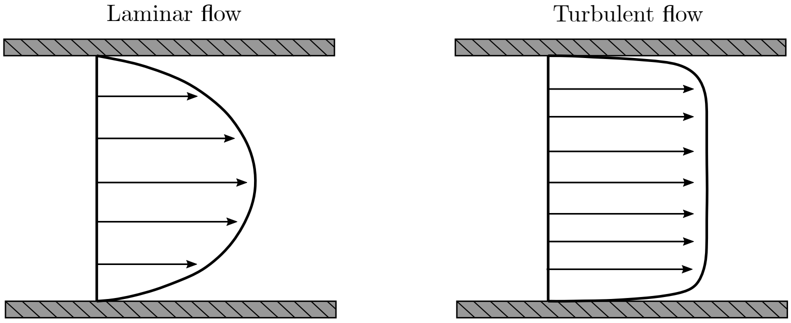

Figure 3.2: Comparison of laminar and turbulent velocity profiles in a duct.

In comparison to laminar flows, these boundary layers have steeper velocity gradients along the wall, leading to higher levels of wall shear stress (denoted by the symbol τ_w). However, turbulent boundary layers' structure exhibits a great level of complexity.

For all flow types (laminar or turbulent) the non-dimensional length scale parameter, based on Spaldings law of the wall [24], can be evaluated as:

$$y^+ = \frac{\rho y_p \cdot \sqrt{\tau_w/\rho}}{\mu} = \frac{y_p \cdot u_\tau}{\nu} \tag{3.21}$$

where the y_p defined the coordinate normal to the wall. The friction velocity is defined as:

$$u^+ = \frac{u}{u_\tau} \tag{3.22}$$

In the case of free shear flows, the SST model is equivalent to the $k - \varepsilon$ model. It is challenging to estimate separation from a smooth surface at close distances, especially when there are unfavorable pressure gradients present, as in the compressor. The SST model and an automated wall function are employed for simulations throughout this work.

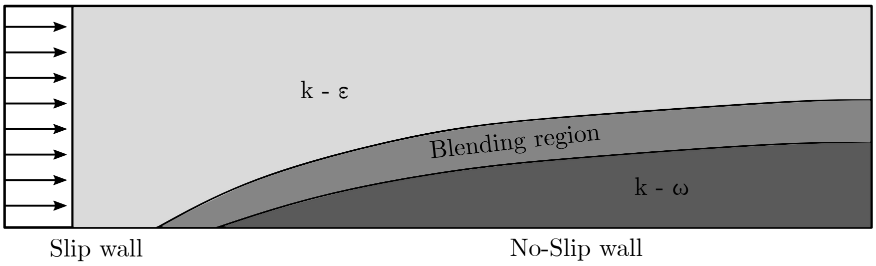

Figure 3.3: Graphic representation of the evolution of the wall functions.

When the mesh is improved, the SST model will switch from a low-Re number form to a wall function formulation utilizing the automated near-wall treatment. The viscous sub-layer solution and the logarithmic profiles will blend smoothly to implement this change. In order to sufficiently resolve the wall, at least 10 layers of inflation should be required. This is because the low-Re formulation is used for $y^+ < 2$. The SST model with automated near-wall treatment will switch between low-Re and wall function for $y^+ \leq 11{,}25$ since the condition of $y^+ < 2$ is challenging to adapt in all areas of the geometry. The simulation does not have to move between distinct wall functions when the model is resolved using an inflation layer, which may result in a higher level of solver accuracy.

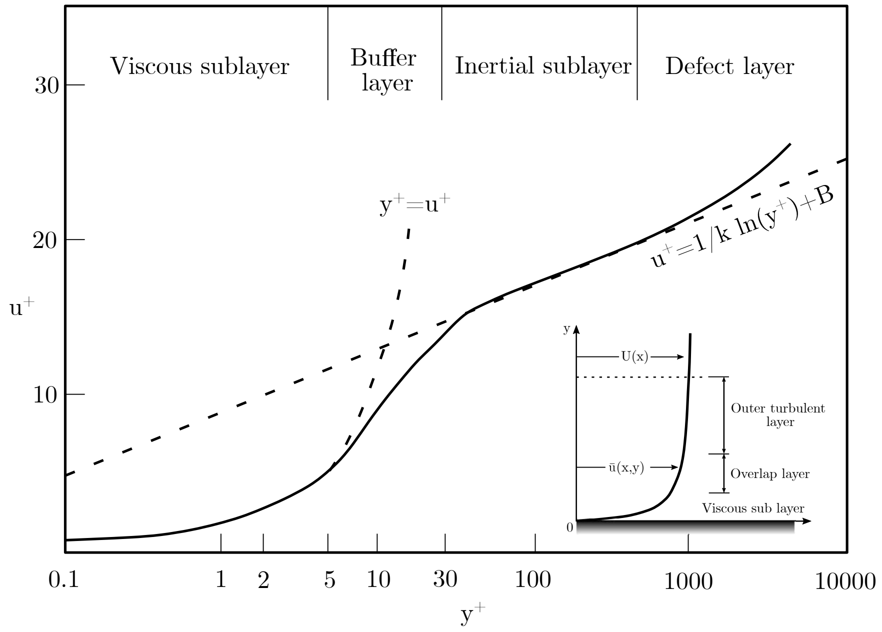

Figure 3.4: Theoretical dimensionless velocity profile in the near-wall region.

Figure 3.4 presents a graph that depicts the correlation between u^+ and y^+ along the wall-normal direction. Within this graph, distinct regions can be identified. The first region is the viscous sublayer, which spans from $0 < y^+ < 5$. This sublayer is located closest to the no-slip wall. Despite the dominance of viscosity in this region, the turbulent fluctuations have minimal absolute amplitudes.

Additionally, this area exhibits the relationship $u^+ = y^+$. Modeling the flow characteristics within the viscous sublayer poses significant challenges due to the requirement of a very fine near-wall grid. Consequently, both experimental and numerical approaches encounter difficulties in accurately capturing the flow properties in this region.

The log-law area is located between $y^+ \sim 70$ and $y/\delta < 0.15$ (where δ denotes the height of the boundary layer).

The law of the wall is valid in this region and holds:

$$u^+ = \frac{1}{k} \cdot \log(y^+) + B \tag{3.23}$$

where k is the von Karman constant and B is an empirical coefficient. The buffer layer is the area that stretches between the viscous sublayer and the log-law zone. The highest streamwise turbulent intensity and turbulence output may be recorded in this area. Any streamwise velocity outside the log-law zone, or for $y/\delta > 0.15$, is combined with the free-stream velocity. This zone, known as the "wake region" stretches from the bulk flow edge to 15% of the thickness of the boundary layer.

3.2 Solvers

In the course of this thesis, the compressor was numerically analyzed and thus a CFD analysis was carried out by setting up the same configuration (geometry, mesh, boundary conditions, and solver settings) for two different solvers: TRACE and Ansys® CFX.
This choice was fundamental to obtain a better results comparison about the flow field behavior and about all the numerical results since CFX has been widely accepted as a commercial CFD solver in the applications of turbomachinery thanks to its robustness, computation efficiency, satisfying calculation accuracy, and the ability for parallelization. As mentioned before, the Demag® KG3.32 compressor was used as a reference study to compare all the results obtained by the simulations.

The preliminary set-up of the computational model consisted of the inlet pipe, the impeller, and the vaneless diffuser. In this phase, for symmetry reasons and because the volute was still not included, it was modeled as a single blade passage with periodic boundary conditions. At this point, the computed performance map (pressure ratio and efficiency versus volume flow rate) was compared to experimental values given by the compressor in the laboratory.

Successively, the volute and the outlet pipe were included in the previous single passage configuration, and the interface between the stationary parts and the rotor was modeled by a mixing-plane approach. Here, the performance map was updated in order to observe the influence of the volute on the overall performance of the compressor.

As already mentioned, a wrong designed volute will produce losses that can hurt not only the overall efficiency but also the flow stability. A volute that is oversized will incur losses due to over-diffusion of the flow, and an undersized volute will fail to completely recover the dynamic pressure from the radial component of the flow entering the volute. However, to fully capture the flow behavior inside the volute, the final analysis needed to extend the model to a full-annulus 360°configuration,
In conclusion, this chapter of the CFD study includes the simulation approach, the mesh model, the simulation setup and the CFD result discussion.

As the study progresses, various simulation methods have been utilized as follows:

- Steady single-passage simulation (impeller only)
- Steady single-passage simulation (full setup)
- Steady and transient full-annulus 360°simulation

These several CFD analyses will be examined from simple to complex in order to examine different aspects of flow distortion. Firstly, the steady single-passage simulation enables a quick turn-around of performance map reproduction.
Secondly, the steady full-annulus model introduces the 360°flow non-uniformity. As a next step, the transient full-annulus simulations further take into account the flow unsteadiness along the circumferential direction, which best represents the compressor operation conditions in reality.
Finally, the transient simulation is considered as an attempt to evaluate the volute pressure distribution in the time and frequency domain in order to identify how the variation of inlet parameters affects the stability of the compressor.

3.2.1 TRACE

Since the early 1990s, the DLR Institute of Propulsion Technology in Cologne has been developing the CFD code TRACE (Turbomachinery Research Aerodynamic Computational Environment) to investigate complicated flows in turbomachinery. TRACE is a three-dimensional Reynolds-averaged Navier-Stokes flow solver and it is used outside of DLR by academic institutions and other research organizations to conduct scientific analyses of turbomachinery flows. TRACE is also used by MTU Aero Engines and Siemens Energy for the design and optimization of turbomachinery components in industrial design settings.

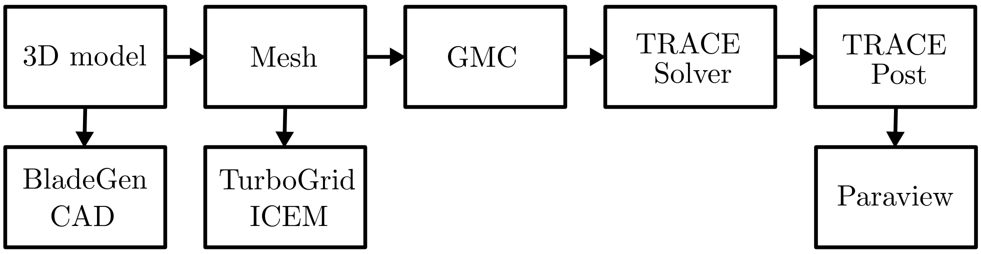

Figure 3.5: Workflow for TRACE solver.

The simulation system TRACE consists of the modules PREP, TRACE, and POST.

- PREP is a pre-processor for mapping blade eigenmodes of a FEM calculation on a CFD grid for flutter or forced response analysis. In this phase, a Graphical User Interface (GUI), called TRACE GMC was used to define all the boundary conditions and the solver settings.
- TRACE (solver) is the hybrid (structured and unstructured) flow solver with nonlinear solvers in the time and in the frequency domain, a linearized module in the frequency domain, and an adjoint flow solver.
- POST is a comprehensive software tool for the global analysis of stationary and non-stationary multi-stage turbomachinery simulations.

TRACE does not include any modules that can display both the results of the 3D simulation and the post-processed data, consequently, an extra software must be used. An open-source, cross-platform data analysis and visualization tool called Paraview is used for this purpose. Paraview, which is intended to handle enormous data sets, enables interactive viewing of a variety of data types, including CAD files, results from 3-D simulations, and both organized and unstructured grids. The program also comes with sophisticated capabilities for data processing and analysis, including cutting and clipping planes, streamlines, and probing lines. Figure 3.5 shows the workflow procedure adopted for numerical simulation with TRACE solver.

3.2.2 Ansys CFX

In this thesis, steady-state and transient CFD simulations are carried out using Ansys CFX. This CFD program was chosen because it can handle rotating domains and is appropriate for modeling turbomachinery flows. Direct management of the whole procedure, from the specification of the geometry through the post-processing of the data, is possible from Ansys Workbench. Ansys Workbench's parameter set window, in particular, makes it simple to change the boundary condition and set up any simulations. This tool is very helpful for running steady-state simulations to calculate compressor maps.

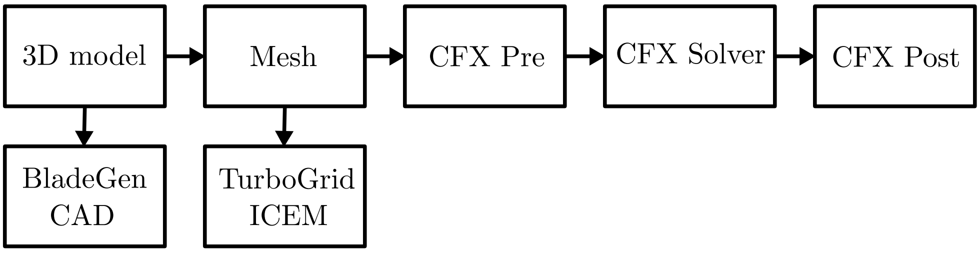

Figure 3.6: Workflow for Ansys CFX solver.

Figure 3.6 shows the usual workflow that is used in Ansys CFX. The creation of the geometry is the initial phase, which is done in Design Modeler through the import and modification of CAD geometries. After that, Ansys Meshing receives the completed design and creates the computational grid. The simulation may be set up in CFX-Pre once the mesh has been created. Boundary/initial conditions, flow characteristics, and any other variables that have an impact on the simulation's outcome can be established here. The output from CFX-Pre is a.def file, which CFX Solver uses to do the computations. The latter completes all computations and numerically solves the flow field; residuals and particular physical quantities defined in CFX-Pre can be observed as the simulation develops. The next step is to display and evaluate the results using the basic post-processing capabilities provided by CFD-Post. The development of a computational mesh is thus necessary since the Ansys CFX solver employs the finite volume approach for spatial discretization. In order to conserve important variables like mass, momentum, and energy, the grid is employed to build finite volumes.

3.3 Geometry and mesh

3.3.1 Single-passage (impeller only)

The initial stage of pre-processing involves the modeling of the geometry, which serves as a model that represents the physical system, in this case, a fluid flow in a centrifugal compressor. In this study part of the geometry was created by the BladeGen® software, which was essential to model the inlet pipe, the impeller, and the vaneless diffuser. Afterward, the volute and the outlet pipe were modeled by means of CAD (Computer Aided Design) software. It is essential to remember that the simulation is for fluid flow and thus the geometry does not correspond to the actual physical structure of the compressor. Instead, it represents the hollow region through which the fluid flows.

For the first part of the study, the geometry was divided into axial-symmetric segments, with a blade in each one. In the present case, the model was split into 15 slices (Fig. 3.7), corresponding to the total number of blades in the compressor.

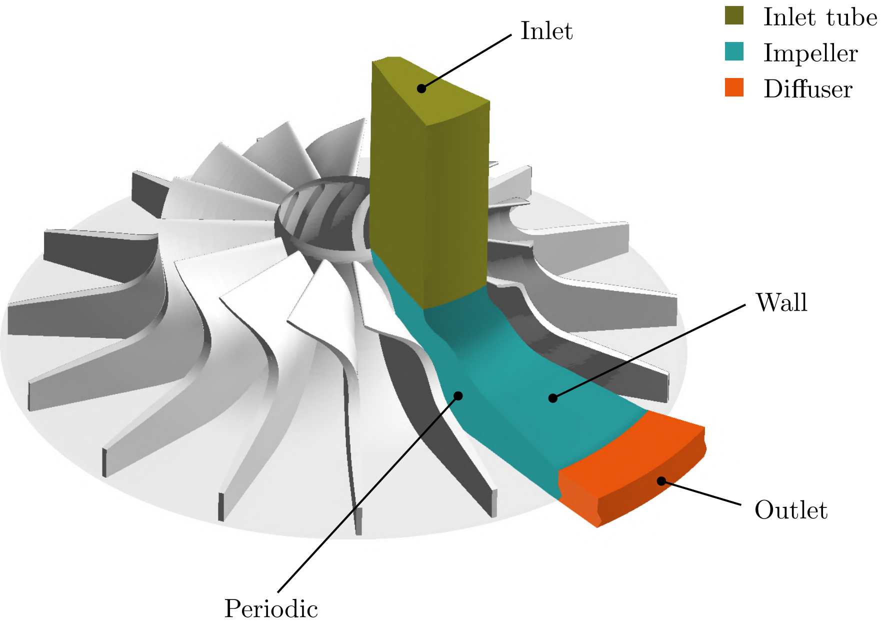

Figure 3.7: Domain setup of a single blade passage.

The following step was to generate the computational grid and it's really important to build the mesh in a method that both captures the geometry's important characteristics and reduces numerical errors. A mesh or grid is the result of discretizing a domain to generate a computational mesh, which is then used to solve equations [**darwish2016finite**]. The meshing process of the first model, so the

partial one without the volute, was carried out by means of the TurboGrid® software, at which it was possible to generate a structured grid (Fig. 3.10).
For the impeller's grid was adopted a "LECircleLowPassage" and "LECutoffBlock1by4" topology (Fig. 3.8) with about 170k hexa elements for a single blade passage.

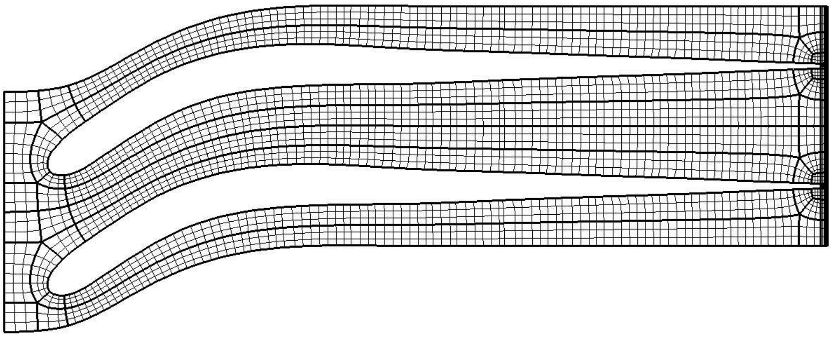

Figure 3.8: Mesh topology of the impeller domain.

In front of the blade, an inlet section had been added to avoid strong influences of the inlet boundary conditions. Behind the trailing edge of the blade, the vaneless diffuser with parallel walls is located. Between the trailing edge and the diffuser inlet, a clearance was defined as $2 \cdot TE_{thickness}$ at which the mixing plane (Fig. 3.10) had been added as the rotor-stator interface.

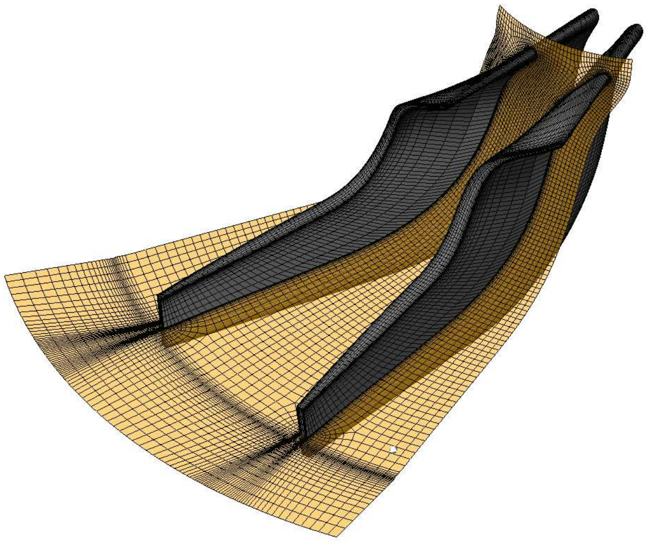

Figure 3.9: Midspan mesh fragments for the blade structured grid.

Structured grids are made up of a series of interconnecting quadrilaterals (2D) or hexahedra cells (3D). A structured grid is organized in rows and columns (i,j,k) of cells (for three dimensions) so that a program sweeping over the entire mesh can directly address the neighboring cells to evaluate differencing expressions.

Consequently, there is a direct relationship between a cell's location in its row and column and the location in the CFD program's arrays used to store physical variables associated with the cell. These grids generally offer a high degree of quality, better alignment, and less memory and time required but at the same time, the grid generation is very difficult for complex geometry. Moreover, it can happen that in order to bend the structured mesh to the physical space being modeled, the cells can take on an odd shape or undesirable size.

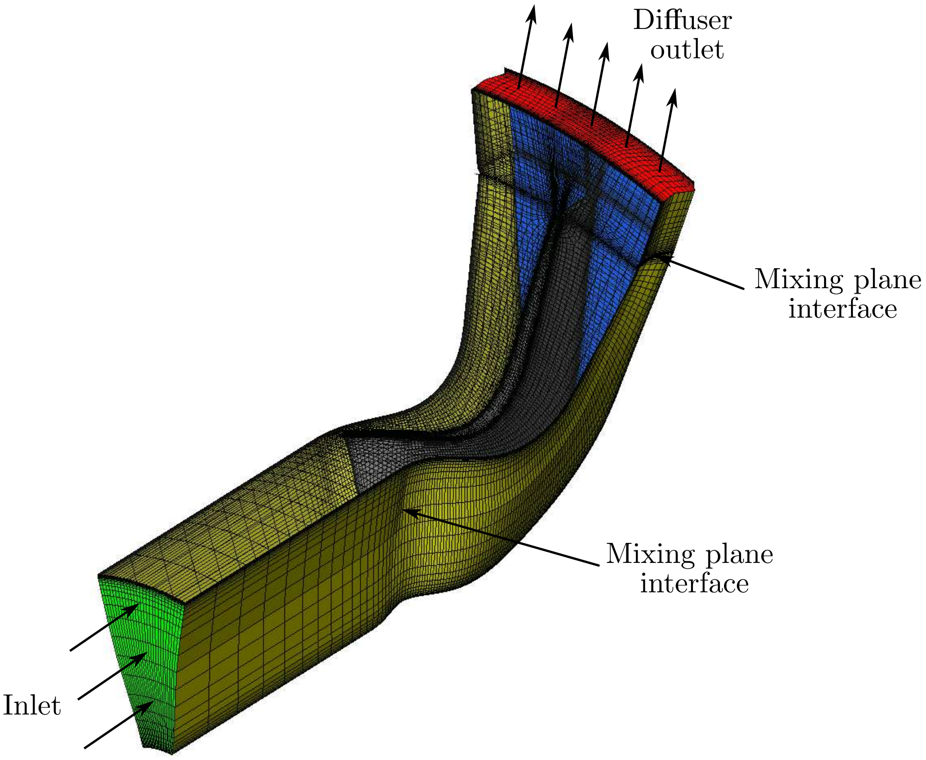

Figure 3.10: Structured grid of the single passage domain

3.3.2 Single-passage (full setup)

In the second phase, the volute was implemented in the single passage configuration. The computational domain of the volute geometries includes the vaneless diffuser, which leads the flow to the volute, the non-axisymmetrical scroll part which goes around the diffuser, and the exit cone which leads the flow to the pipeline. Moreover, an outlet tube with $5 \cdot D_{out}$ length was placed downstream of the volute in order to get a more stable flow thus reducing the possibility of having reverse flow in the outlet boundary condition.

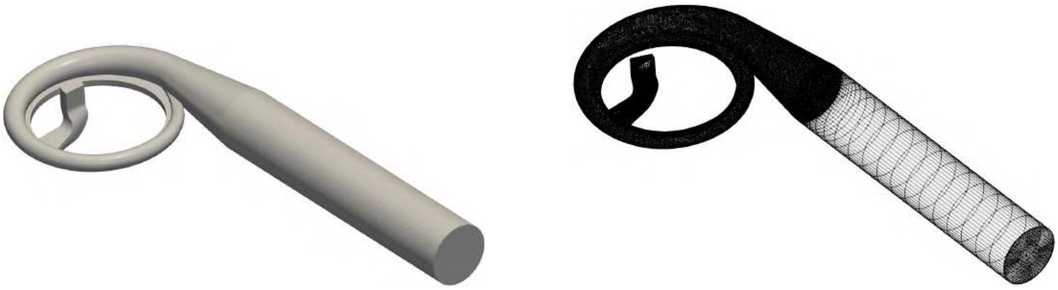

(a) Solid domain **(b)** Mesh of the domain

Figure 3.11: Full setup of the computational domain with the single passage impeller, the volute and the outlet pipe.

For the volute, an unstructured grid was chosen, which was generated with the commercial mesh generator ICEM®. In the wall regions of the volute grid, 6 prism inflation layers had been added while the rest of the grid consists of tetrahedral cells. The grid presents about 1.2 million cells. Conversely, the outlet pipe was made with a structured mesh with an o-grid topology that presents about 37k cells. In this case, no inflation was implemented to the pipe since it was not relevant to get information about the flow behavior in this region of the domain.

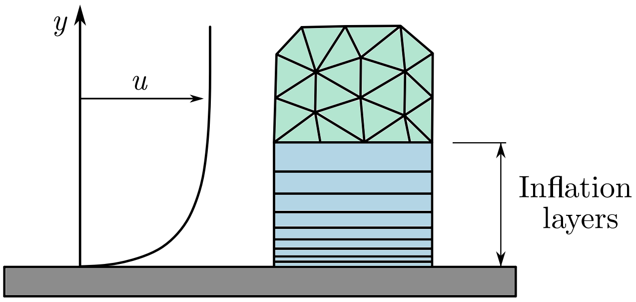

Figure 3.12: Growth of the inflation layers in an unstructured grid.

Unstructured grids have no obvious relationship between neighboring cells and the location of their data in the data structure and thus the location of the cell and the location of the data must be connected using indirect addressing. Therefore each object (e.g. cell) is identified by an arbitrary ID number and they are ordered in an arbitrary way in a 1-D list. Consequently, additional connectivity information has to be provided to identify neighbor objects. Unstructured grids are not fine enough close to the wall, and to resolve the gradients in the RANS simulation, the cells need to be smaller normal to the wall than along the wall. Therefore it was necessary to grow inflation layers (prism layers) underneath the unstructured mesh (Fig. 3.12) in order to provide the thin cells that we need to resolve the gradients.

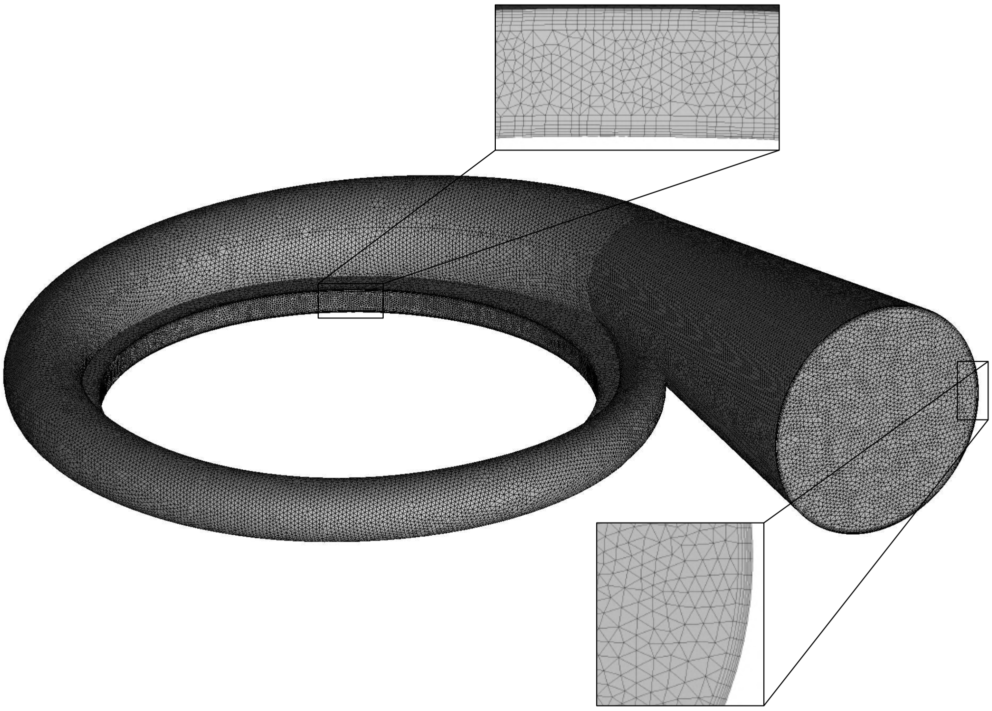

Figure 3.13: Overview of the unstructured grid of the volute.

Furthermore, cells in unstructured grids can be triangles, quadrilaterals, or polygons and have irregular shapes. These grids provide construction flexibility and are advantageous to implement in complex geometries, particularly to capture flow features that are difficult to capture by structured grids. However, this flexibility comes at the cost of more computational effort because the numbering depends also on the local connectivity and the geometric quantity, and not just on the index.

3.3.3 Full-annulus 360°

The full-annulus model may be defined with the full 360°inlet flow conditions model because it can be regarded as a reproduction of every single blade passage by the blade number. As a result, no rotational periodicity needs to be established between adjacent blade passages.
Figure 3.14 shows the full-annulus domain, where the vaneless diffuser was totally integrated into the statoric section of the volute.

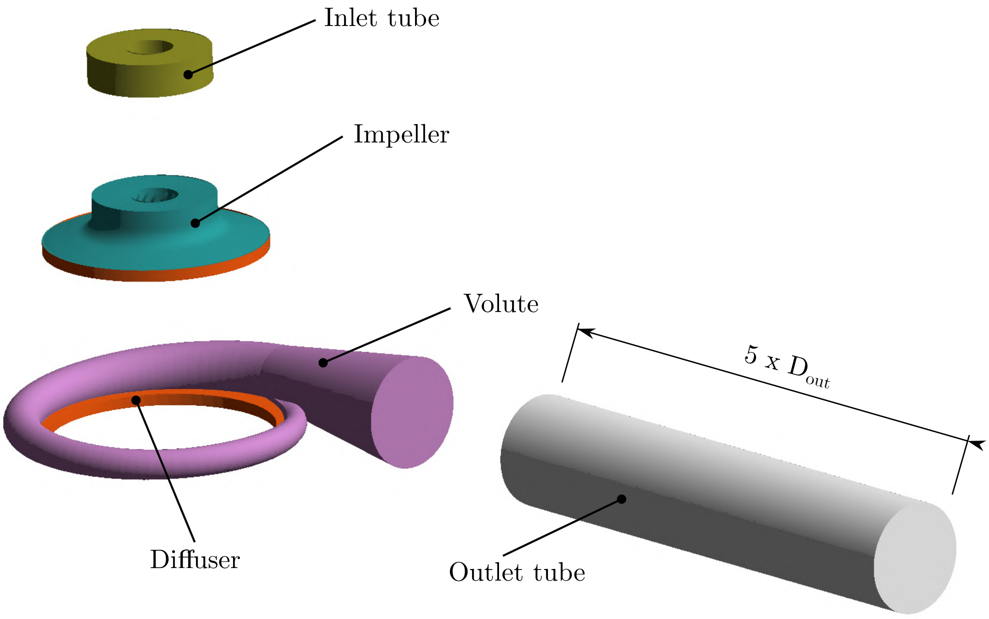

Figure 3.14: Full computational domain of the centrifugal compressor

In the full configuration, the simulation required an important computational effort. For this reason, a distributed parallel run was performed by adopting 40 CPU serial connected in the university cluster system.
The summary of the final grid is reported below:

Part	Grid type	Nodes	Elements
Inlet tube	Structured	207900	181440
Impeller	Structured	2919330	2541120
Diffuser + Volute	Unstructured	328441	1218660
Outlet tube	Structured	39225	36960
Total	-	3497896	3978180

Table 3.1: Mesh statistics of the full-annulus configuration.

Both solvers enable the use of an Automatic Near-Wall treatment (AWT) based on wall functions and Low-Reynolds-Number techniques (LRN) for the SST Menter $k-\omega$ turbulence model. Note that the Reynolds number being discussed

is the turbulent Reynolds number, which has low values in the viscous sublayer (Fig. 3.4) and is dictated by characteristics of the smaller turbulent scales.
The $k-\omega$ equations are directly integrated using LRN techniques across a near-wall mesh. Since no assumptions about the variance of the variables close to the wall are needed, they are often more accurate than wall-function treatments. On the other hand, the majority of low-Re additions to turbulence models are highly complicated, which might harm the numerical method's stability or performance.

Furthermore, to guarantee proper resolution of the boundary layer features, very short mesh length scales in the direction corresponding to the wall are needed. This criterion may also be applied to the wall coordinate y^+, whose low values ($y^+ < 2$ for $k-\omega$ models [25]) often provide high-quality resolution throughout the boundary layer. y^+ can thus be one order of magnitude bigger than the specified limit for actual situations even though this need can be readily accomplished in basic 2D examples. This is because solving highly inflated grids in 3D complicated industrial geometries requires considerable processing resources.

The most popular technique for overcoming this grid resolution requirement is Automatic Near-Wall Treatment, which gradually switches between wall functions and the LRN approach across the boundary layer without sacrificing accuracy (Fig. 3.3). As is shown in figure 3.4, for low y^+ values ($y^+ \sim 1$), equations are integrated into the wall, whereas wall functions are used for higher ones ($y^+ \sim 30$). Within this range, a combination of the two formulations is used where the solver is in charge of switching between the two formulations, which greatly relaxes the constraint on grid refinement.

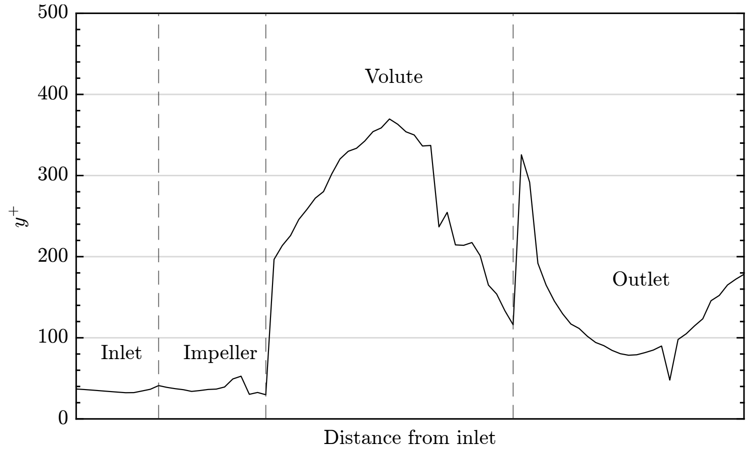

Figure 3.15: Average non-dimensional wall distance y^+ for the near-wall cells of the computational domain.

The $\overline{y^+}$ value is around 30 in the inlet tube, 30 in the impeller, 150-350 in the volute, and 100-200 in the outlet pipe. The grid density close to the surfaces would be adequate for the impeller part since the local y^+ is below the limit value of 70 in about 95% of the surface. As it illustrated in figure 3.16, the y^+ reaches a very high value in the region close to the trailing edge, where the fluid velocity is very high. Conversely, the grid density in the diffuser, volute, and outlet pipe is coarser, indeed a high Reynolds number turbulence with a wall function was used. Due to the boundary layer's propensity to separate as a result of the large pressure gradient, the coarse grid may provide issues, particularly in the diffuser and volute. The total number of elements is already significant and the computing time is somewhat lengthy and thus, the grid was constructed in this manner in order to obtain a qualitative result that was satisfactory given the computer resources available. Moreover, even with a coarse grid and the chosen turbulence model, it is still feasible to get rather excellent results [26], but this does not suggest that the computation would always be accurate with a coarse grid.

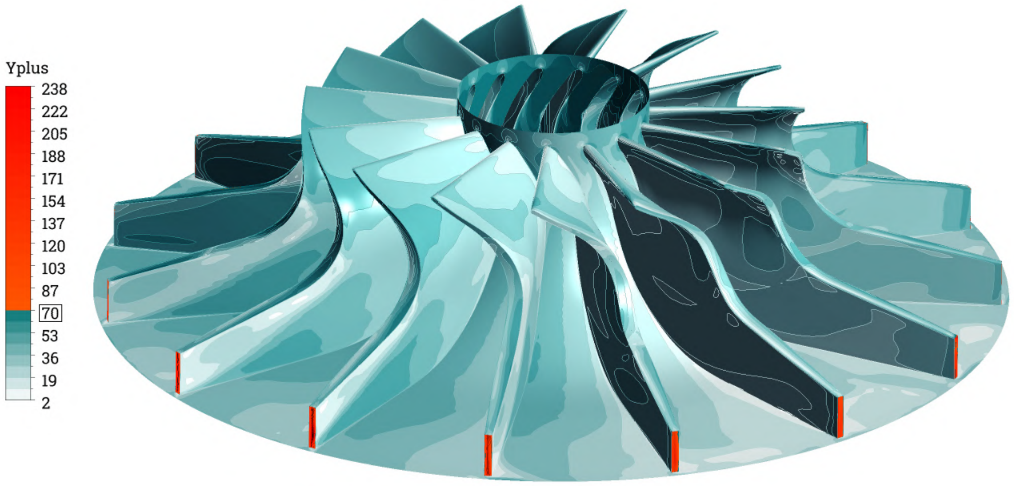

Figure 3.16: y^+ values in the impeller domain.

3.4 Boundary conditions

The numerical model's boundary conditions rely on the primitive variables p, u, T instead of the conserved variables. The benefit lies in the fact that these primitive variables are obtained from experimental observations and can be directly employed as boundary conditions in the simulations. The inlet boundary conditions are taken from the data of the KG3.32, that were measured in the university lab in order to obtain the performance map of the compressor. In the following study, a single rotational speed curve was taken into account for the comparison with the computational results provided by the CFD analysis.

	Parameter	Value
Inlet	$p_{tot,in}$	103560 Pa
	$T_{tot,in}$	297.533 K
	α_r	0°
	α_θ	0°
	Turbulence intensity	1 m
	Eddy length scale	5 %
Outlet	$\dot{m}_{out}$	variable [kg/s]

Table 3.2: Boundary conditions used for the numerical simulations.

In order to couple the rotating and the stationary frame for the steady simulation, a mixing plane approach is used in the rotor-stator interfaces for both solvers. The stage/mixing-plane model is an alternative to the frozen rotor model for modeling a change in the frame of reference. Instead of assuming a fixed relative position of the components, the stage model neglects transient interaction effects between the components and performs a circumferential averaging of the fluxes over the interface, assuming a perfect flow mixing across the interface. The benefit of the mixing plane is that it drastically cuts down the calculation time, however, the usage of the mixing planes demonstrates a good agreement with experimental results [27]. The solid boundaries of the computational domain are modeled as a smooth wall. For the velocity, a non-slip condition is used, and for the energy equation, an adiabatic boundary condition is used.

Conversely, for the time-resolved computations of the flow (unsteady), a transient rotor-stator interface was adopted. The transient approach, also known as the Sliding Mesh method, takes into account transient interactions at the interface, and therefore the cells of each component slide along the interface to mimic the rotation of the impeller. On centrifugal compressors, this model predicts the true transient interaction of the flow between the impeller and diffuser. The interface location is updated every timestep, resulting in higher computational effort and quantitative post-processing of the data required than the stage/mixing-plane model.

	Specification	Setting
	TRACE	
Spatial scheme	Accuracy	1^{st} and 2^{nd} Order
	Gradient method	GreenGauss
	Limiter	0
Temporal scheme	Scheme	Euler Backward
	Accuracy	2^{nd} Order
	Solution method	Predictor corrector
	CFX	
Advection scheme	Accuracy	High resolution
Transition scheme	Accuracy	High resolution

Table 3.3: Solver settings used for the numerical simulations.

In order to ensure a stable simulation, the spatial scheme began with 1^{st} order accuracy as its initial setting. Once a satisfactory level of convergence was attained, the accuracy was manually elevated to 2^{nd} order. This step proved crucial during the simulation, as initiating directly with 2^{nd} order accuracy resulted in errors and hindered the iterative solving process from commencing.

3.4.1 Convergence criteria

The Courant number (or CFL number) is of fundamental importance for transient flows. For a one-dimensional grid, it is defined by:

$$Co = \frac{\text{Fluid distance}}{\text{Cell distance}} = \frac{u \cdot \Delta t}{\Delta x} \tag{3.24}$$

where u is the local fluid speed, Δt is the timestep and Δx is the mesh size. On commercial CFD codes, the implemented Courant number is a multidimensional generalization of equation 3.24 where the velocity and length scale are based on the mass flow into the control volume and the dimension of the control volume.

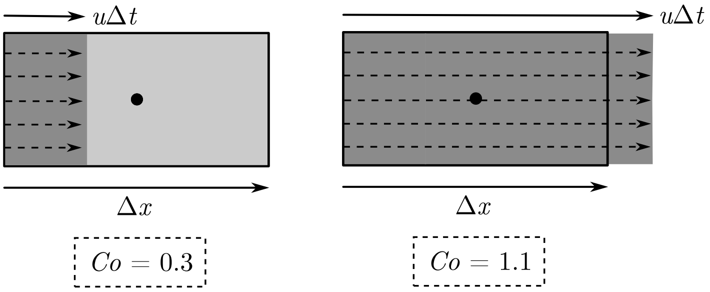

Figure 3.17: Courant number in a cell.

In explicit CFD methods, it is essential to select a timestep that ensures the Courant number is sufficiently small (Co $\sim$ 1) to maintain stability. Failing to do so would lead to instability, causing the numerical solution to diverge. On the other hand, implicit schemes, such as those available in Ansys CFX, do not necessitate a small Courant number for stability. Nevertheless, in certain transient calculations, it might be necessary to keep the Courant number small to precisely resolve transient details.

To ensure stability in the simulation, the CFL number is defined as a ramp, with a lower value at the beginning that increases as the simulation advances.

Timestep	CFL number
1	1
100	50

Table 3.4: CFL-Number settings.

In conclusion, the pre-processing stage of CFD simulations is a multifaceted endeavor that demands meticulous attention to the characteristics of the physical system under investigation. It is crucial to accurately and efficiently specify the geometry, mesh, boundary conditions, physical properties, and numerical schemes to achieve a precise simulation outcome.

Below, the residuals of the simulation are presented for the standard mesh of the single passage. The chosen operating point for that simulation is a mass flow of $\dot{m} = 2.075$ kg/s and a rotational speed of $n = 20202$ rpm.

In the TRACE solver, as a non-linear time domain solver, the residuals are given in three different norms. The reduction to a global scalar value starts from the residual vector which is one of the 5 governing equations for each cell in the domain. The residual is given by:

$$\begin{aligned}\text{Residual} = &\ \text{flux balances}\\ &- \text{volume integral of sources}\\ &+ \text{temporal terms (in case of unsteady simulations)}\end{aligned}$$

The cell volume is denoted by, the local pseudo-time step size by and the CFL number by.

L1 residual

$$\frac{1}{n_{\text{cells}}} \sum_{j}^{n_{\text{cells}}} \sum_{i}^{n_{\text{equations}}} \left| \frac{\Delta\tau_j}{V_j c} R_i^j \right| \tag{3.25}$$

L2 residual

$$\sqrt{\frac{1}{n_{\text{cells}}} \sum_{j}^{n_{\text{cells}}} \sum_{i}^{n_{\text{equations}}} \left(\frac{\Delta\tau_j}{V_j \cdot Co} R_i^j \right)^2} \tag{3.26}$$

Max residual

$$\max_j \sum_{i}^{n_{\text{equations}}} \left| \frac{\Delta\tau_j}{V_j \cdot Co} R_i^j \right| \tag{3.27}$$

Note that the cell volume is denoted by V_j, the local pseudo-time step size by $\Delta\tau_j$, and the CFL number by Co where the residuals are all based on non-dimensionalized Navier-Stokes equations.

Residuals

Below, the residuals of the simulation are presented for the standard mesh of the single-passage (full setup). The chosen design point for the simulation is a mass flow outlet boundary condition of $\dot{m} = 2.075$ kg/s and a rotational speed of the impeller of $n = 20202$ rpm. The shroud part of the impeller is counter-rotating and the impeller presents a blade-tip gap of 5 mm.

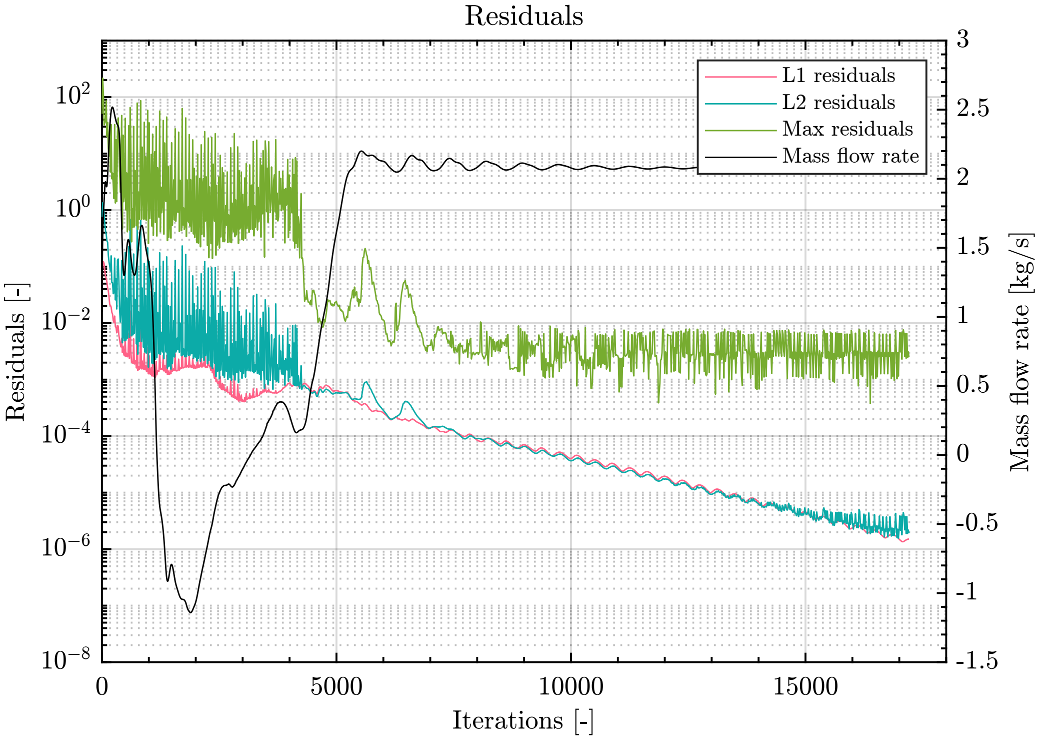

Figure 3.18: Convergence map of a simulation with TRACE.

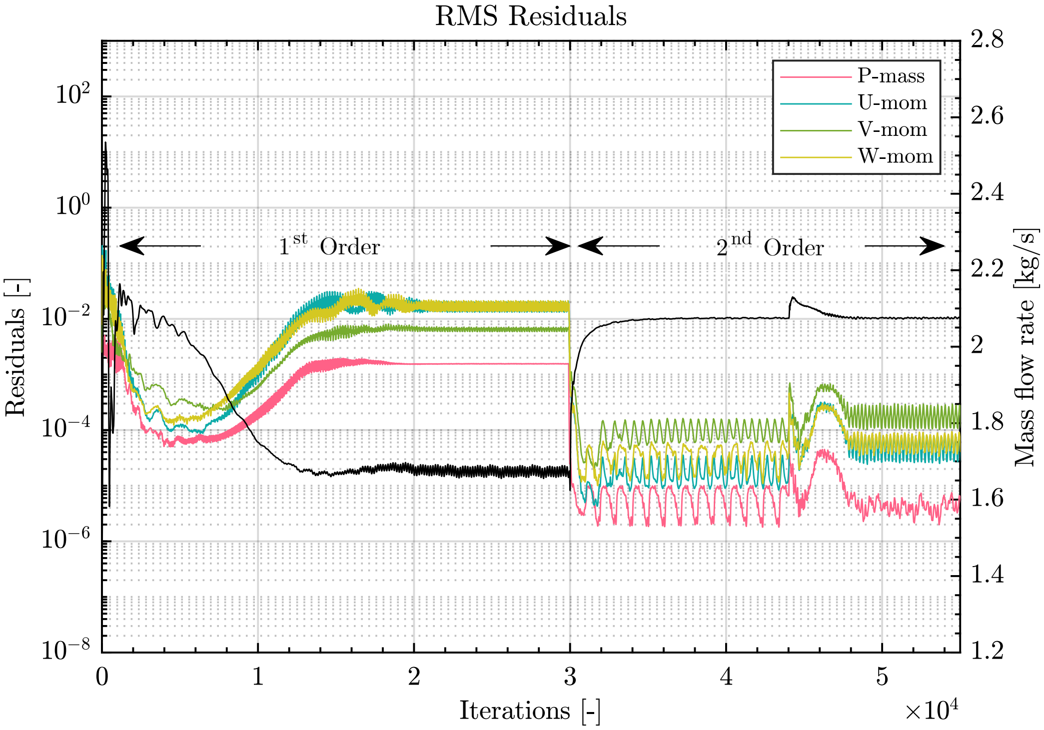

Figure 3.19: Convergence map of a simulation with CFX.

4

Results

4.1 Single passage (Impeller only)

simplerIn the first step, the numerical calculation was performed by both solvers (TRACE and CFX). Furthermore, TRACE solver was adopted only for the steady-state simulation of the preliminary analysis with simpler models while CFX was used to perform the transient simulations that will be shown in the following chapters.
The Figure 4.1 presents the impeller performance parameters predicted by the steady single-passage model.

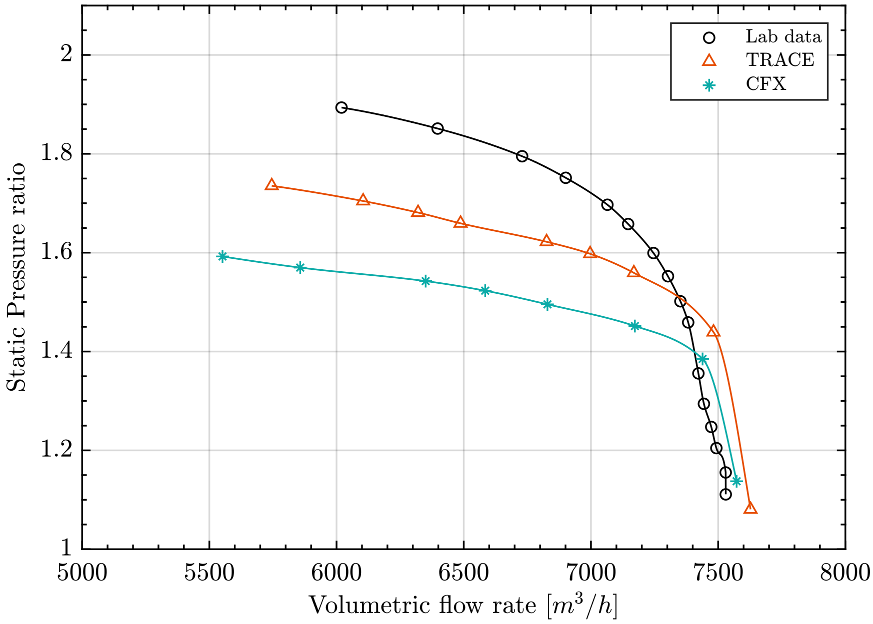

Figure 4.1: Performance map representing the static pressure ratio (Π_{ss}) and the inlet volumetric flow rate ($\dot{V}_{in}$).

As it is shown in Figure 4.1, the computed performance map well predicts the experimental curve in the close-to-choke region at higher flow rates. Subsequently, it's noticeable that both numerical curves reported a further drop in pressure when it moved up to the close-to-surge region. Additionally, it has to be said that the experimental curve of the static pressure ratio was obtained by measuring the inlet static pressure immediately after the IGV while the outlet static pressure was measured immediately after the exit diffuser tube of the volute casing. However, the numerical curves for both solvers were obtained by having an inlet static pressure in the impeller inlet and an outlet static pressure in the diffuser outlet. Therefore it's expected that the further gain in pressure is due to the presence of the volute casing.

Moreover, there is a pressure discrepancy between the results of the TRACE and CFX curves which may be due to the different numerical approaches that the two solvers implement to solve the analysis.

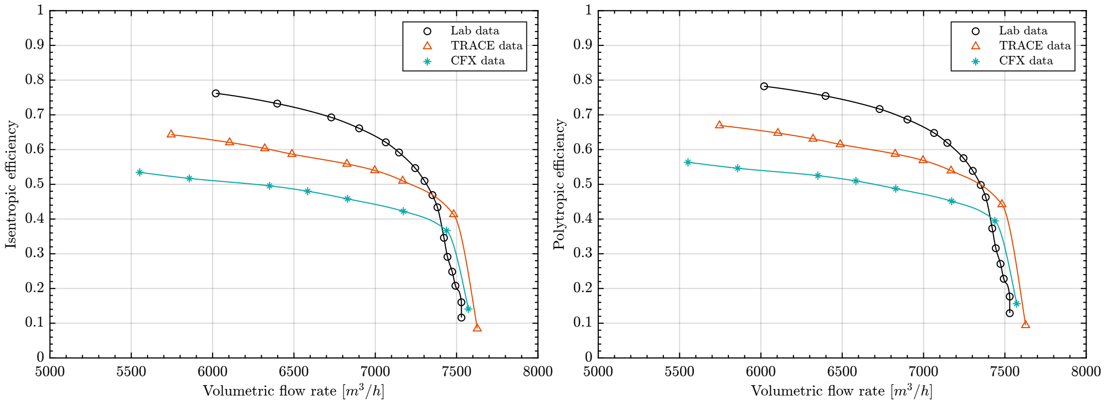

(a) **(b)**

Figure 4.2: Impeller performance predicted by the steady single-passage simulation; shown are: (a) isentropic efficiency η_{is} (b) polytropic efficiency η_p.

Due to the under-prediction of the static pressure ratio (Π_{ss}), the isentropic (η_{is}) and polytropic (η_p) efficiency is expected to be largely under-predicted as depicted in Figure 4.2. This is because the total pressure ratio is the scale for the compression capability whereas the output-input ratio η describes how efficiently a compressor can work. The under-prediction is particularly large at the near-surge locations.

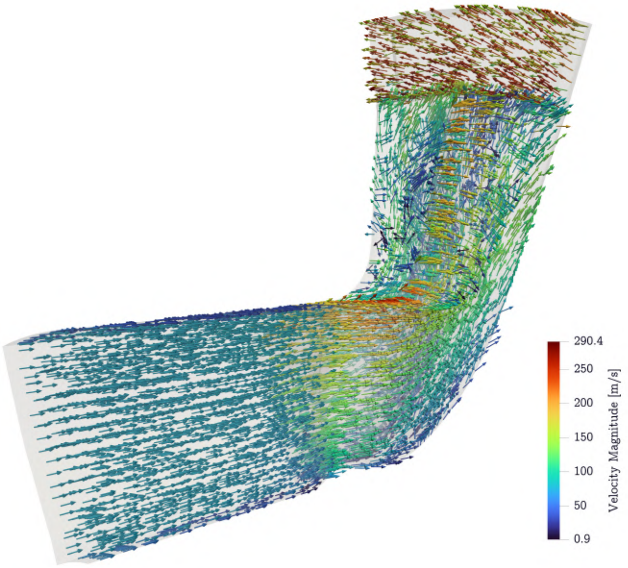

(a) Isometric view

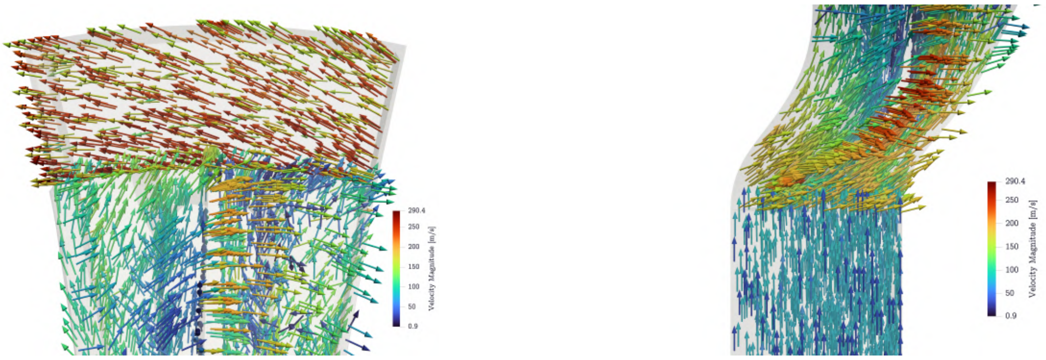

(b) Front view

(c) Top view

Figure 4.3: Velocity vector of the flow field for the steady, single-passage simulation.

The way the solver calculates the flow can be seen in the steep turn of the flow at both transition zones, from input to rotor and from rotor to exit. The flow calculations are carried out with respect to the related system when dealing with rotating domains or systems, such as the rotor in this instance. However, the absolute system is used, which includes the circumferential velocity in the computation of the total velocity and results in a sudden and abrupt shift in flow direction when the flow enters a non-moving domain, such as the outlet domain. Figure 4.4, which shows the flow streamlines, also illustrates this occurrence.

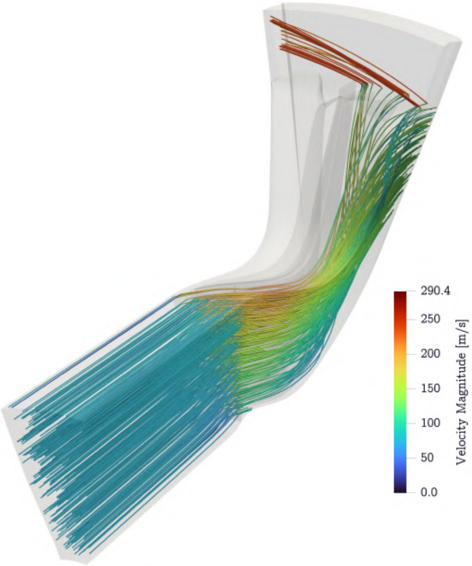

(a) Isometric view

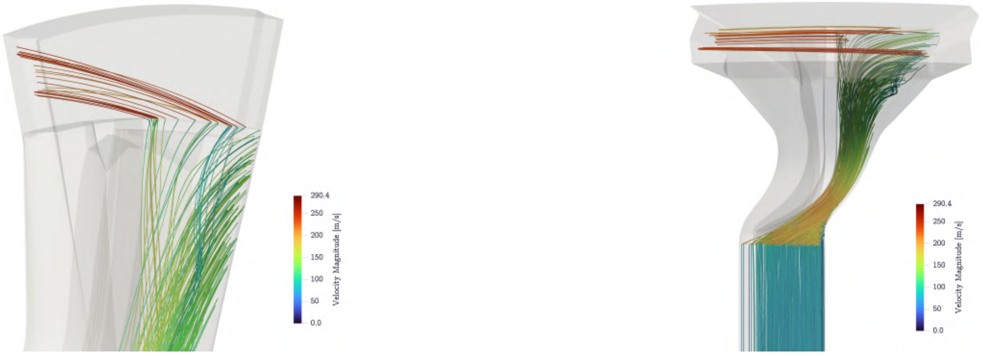

(b) Front view

(c) Top view

Figure 4.4: Streamline of the flow field for the steady, single-passage simulation.

In contrast to the velocity vectors given in the preceding pictures, the figures above reveal that there are some locations in the domain where the streamlines seem to be nonexistent. This is due to the fact that the streamlines shown in Figure 4.4 only include the flow coming from this one segment's inlet and ignore any flows coming from the surrounding segments' inlets. As a result, several areas of the segment seem to be empty. In truth, however, the flow from the adjacent segment enters and fills this vacant space, mimicking the pattern of the flow leaving this segment. Although there are no apparent reversible or circulating motions observable in the streamlines, there is evidence of particle mixing and intersecting flow channels.

4.2 Single passage (Full)

In this section the volute casing was implemented to the previous single-passage setup and a steady-state simulation was performed. From this point of the study, all the numerical simulations were conducted only by CFX solver since it has been found that it was able to guarantee greater accuracy in the results and greater robustness in computing analysis with flow instability. Thereafter, the computational domain consists of the single-passage impeller and the volute geometries include the vaneless diffuser, the non-axisymmetrical scroll part that goes around the diffuser, and the exit cone which leads the flow to the exit tube.

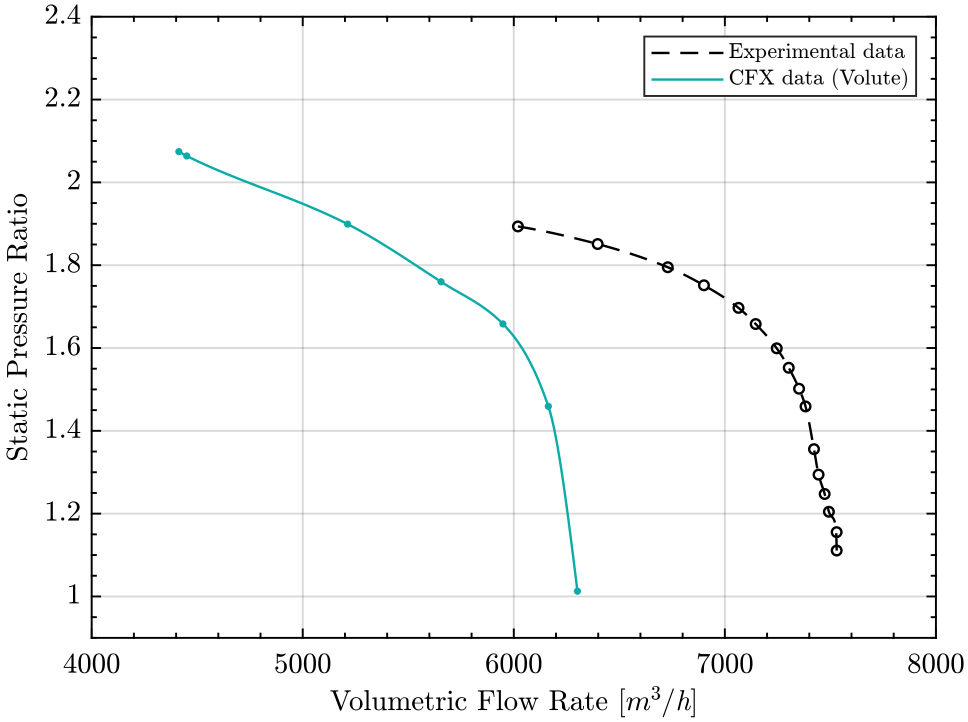

Figure 4.5: Performance map representing the static pressure ratio (Π_{ss}) and the inlet volumetric flow rate ($\dot{V}_{in}$).

As depicted in Figure 4.5, the performance curve shows how there is a pressure gain effect compared to the curve previously obtained with the single passage domain. According to the pressure measurement done in the lab, the static pressure ratio is referred to the outlet pressure in the exit-cone; it reaches a peak of $\Pi_{ss} = 2.07$.

Moreover, it is clearly visible how the performance curve obtained by CFX undergoes a significant shift towards lower flow rates. In the Figure 4.6 is represented the static pressure ratio calculated for three outlet pressures: impeller exit, volute exit, and tube exit. It's recognizable how the performance behavior of the impeller is heavily affected by the downstream components and there's a huge pressure gain between the diffuser and the volute exit. Additionally, the closer it moves towards the near-surge region the less divergent the tube-volute curves are. Generally, the exit tube should not contribute to a pressure gain since it's just a simple straight tube and thus there would have been expected a slight pressure loss in that region. However, a plausible reason could be explained by having a strong fluid recirculation in the exit cone of the volute that is then slowed down in the exit tube hence causing a pressure gain.

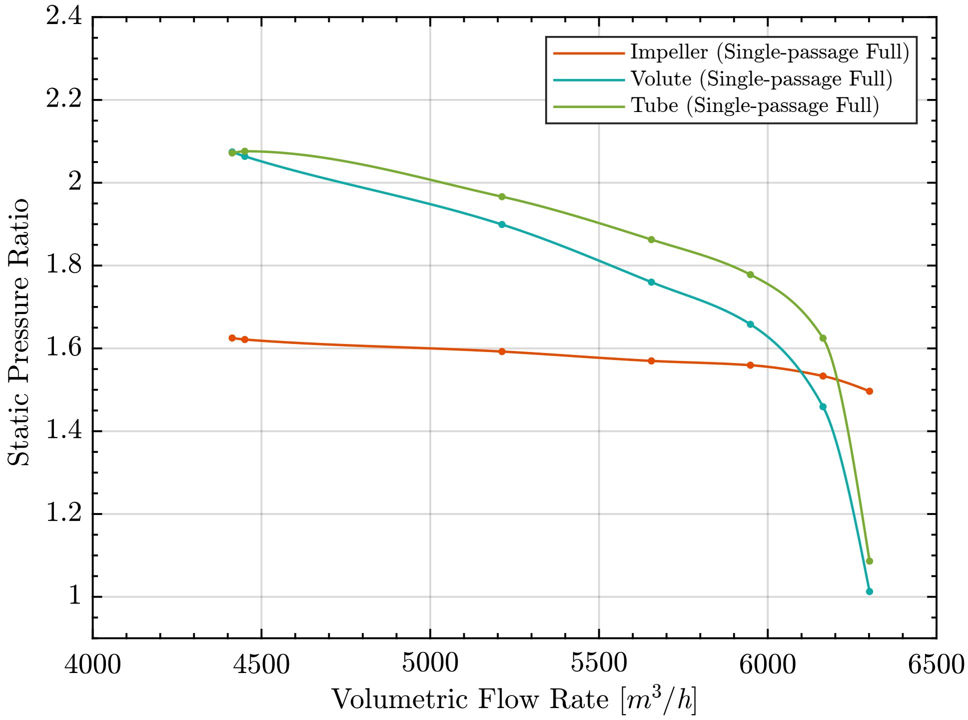

Figure 4.6: Performance map representing the static pressure ratio (Π_{ss}) measured in: impeller exit, volute exit, and tube exit.

Besides that, the implementation of the volute causes an anticipation of the choke condition and reduces the range of operation of the whole compressor. In fact, when the flow in the volute reaches the near-choke region, the impeller is still very far from that condition, and vice versa this trend also occurs at lower flow rates in the near-surge zone.

In Figure 4.7 is represented a comparison between the previous curves (Fig. 4.5) and the performance curve of the impeller obtained with the single-passage configuration seen in the previous chapter (Fig. 4.1)

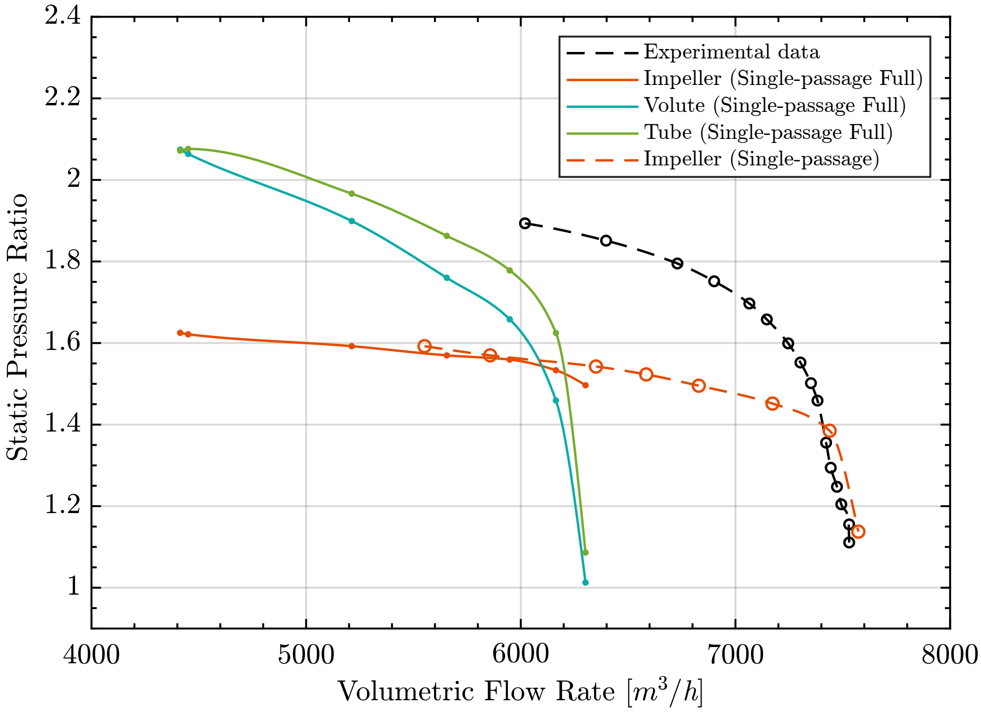

Figure 4.7: Performance map representing the static pressure ratio (Π_{ss}) measured in: impeller exit, volute exit, and tube exit.

It can be seen how the impeller's curve shape is not influenced by the volute itself, but the curve is simply shifted left to lower flow rates.
However, the shift amplitude is not coherent with that which occurs for the volute's curve, and therefore it finds in the circumstance in which the flow in the impeller is close to the surge condition, while in the meantime, the flow in the volute is still in the stable range.

It should also be said that the Demag® KG3.32 compressor examined for this study, and used as a reference for the comparison of the performance curves (experimental vs. CFD), is really aged. Therefore, uncertainties arise regarding the actual reproduction of the compressor itself due to a lack of information, such as technical drawings and performance values.
In particular, it's not possible to confirm whether the geometry of the volute and the shape of the tongue are equivalent to the actual ones of the reference compressor used for the laboratory tests. Furthermore, the tip clearance is relatively wide with respect to other commercial compressors.

The following Figure 4.8 shows the absolute static pressure and Mach number for three operating points, which represent the three possible flow conditions:

- $\dot{m} = 2.075$ kg/s $\longrightarrow$ $\dot{V} = 6164\ \mathrm{m}^3/\mathrm{h}$
- $\dot{m} = 1.75$ kg/s $\longrightarrow$ $\dot{V} = 5212\ \mathrm{m}^3/\mathrm{h}$
- $\dot{m} = 1.5$ kg/s $\longrightarrow$ $\dot{V} = 4450\ \mathrm{m}^3/\mathrm{h}$

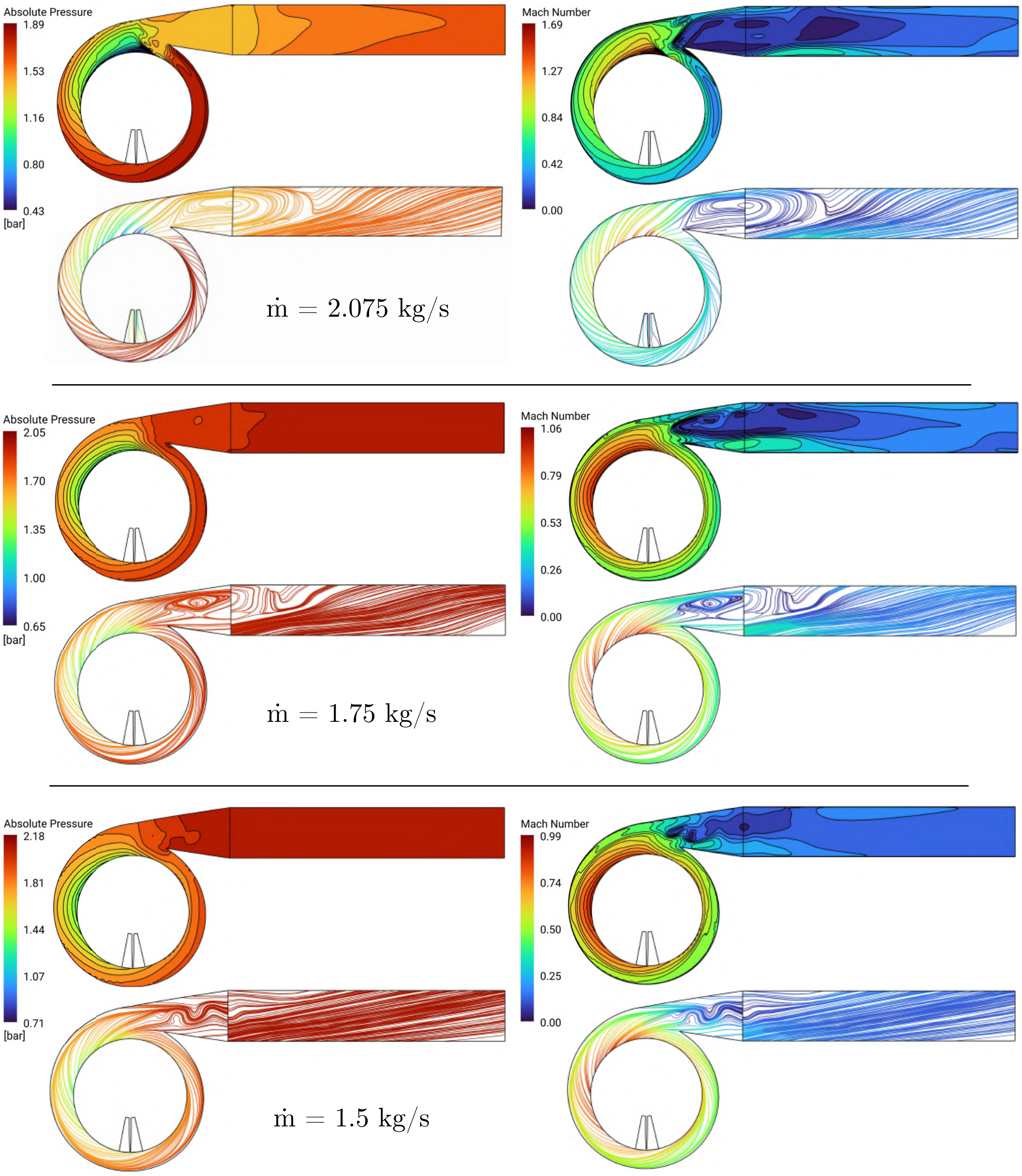

Figure 4.8: Contour maps and velocity streamlines representing the absolute static pressure and Mach number for three operating points: $\dot{m} = 2.075$ kg/s, $\dot{m} = 1.75$ kg/s, $\dot{m} = 1.5$ kg/s.

In all the cases it's evident how a strong flow recirculation is generated in the exit-cone of the volute. Furthermore, this recirculation is very wide for the case with a higher flow rate, i.e. near the choke condition, while it's mitigated when the flow rate is reduced.

This phenomenon, probably influenced by the flow deviation induced by the presence of the tongue, confirms the previous hypothesis concerning a considerable pressure gain in the outlet pipe (Fig. 4.6) precisely due to a deceleration of the flow.

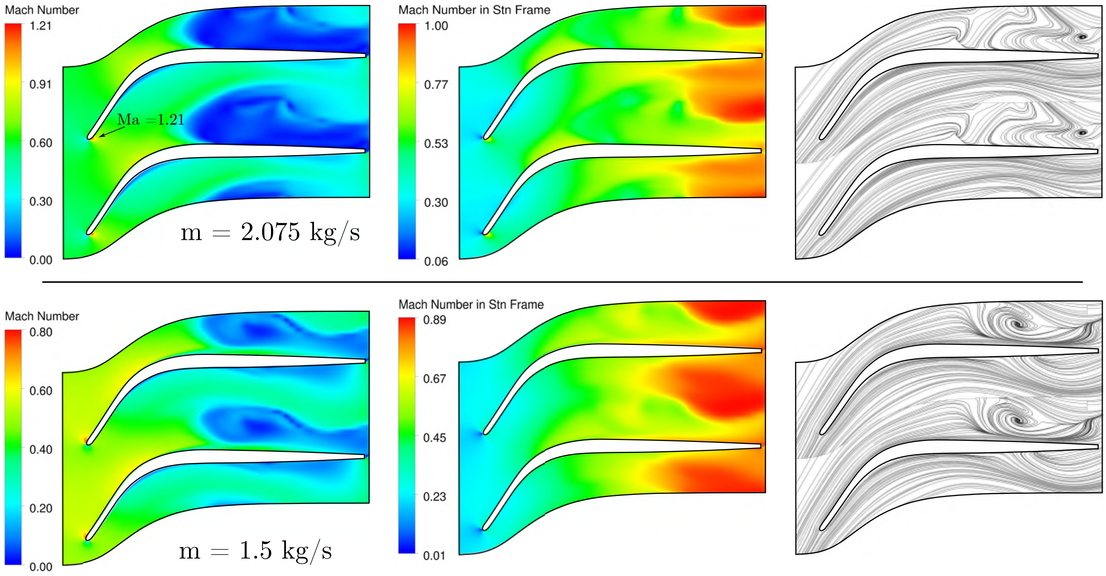

Figure 4.9: Color and stream maps of the impeller's blade-to-blade view at 80% of span distance representing Mach number and Mach number in the standard frame for two operating points: $\dot{m}$ = 2.075 kg/s and $\dot{m}$ = 1.5 kg/s.

In Figure 4.9 is represented the color and stream maps of the blade-to-blade view of the impeller at 80% of the span distance (close to the shroud side). It can be observed how the stagnation point in the leading edge moves from the pressure to the suction side as the mass flow increases. This is due to the increasing of the absolute component of the velocity, which leads to a very high negative flow incidence (i.e. low angles of attack). In particular, for the case with a higher flow rate, the low-pressure point is found close to the leading edge in the pressure side of the blade, where the Mach number is 1.21, and thus the flow regime is supersonic in that portion of the impeller throat. However, it's a consistent value given that it's in the negative slope section of the curve (Fig. 4.6) towards the choke point.

Besides that, with the same flow rate, the volute provides a supersonic Mach number of 1.69 in the proximity of the diffuser outlet, in the volute region close to the tongue and the exit-cone (Fig. 4.8). This strong acceleration of the fluid, which leads to a choke condition in the volute, causes intense instabilities in the flow field and huge pressure losses with a sudden efficiency degradation of the whole compressor.

Choking in the context of compressors is related to a phenomenon occurring during exceptionally high flow rates. This situation gives rise to potential blockage effects within the passages of the blade's rows. The blockage effect can be generated from various factors, including supersonic flow shocks, wake areas, strongly secondary flows, or even the inefficiency in utilizing the passage's full area due to disturbances in the flow. Often, a combination of these factors manifests in practical scenarios.

When a compressor's impeller is operated at its design point, the flow stream enters the impeller optimally. However, deviating from this ideal state, such as by reducing the flow rate, causes the inflow direction to change. This change in direction leads to increased losses, eventually culminating in separations within the flow along the suction side of the impeller blades, a phenomenon commonly termed as "stall". Conversely, raising the flow rate beyond the design point amplifies both losses and the inflow velocities directed into the impeller throat. Over time, the combination of flow separation and the occurrence of compression shock waves will essentially limit the flow that can pass through the impeller. Notably, these shock waves exhibit dynamic and fluctuating behavior.

The reality of this scenario is more complicated due to the three-dimensional nature of the flow field. As a result, compression shocks might obstruct only a portion of the flow path, typically closer to the shroud side, and separated flow may form rather complex flow structures [28].

Operating vaneless diffusers under choke conditions presents no notable difficulties. Specifically, there are no concerns regarding the occurrence of compression shocks or a heightened risk of flow separation that need to be taken into account. However, the situation is different for volutes. When volutes are operated at points other than their design parameters, they undergo a distinct alteration in the distribution of pressure along the circumferential direction [28]. This alteration becomes a critical factor when evaluating the radial forces acting on the rotor.

4.3 Full annulus

An improved simulation method is provided by full-annulus CFD simulations, which use the entire 360°non-uniform flow field as the inlet boundary conditions. As a result, the impact of flow non-uniformity can be measured by comparing the results from multiple passes to the change in impeller performance characteristics.

Considering the flow condition inside a volute passage, it's possible to find the critical geometric parameters. A sketch of the volute model used for theoretical analysis is given in figure 4.10. If the wall friction can be neglected, the angular momentum should be conserved, and therefore:

$$R \cdot V_t = R_d \cdot V_t' \longrightarrow V_t = \frac{R_d \cdot V_t'}{R} \tag{4.1}$$

where R is the radius, V_t is the tangential velocity, and the appendix donates the streamwise position of the diffuser outlet (or the volute inlet).

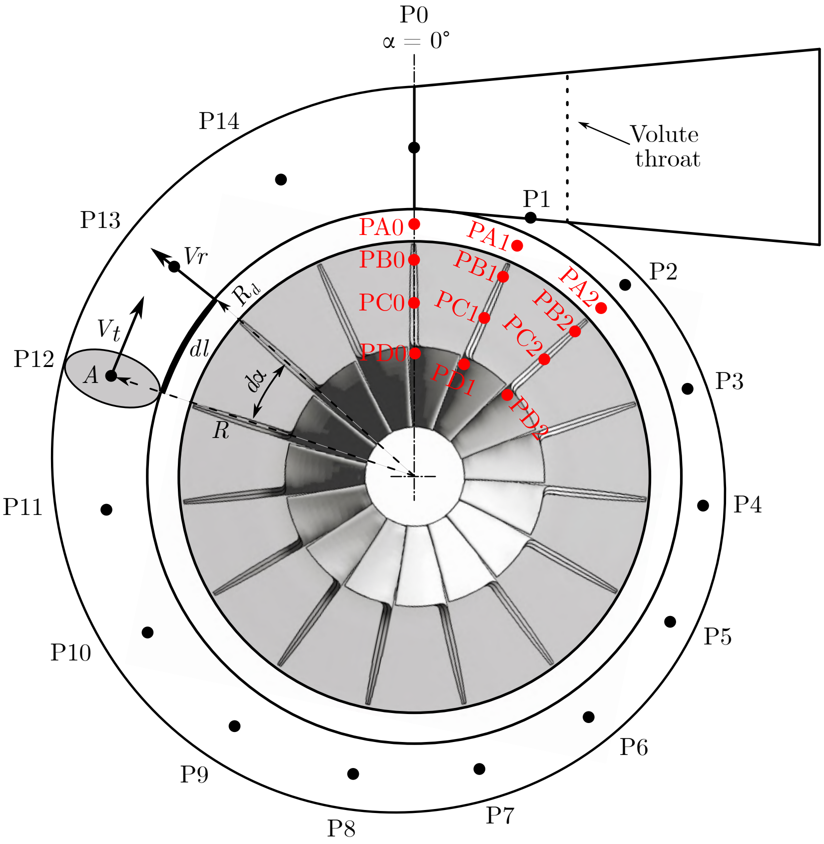

Figure 4.10: Monitoring points located in the volute and impeller domain.

Considering the circumferential position α, the mass flow rate passing through the cross-section A can be expressed as:

$$\dot{m} = \int \rho V_t dA_\alpha = \int \rho R_d V_t' \frac{dA_\alpha}{R} \tag{4.2}$$

From circumferential position α to $\alpha + d\alpha$, the increased mass flow rate passing through the cross-sectional area of the volute is:

$$d\dot{m} = d\left(\int \rho R_d V_t' \frac{dA_\alpha}{R}\right) = \rho' V_r' b dl \tag{4.3}$$

Within the range from α to $\alpha + d\alpha$, it is appropriate to regard V_t' as constant, since $d\alpha$ is small. Considering that $dl = R'du$, we have:

$$d\left(R' V_t' \cdot \int \rho \cdot \frac{dA_\alpha}{R}\right) = \rho' V_r' b' R' d\alpha \tag{4.4}$$

Therefore, the flow inside the volute is controlled by:

$$d\left(Vt' \cdot \int \rho \frac{dA_\alpha}{R}\right) = \rho' V_r' b' d\alpha \tag{4.5}$$

It is reasonable to assume that the density of the flow passing across section A is constant (denoted rm, where “m” denotes the average value). Then, equation 4.5 can be rewritten as:

$$\frac{d}{d\alpha}\left(V_t' \cdot \frac{A_\alpha}{R_m}\right) = V_r' b' \cdot \frac{\rho'}{\rho_m} \tag{4.6}$$

This equation expresses the relationship between the flow and the area-to-radius ratio A_α/R_m (cross-sectional area divided by average radius) distribution along the circumferential direction. Considering the ideal case, where the circumferential difference in the flow field can be neglected, a derivative of the equation 4.5 can be calculated as:

$$\frac{d}{d\alpha}(A_\alpha/R_m) = b' \cdot \frac{\rho'}{\rho_m} \cdot \frac{V_r'}{V_t'} = \text{constant} = k \tag{4.7}$$

According to equation 4.7, the A_α/R_m should change linearly along the circumferential direction; in this case, the area of the volute throat (Fig 4.10) is highly significant, since a larger throat area indicates a larger slope k of the circumferential distribution of A_α/R_m.

Because the slope k is related to the operating conditions of the compressor (i.e., related to ρ and V), the slope k determines the match point, i.e., the throat area determines the match between the volute and the upstream components.

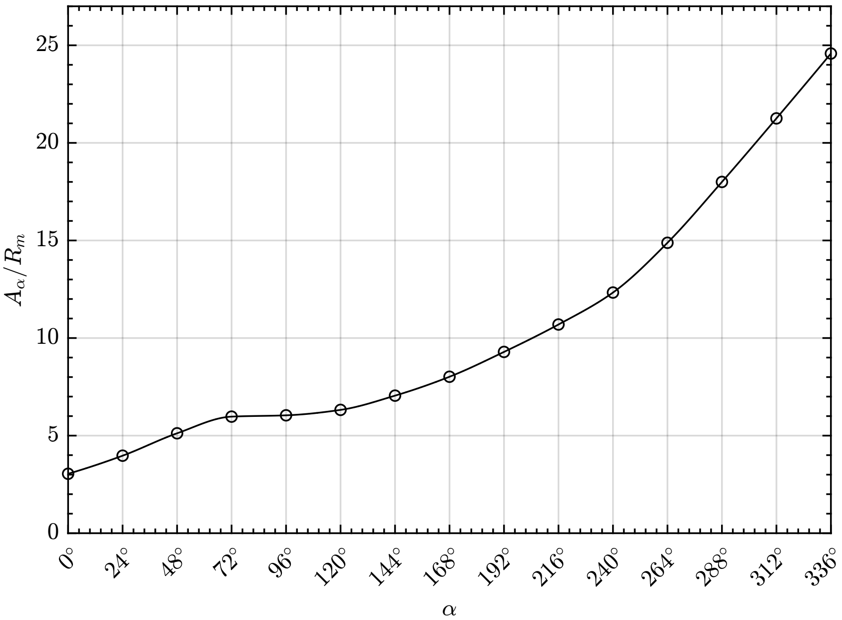

Figure 4.11: Volute with non-linear A_α/R_m distribution and fixed throat area.

If the influence of circumferential distortion cannot be neglected, the Equation 4.6 indicates that the circumferential distribution of A_α/R_m is no longer linear and is closely related to the flow field (Fig. 4.11). In this case, the detailed A_α/R_m distribution along the circumferential direction also has a significant impact on the volute flow condition. According to theoretical analysis, the throat area and the A_α/R_m distribution are two critical parameters affecting the volute performance.

In the Figure 4.12 is represented the performance map representing the comparison between the steady-state simulation of the single-passage (Full) and the full annulus 360°domains. In this case, only four operating points were examined because of the important computational effort and time required for each numerical simulation.

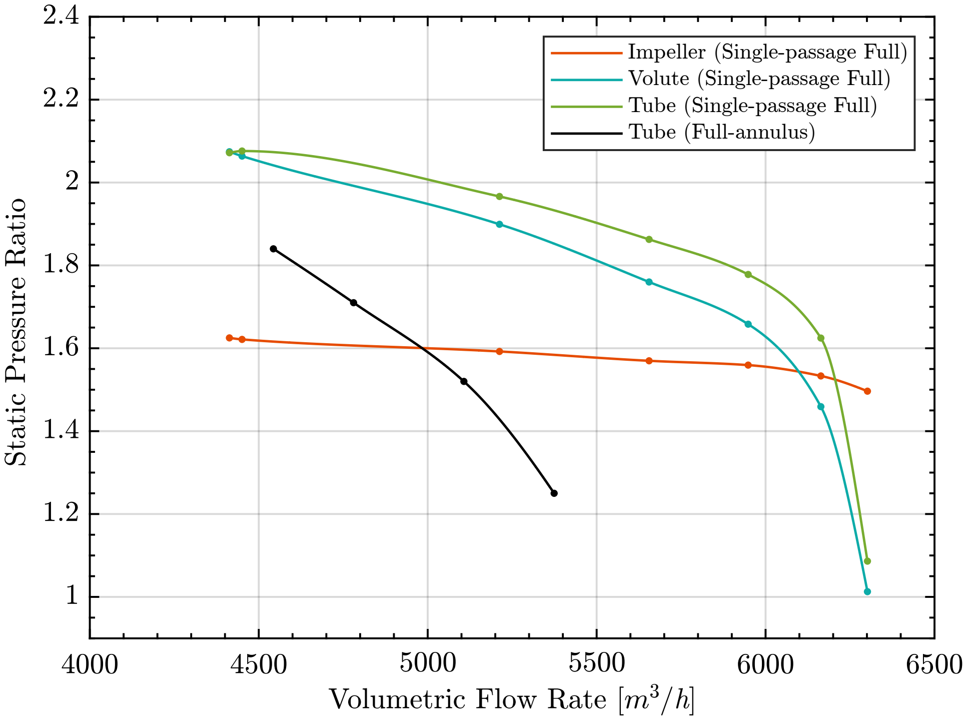

Figure 4.12: Performance map representing the comparison between the steady-state simulation of the single-passage (Full) and the full annulus 360°domains.

It's evident that there's a further shift of the whole performance curve towards lower flow rates, hence still reducing the range of operation of the compressor. It's reasonable to say that the presence of instabilities and supersonic flows between the rotor-stator interface is then aggravated in the full annulus configuration since the interface changed from a Mixing Plane (with periodic boundary conditions) to a Transient Rotor Stator. This leads to a further increase in losses and an overall drop in pressure ratio.

4.4 Transient simulation

In order to determine the transient pressure variations and the strength of pressure fluctuations in the model compressor, a transient simulation was computed for a single operating point, imposing an outlet boundary condition with an outlet static pressure $p_{out} = (p_{in} + 0.2)$ bar.

It should be mentioned that, for the transient simulations obtained by URANS equations, the pressure fluctuation components are only the phase-averaged values which are highly periodic on each grid node in the whole computational domain, and no instantaneous fluctuating pressure components are obtained. Therefore, the periodically unsteady pressure p at a grid node can be decomposed into two parts: the time-averaged pressure $\overline{p}$ and the periodic pressure $\tilde{p}$ representing the part of the pressure changing periodically with the blade passing frequency, defined as:

$$\overline{p}\left(node\right) = \frac{1}{N}\sum_{i=0}^{N-1} p\left(node, t_0 + i\Delta t\right) \tag{4.8}$$

$$\tilde{p}\left(node, t\right) = p\left(node, t\right) - \overline{p}\left(node\right) \tag{4.9}$$

4.4.1 Pressure fluctuation analysis of the volute

Time-dependent results of pressure distributions in the model compressor are analyzed in this section as the function of impeller relative position. Figure 4.13 shows the pressure distributions in the impeller, diffuser, and volute channels at middle height under $\dot{m} = 1.8$ kg/s, and the rotating angle ϑ was defined to show the impeller rotating positions.

Four pressure distribution results were shown from $\vartheta = 0°$ to $24°$ to indicate the pressure variations for a rotational step of one blade passage.

The results show that the pressure distribution in the impeller and diffuser channels is unsteady due to the impeller rotating positions. In particular, it shows a pressure maldistribution in the region close to the exit-cone and the tongue due to high recirculation by secondary flow within the blade passage section.

Furthermore, there's an evident pressure peak in the pressure side of the blade close to the trailing edge.

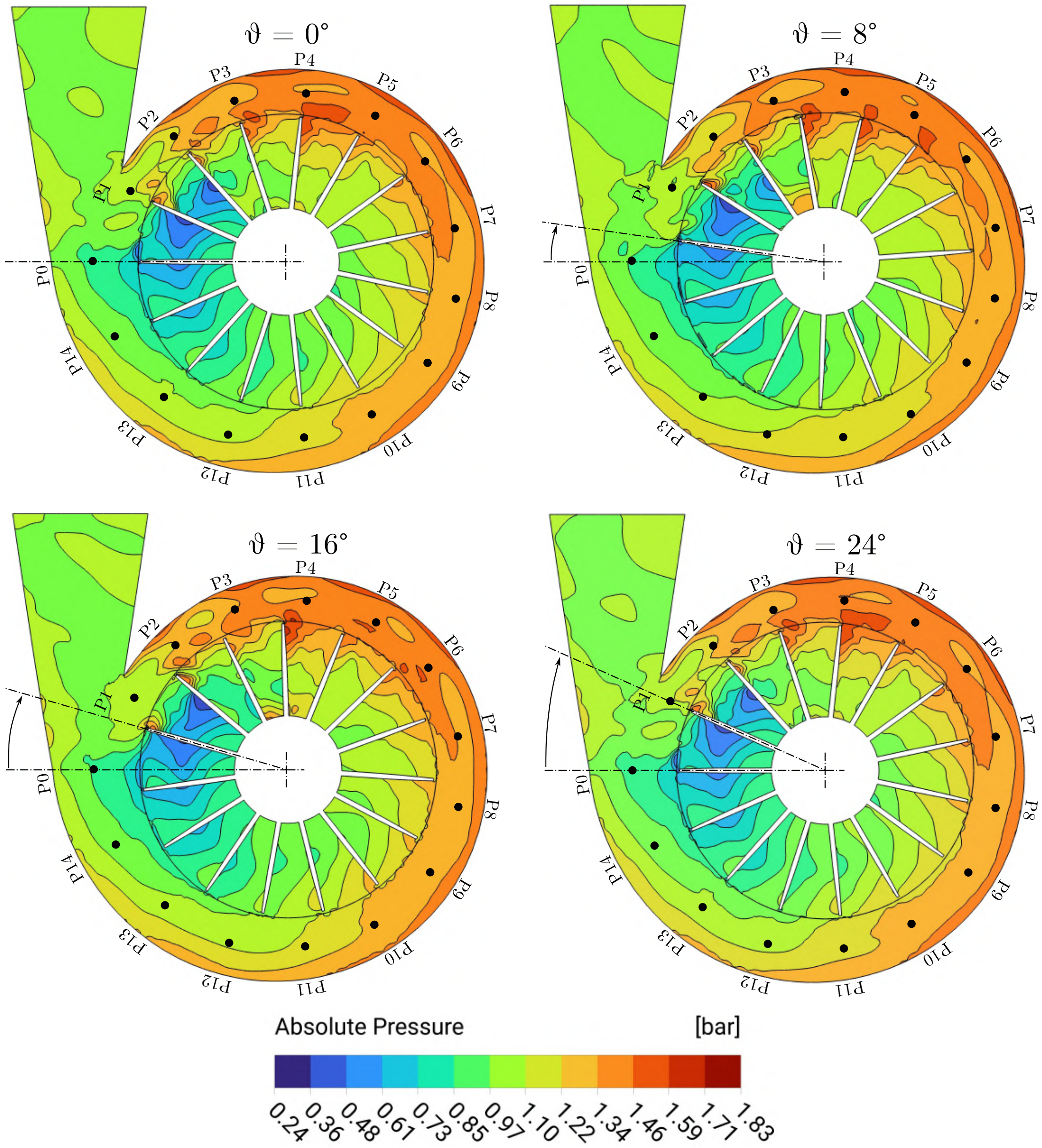

Figure 4.13: Unsteady pressure distributions in the impeller, diffuser, and volute channels at middle height for multi-impeller rotating positions under $\dot{m} = 1.8$ kg/s condition.

Moreover, it's even possible to observe large pressure fluctuations in the volute channel, that are influenced by the direct propagation of the fluctuations coming from the diffuser section.

Although the above obvious pressure variations can be analyzed for different time points, the variation extent cannot be easily indicated quantitatively by the contour map representation. Therefore, a new pressure fluctuation intensity analysis method will be used for this case, and the results will be discussed in the next section.

For analyzing the pressure fluctuation characteristics in the time and frequency domain, 14 monitoring points are defined in the volute as shown in Figure 4.10. All the monitoring points are placed in the origin of each cross-section of the volute and each point is equally spaced along the circumferential position of $\alpha = 360°/15 \text{ blades} = 24°$.

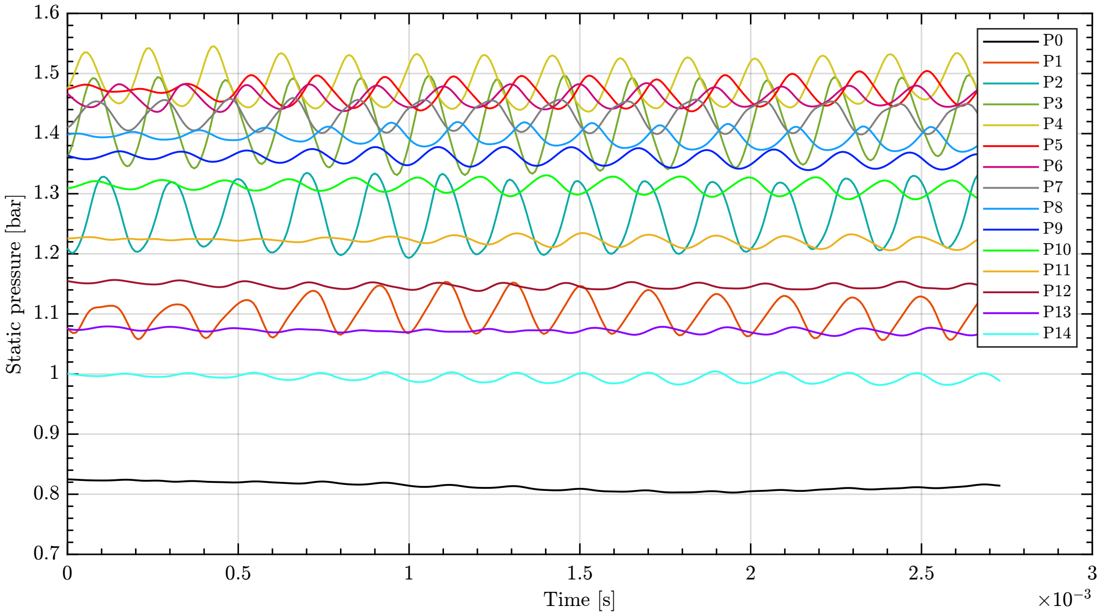

Figure 4.14: Time-history results of pressure fluctuations on the monitoring points under $\dot{m} = 1.8$ kg/s condition.

Figure 4.14 shows the time-history results of pressure fluctuations on the monitoring points under $\dot{m} = 1.8$ kg/s condition. The obvious periodicity of the fluctuation can be obtained, but the fluctuation extent is different because of the monitoring locations.

On point P1, which is near the tongue region of the volute, huge fluctuation, of which the peak-valley difference is more than 0.15 bar. On point P4, pressure fluctuation is smaller than on P3, and the peak-valley difference is about 0.09 bar, however, this point reported the maximum time-averaged static pressure of $\overline{p}_4 = 1.48$ bar.

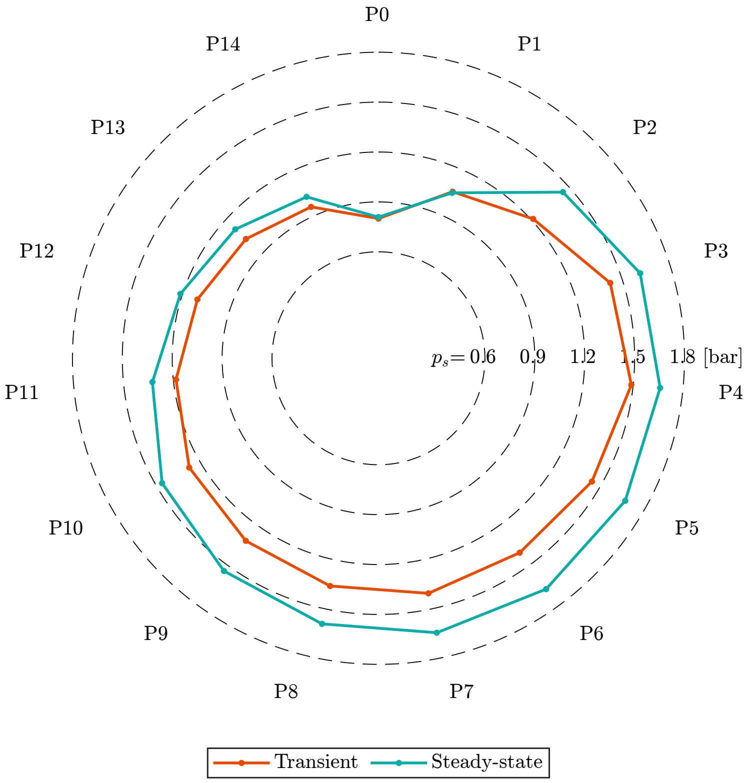

Figure 4.15: Circumferential average static pressure distribution in the volute domain and comparison between transient and steady-state numerical simulation.

Moving forward along the volute envelope, it can be noticed a progressive drop in pressure (Fig. 4.15), up to point P0. The apparent reason for the local pressure drop at that point is the rather sharp transition from the volute to the exit-cone. Moreover, as shown in Figure 4.14, at point P0 the pressure fluctuations are very attenuated and one could say that there is a quasi-stationary behavior in that region.

4.4.2 Frequency analysis

In order to analyze the pressure fluctuation more deeply, the results in the angle of frequency domain should be stated, and the fluctuations with different frequency components can be studied, and then the main contributing fluctuation components can be recognized.

Figure 4.14 shows the frequency domain results of pressure fluctuations on all the monitoring points, and the Fast Fourier Transform (FFT) method was used to transform the time domain results into frequency domain results, with a Hanning window function.

Because of the time step selected in this paper, the frequency domain below 60 kHz is valid due to the principle of the Shannon sampling theorem. The Nyquist–Shannon sampling theorem is a theorem in the field of signal processing that serves as a fundamental bridge between continuous-time signals and discrete-time signals. It establishes a sufficient condition for a sample rate that permits a discrete sequence of samples to capture all the information from a continuous-time signal of finite bandwidth. Therefore, the upper-frequency limit that is acceptable:

$$f_{signal} \leq \frac{f_{sampling}}{2} \quad \longrightarrow \quad f_{signal} \leq \frac{121.22\ [\text{kHz}]}{2} \simeq 60\ [\text{kHz}] \tag{4.10}$$

Furthermore, in the following figures, the upper-frequency limit will be restricted to lower values as they hold greater importance in this study. Moreover, to enhance frequency resolution and achieve an accurate analysis of pressure fluctuation composition, it was employed the sampling time from the last three calculated impeller revolutions.

The frequency domain graph of the pressure pulsation in the circumferential portion of the volute is shown in Fig.4.16:

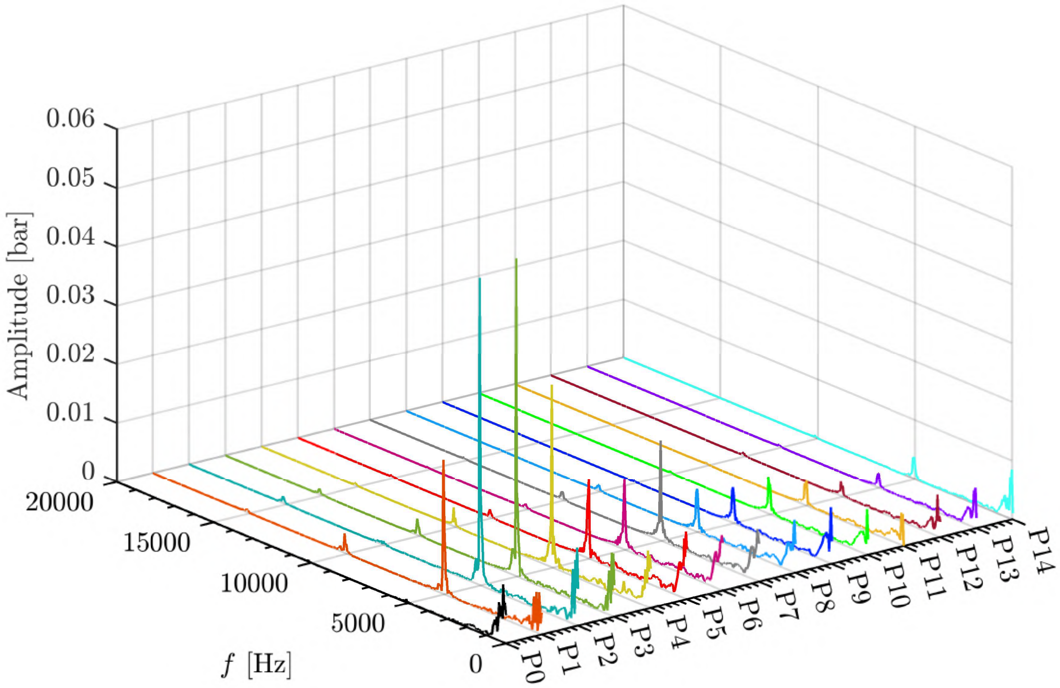

Figure 4.16: Frequency domain results of pressure fluctuation on the 14 monitoring points of the volute.

On all the monitoring point shown in Figure 4.16, obvious pressure fluctuation components can be observed on the impeller blade passing frequency (BPF) and its integer harmonics and on the impeller frequency (IF).

As a matter of fact, when the impeller rotates, the blades sweep over the monitoring points, and they alternate between the high-pressure and low-pressure zones. This is caused by the rotor-stator interaction.

Indeed, the two main frequencies are:

$$\text{IF} = \frac{rpm}{60} = \frac{20202}{60} = 336.7\ \text{Hz} \tag{4.11}$$

$$\text{BPF} = \text{IF} \cdot N_{blades} = 336.7 \cdot 15 = 5050.5\ \text{Hz} \tag{4.12}$$

Observing Figure 4.16 it's confirmed that the pressure fluctuations generated by the impeller's rotation after the rotor-stator interaction with the diffuser produces most of the pressure fluctuations propagating downstream. Additionally, the highest reported pressure amplitude was observed at monitoring point P3, which corresponds to the location with the most extensive pressure fluctuations.

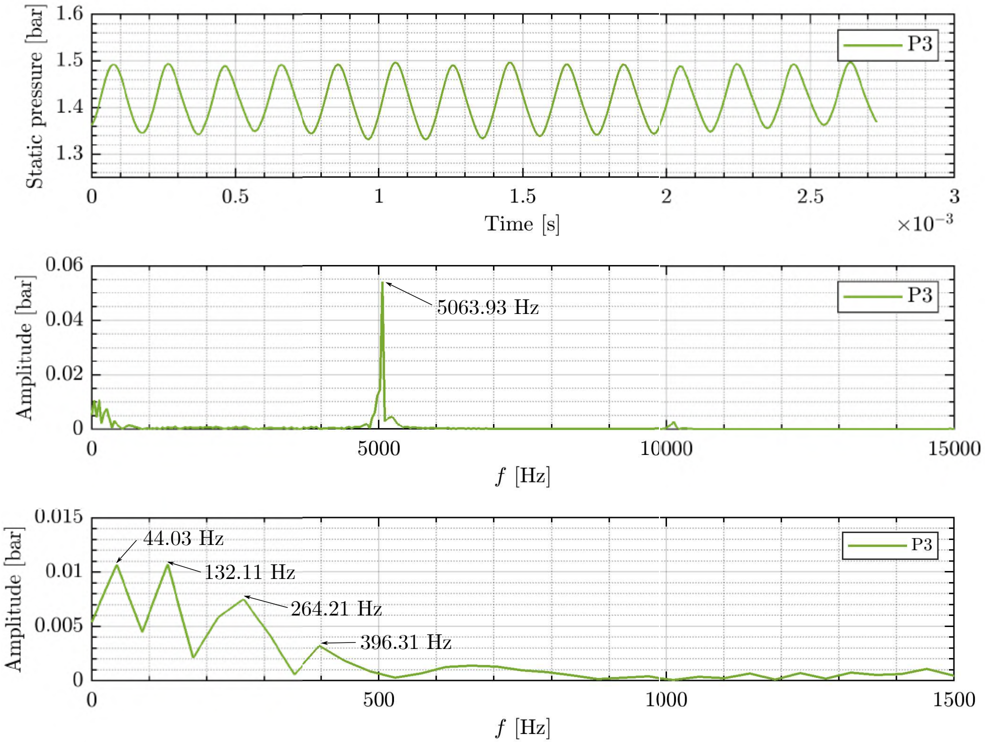

Figure 4.17: Frequency domain result of pressure fluctuation for the P3 monitor point.

In the detailed view of the pressure signal obtained for the monitoring point P3 (Fig.4.17) it can be identified the impeller frequency (IF) which is 15% greater than the theoretical one. Moreover, below the impeller frequency, it is possible to identify three other low-frequency peaks which are identified as small pressure fluctuations with broadband waves inside the volute scroll. One occurred at around 44 Hz ($\simeq$ 13.3% of IF) another one at around 132 Hz ($\simeq$ 40% of IF) and the last one at around 264 Hz ($\simeq$ 80% of IF). These large wave pressure fluctuations are protracted along the whole volute envelope and they are due to flow instability during the operation. They are probably due to a stall occurrence in the impeller-diffuser domain.

4.4.3 Frequency analysis in the impeller-diffuser

In the pressure distribution map seen in the previous section (Fig. 4.13), it has been found that the impeller domain shows a low-pressure maldistribution in the cutoff region close to the tube exit and the tongue.
Since the actual operating point is in the near-choke region, it's probable it undergoes a combination of flow separation and the occurrence of compression shock waves that will essentially limit the flow that can pass through the impeller. Furthermore, the shock waves themselves tend to be dynamic and fluctuating in nature, and therefore a frequency analysis in the impeller-diffuser region was conducted in order to investigate those pressure fluctuations.

The static pressure was analyzed at $\alpha = 0°$, 24°and 48°circumferential positions (P0, P1,P2 in Fig.4.10) at four equispaced meridian locations along the impeller-diffuser domain (A, B, C, D in Fig. 4.18).

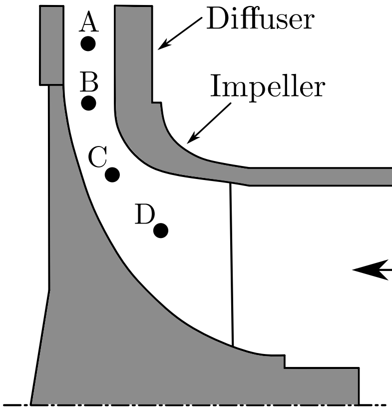

Figure 4.18: Monitoring points in the impeller-diffuser domain at middle-span height.

The Fast Fourier Transformation (FFT) spatial distribution results at each measurement point in the spanwise direction are shown in the following figures.

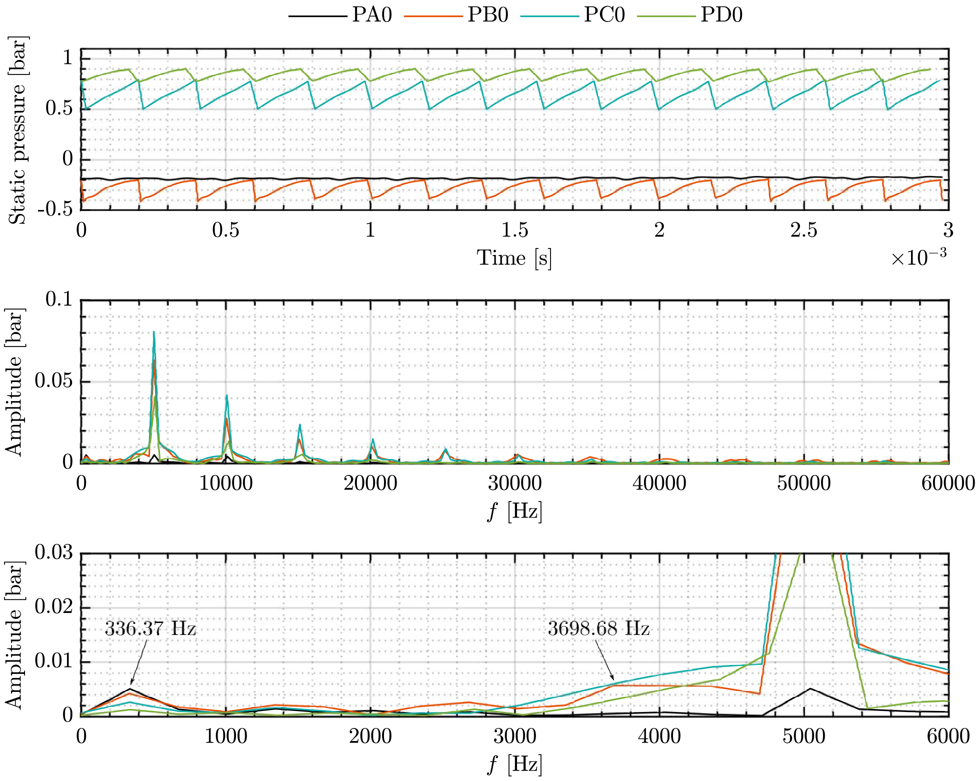

Figure 4.19: Time and frequency domain results of pressure fluctuations in the impeller-diffuser for the P0 monitor point.

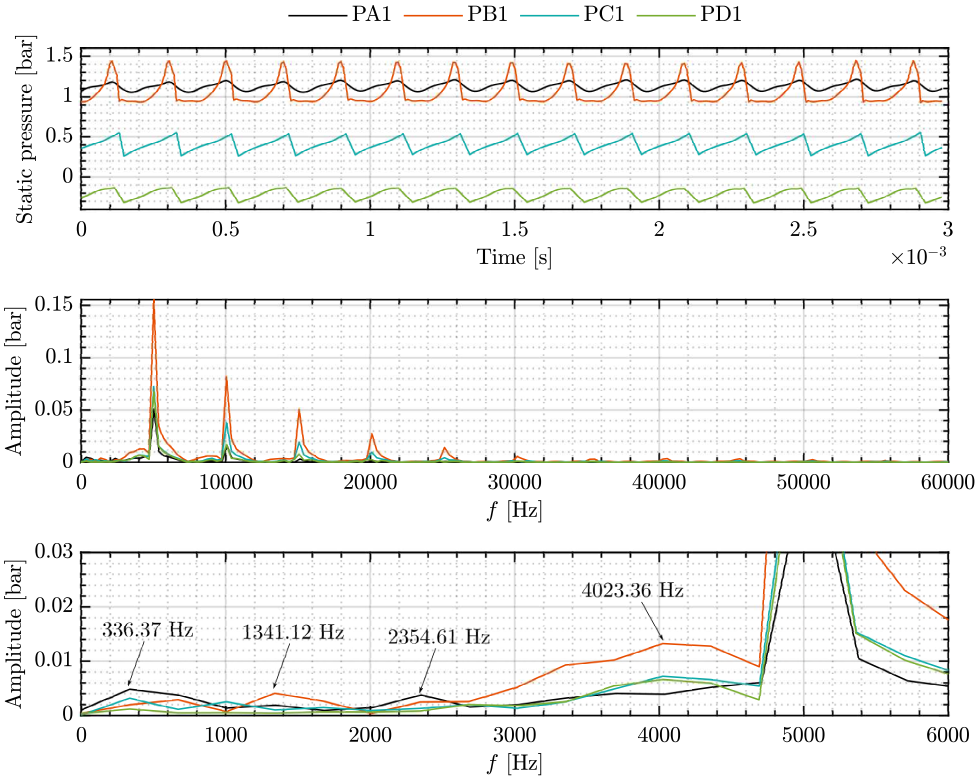

Figure 4.20: Time and frequency domain results of pressure fluctuations in the impeller-diffuser for the P1 monitor point.

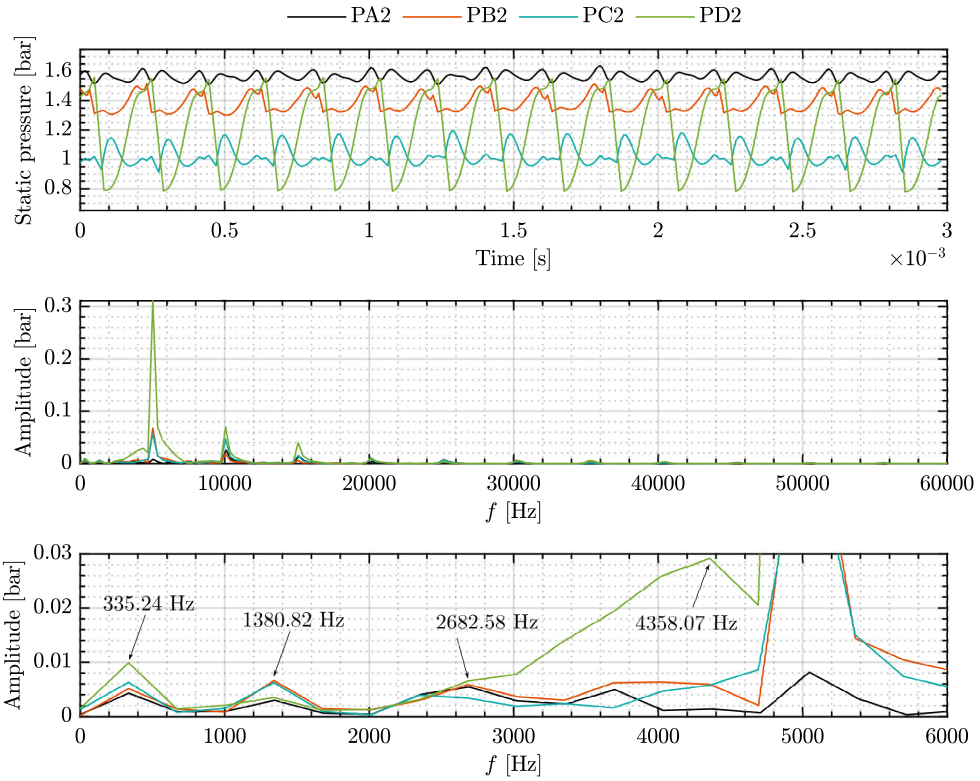

Figure 4.21: Time and frequency domain results of pressure fluctuations in the impeller-diffuser for the P2 monitor point.

It can be seen from Figure 4.20 - 4.21 that the pressure fluctuations in the cutoff region (close to the tongue) found frequencies different from those previously seen in the volute (Fig. 4.17). Of considerable interest are three relatively low amplitude peaks located at around 1340-1380 Hz ($\simeq 4 \cdot$ IF), then around 2355-2680 Hz ($\simeq$ 7-8 $\cdot$ IF) and the one with the larger amplitude at around 4020-4360 ($\simeq$ 12-13 $\cdot$ IF).

A current research project explores the feasibility of identifying various failures using non-intrusive measurement devices, where the physical Demag® KG3.32 compressor is operated to identify the influence of different parameters on the measurement signal. The IGV was modified by misaligning one or two blades respectively in order to simulate a fault. Subsequently, an accelerometer was placed on the inlet section close to the IGV. Indeed, Figure 4.22 illustrates the frequency domain of the measured data of the accelerometer, without any IGV misalignment. It can be seen in the detailed view (Fig. 4.22b) that there are excited frequencies around 4IF value which correspond to those found in the transient simulation seen before. Apart from that, it was not possible to assign a physical phenomenon yet.

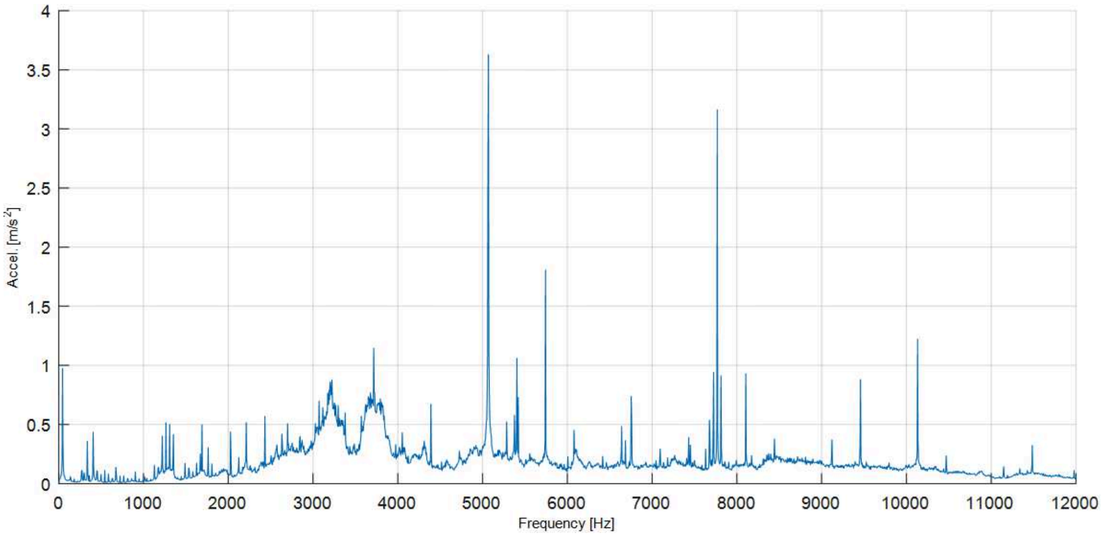

(a) Full spectrum domain.

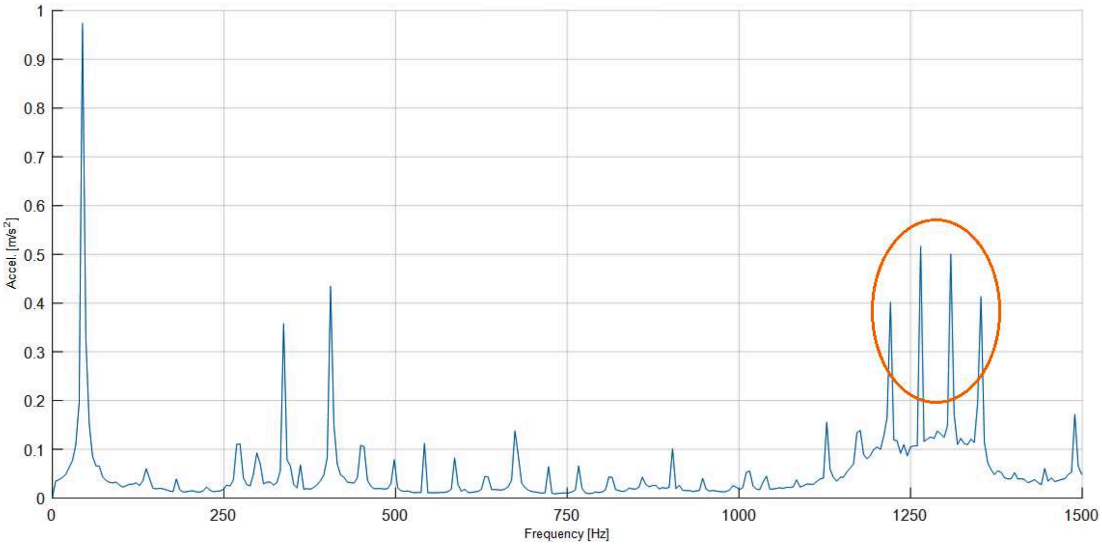

(b) Detailed view of the spectrum domain.

Figure 4.22: Frequency domain analysis of the accelerometer's recorded data.

It can be assumed that, since the results obtained from the transient simulation show that 4IF is excited by pressure fluctuations this may be the effect reported in the experimental result in Figure 4.22b.

The changed flow may produce a different pressure field which leads to different excited frequencies in the range of frequencies around 1340-1380 Hz ($\simeq 4 \cdot \mathrm{IF}$). This result certainly involves more information on the nature of this frequency peak which could indeed be aerodynamically correlated and not of a mechanical origin.

4.4.4 Flow structure analysis

From the results obtained up to this point, it's possible to state with certainty that the behavior of the impeller is strongly influenced by the presence of the volute, which has consequently led to the generation of a zone of strong instability and consequently large pressure fluctuations in the cutoff region, close to the tongue. In particular, it was observed that the impeller presents a quasi-steady stall behavior in about three cells while one cell reported an alternating stall in the proximity of P2 (Fig. 4.13).
Due to the influence of asymmetric outlet structures, the static pressure circumferential distribution is non-uniform in the impeller [29, 30].

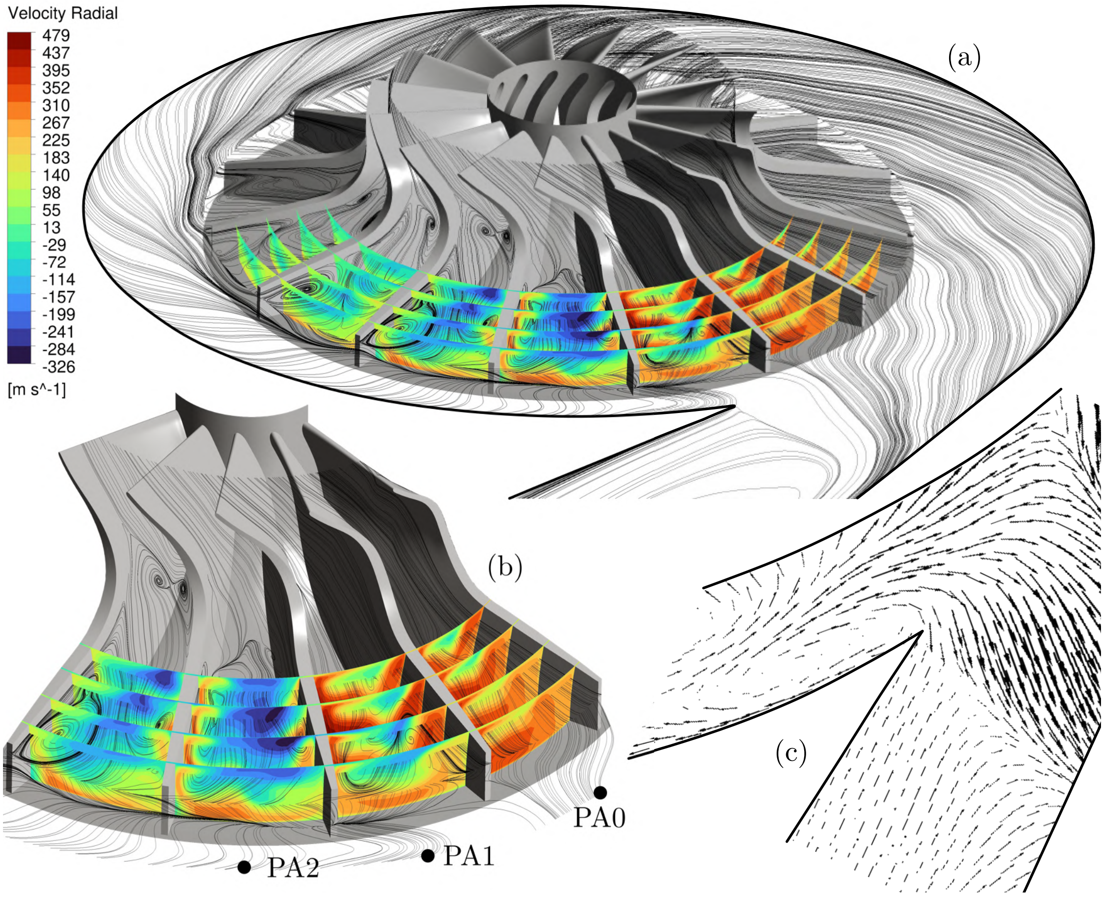

Figure 4.23: Representation of: (a) radial velocity distribution in the impeller/diffuser domain with streamline at 80% of span height (b) detailed view with diffuser monitoring points (c) velocity vectors in the cutoff (tongue region).

In Figure 4.23b the velocity streamlines in the meridian plane at 80% of span height show the flow behavior in the stalled cells. In particular, it shows three stalled regions: in the suction and pressure side of the blade close to the trailing edge and a region in the pressure side close to the leading edge.

Moreover, it can be seen from the velocity vectors in Fig. 4.23c how the velocity field in the cutoff region is non-uniform. A strong recirculation occurs in the proximity of the tongue whereas some flow moves backward in order to overcome the tongue and be expelled by the exit-cone. This leads to a strong non-uniform circumferential pressure distribution both in the volute (Fig. 4.24) and in the impeller.

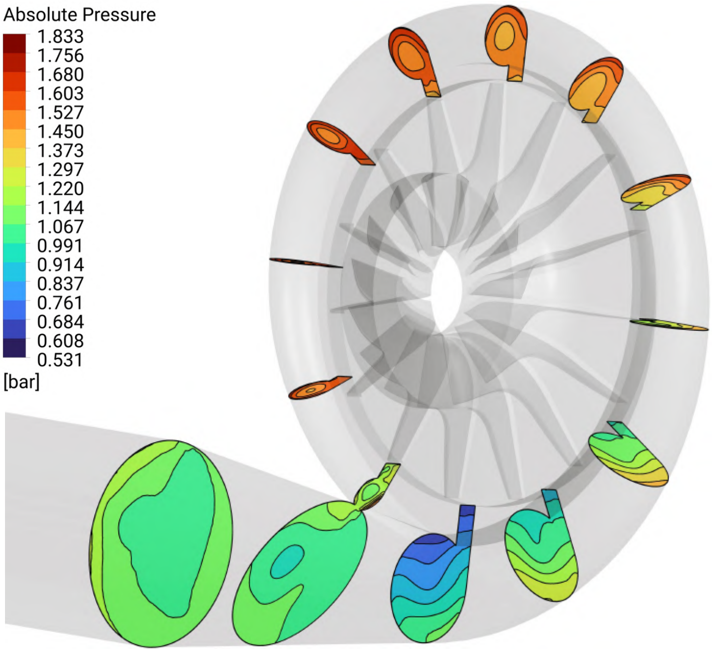

Figure 4.24: Static pressure distribution along the scroll envelope of the volute.

As mentioned before (Fig. 4.12) the compressor is working in overload conditions, and thus the volute is too small at high flow rates and the fluid is accelerating, leading to a circumferential pressure decrease and a sudden pressure increase near the tongue [31] as it's shown in Fig. 4.15. This pressure distribution also results in a distortion of the velocity field in the impeller.

Indeed some studied results showed that the asymmetric structures of the compressor, like the volute, will influence the circumferential position of stall inception onset. Galloway et al.[32] experimentally and numerically investigated the stability enhancement of a centrifugal compressor stage using a porous throat diffuser. In this work, the circumferential position of stall inception onset had been identified, which is related to the volute tongue because the non-axisymmetric effects propagate upstream through the diffuser passage and cause large pressure and incidence variations around the circumference at the diffuser inlet region. These studies showed that the circumferential position of stall inception onset is linked with the asymmetric structures of the compressor.

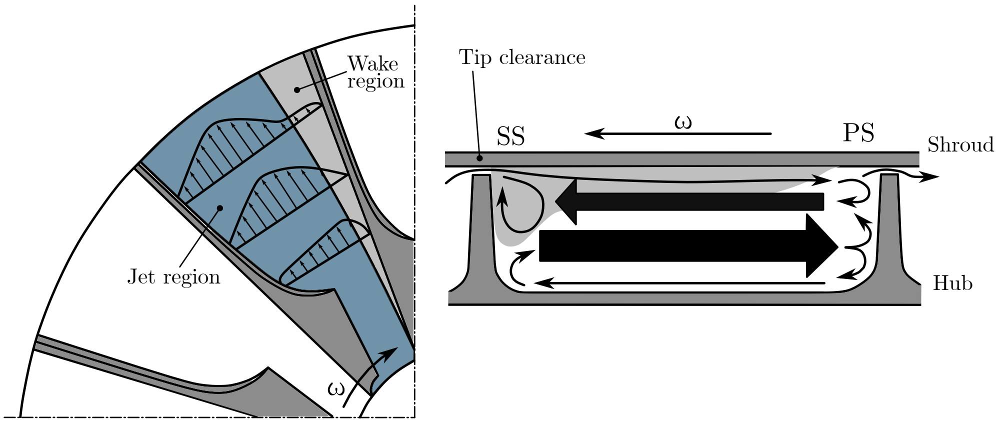

Figure 4.25: Secondary flows in the impeller blade passage.

In Figure 4.26 is represented the radial velocity distribution in a circumferential plane at different radius of the impeller and diffuser. It can be seen that the radial velocity is quite uniform for half of the impeller, and a well built non-uniformity in the cutoff region. Furthermore, there's a strong acceleration of the flow in the middle-low region (close to the hub) and a negative velocity close to the shroud.

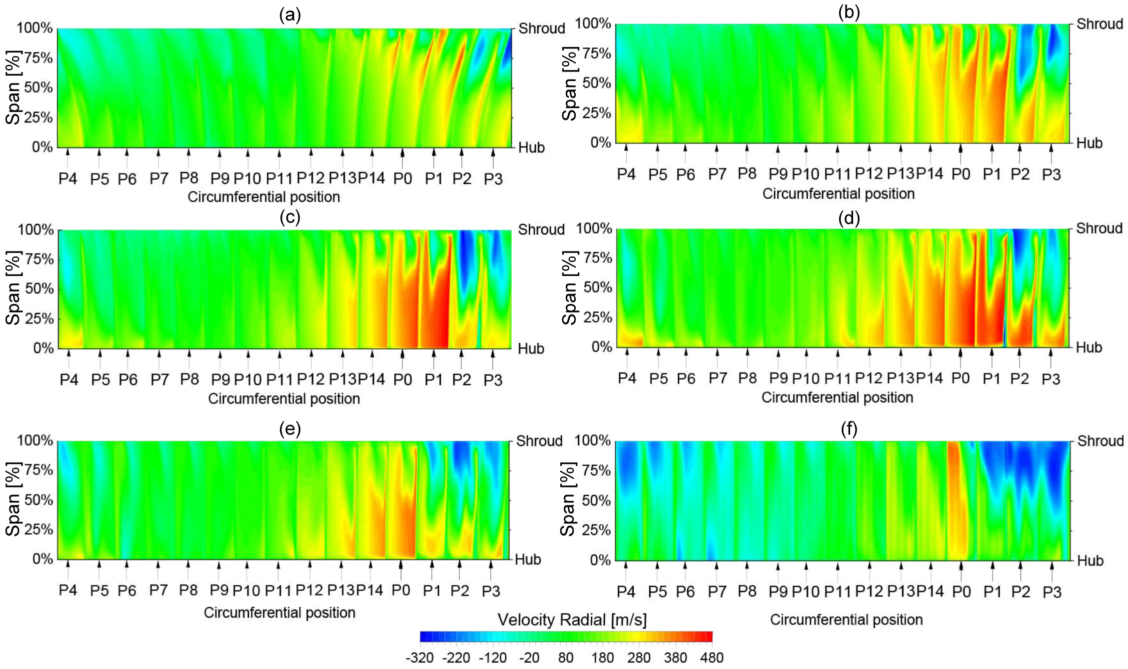

Figure 4.26: Radial velocity distribution in the impeller/diffuser domain for: (a) 60% chord length (b) 70% chord length (c) 80% chord length (d) 90% chord length (e) 100% chord length (f) diffuser mid-high.

At surface 4.26a, the radial velocity is still influenced by blade loading (with a faster relative flow at suction side) and by different curvatures of the walls (which are the cause for the hub to shroud gradient). Then the radial velocity distribution is progressively distorted downstream by the increasing thickness of the shroud boundary layer that can be seen at surface (c). The growth of this low momentum region corresponds to the increase of the high turbulence zone at the casing. A better knowledge of the complex phenomena inside the rotor can be achieved through the analysis of the vorticity contours of Figure 4.27.

Vorticity is the tendency for elements of the fluid to "spin" and it can be related to the amount of circulation or rotation (or more strictly, the local angular rate of rotation) in a fluid.

$$\vec{\omega} = \vec{\nabla} \times \vec{V} = \left(\frac{\partial}{\partial x} \, \frac{\partial}{\partial y} \, \frac{\partial}{\partial z} \right) \times (v_x \, v_y \, v_z) \tag{4.13}$$

The different contributions to secondary flows can be seen clearly in the surface 4.27a where two blade surface vortices along the blade height at suction (SS) and pressure (PS) side and a strong vortex near the shroud. This last vortex results from the merging of the passage vortex at shroud and the Coriolis vortex, as discussed by Van den Braembussche [33].
The blade vortex is stronger at the SS, due to the greater velocity gradient of the boundary layer, and tends to vanish towards the radial exit, as shown in Figure 4.27.

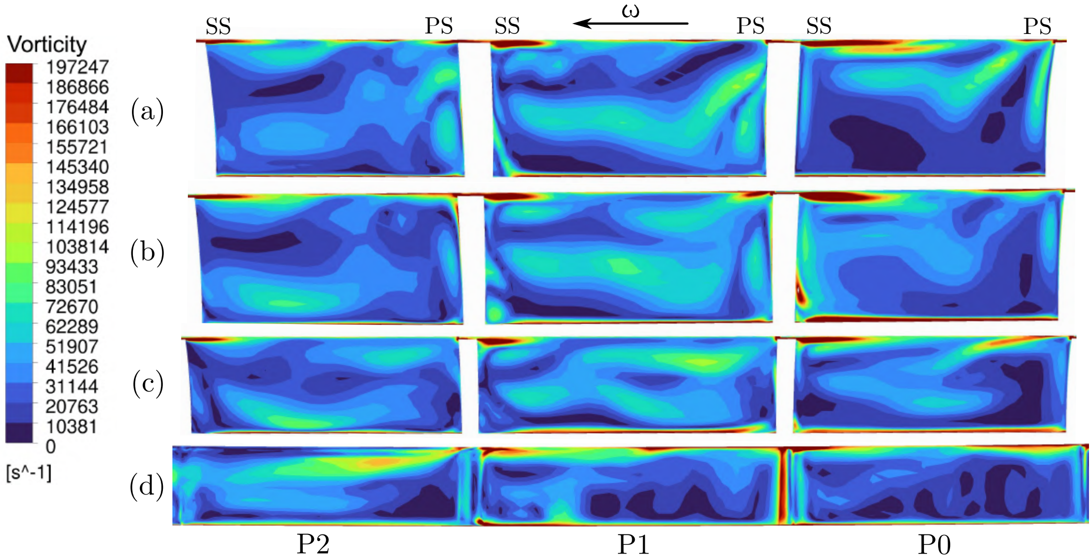

Figure 4.27: Vorticity in four hub-to-shroud surfaces of the impeller at point P0,P1 and P2 for: (a) 60% chord length (b) 80% chord length (c) 100% chord length (d) diffuser mid-high.

Due to the meridional curvature, the high-momentum fluid is convected towards the hub. On the contrary, the low-momentum fluid, coming mainly from the tip-clearance, is accumulated in the near-shroud region. Due to the difference in relative velocity, the Coriolis force drives the high-momentum fluid (also known as "jet") towards the PS, whereas the low-momentum fluid (also known as "wake") is driven towards the SS. The Coriolis vortex (CV) and the passage vortex (PV) have the same effect and are not always distinguishable one from the other: they are often referred to as passage vortices.
The tip-clearance flow is accumulated in the tip vortex that is well-defined in the first part of the impeller (Fig.4.27a) and is then transported along the shroud. Contrary to the core flow, the secondary velocity within the low-momentum boundary layer is determined by the pressure field dictated by the core flow. This results in a secondary flow from the PS to the SS within the hub boundary layer.

The overall result is a thick high-turbulence region in the upper half of the channel (shown in Figure 4.28d). The remaining portion of the section has a low turbulence level with high flow velocity and identifies the jet zone in the jet-wake model.

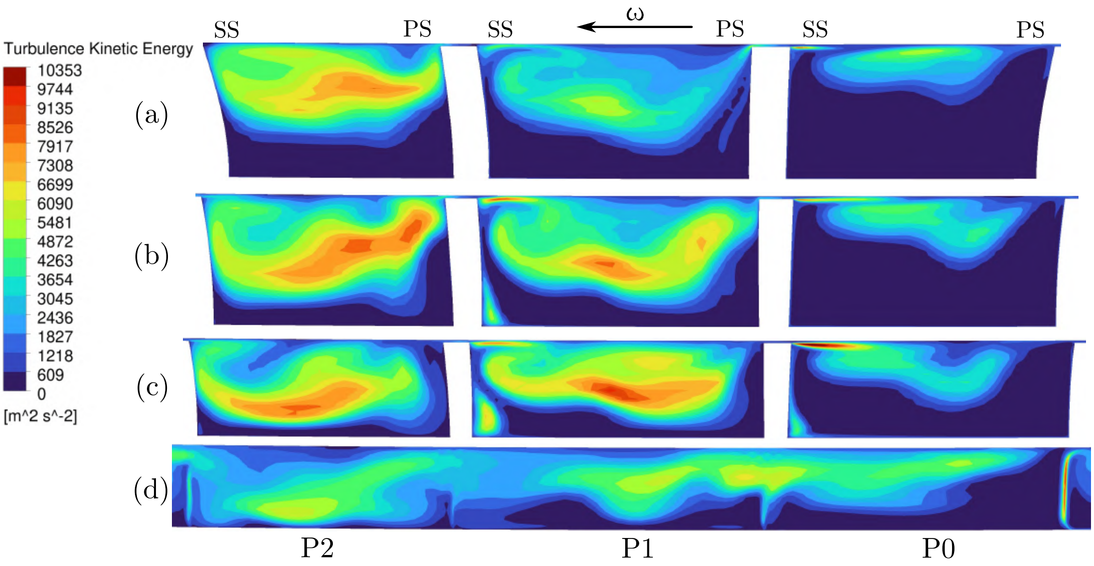

Figure 4.28: Vorticity in four hub-to-shroud surfaces of the impeller at point P0,P1 and P2 for: (a) 60% chord length (b) 80% chord length (c) 100% chord length (d) diffuser mid-high.

The non-uniform static pressure circumferential distribution at the impeller outlet induced by the volute tongue causes the inception of a stall region, in the location corresponding to the circumferential static pressure peak in the volute. Furthermore, that stall zone is not moving along the circumferential direction.

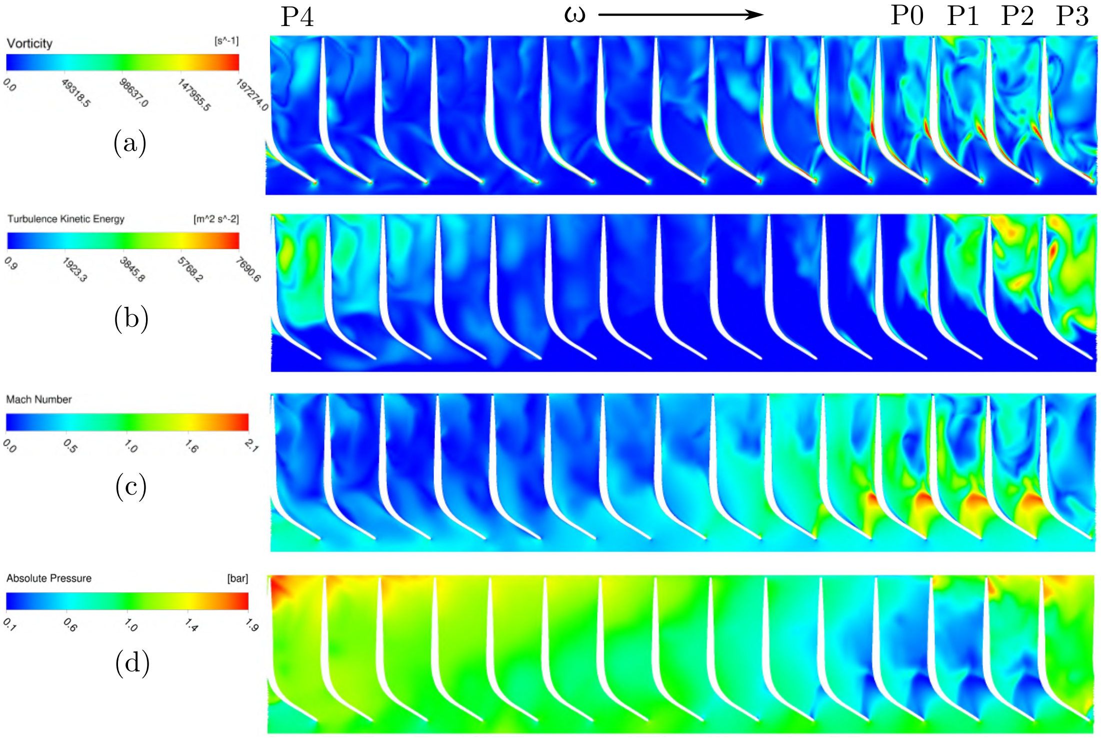

Figure 4.29: Blade-to-blade view at 80% span height of: (a) vorticity (b) turbulence kinetic energy (c) Mach number (d) absolute pressure.

A possible explanation can be formulated based on the similarities found by the study of Fujisawa at al. [34], where the stall zone is not moving along the circumferential direction because the circumferential position of the stall is dominated by the impeller outlet static pressure distribution.

The spillage vortex generated by the tip leakage flow may cause the local low static pressure zone in the blade passage (Fig.4.13) where it cannot move across the full annular due to asymmetric structure limitations.

5

Conclusions

In the presented work, a CFD analysis of a single-stage centrifugal compressor is presented. The analysis was conducted with the Demag® KG3.32 compressor serving as the reference model. Both steady and unsteady RANS simulations were performed, primarily utilizing the Ansys® CFX flow solver. Additionally, comprehensive experimental data, acquired through an ongoing research project at the test rig of the Chair of Turbomachinery (University of Duisburg-Essen), were incorporated into the analysis. The primary focus of this investigation was the determination of pressure distribution within the volute. The numerical analysis was divided into three sequential steps, commencing with the simplest single-passage geometry and culminating in the analysis of the complete annulus geometry encompassing the entire compressor.

In Chapter 4, the primary objective was to discern the probable causes of the discrepancies observed between the performance results obtained from CFD simulations and experimental data, particularly in terms of the compressor map and efficiency curves. The initial findings indicated a shift in the curves towards lower flow rates and a reduced operational range, primarily attributed to the incorporation of the volute in the setup.
Preliminary results revealed that the volute precludes choking in the entire compressor, resulting in a non-uniform pressure distribution within the volute and substantial flow recirculation in the exit-cone region. Furthermore, various analyzed setups did not consistently alleviate the mismatch issue, which was further aggravated in the 360°full annulus configuration.

Subsequently, an unsteady time-resolved simulation of a single operating point was executed across the entire domain to detect pressure fluctuations within the volute. Multiple monitoring points were strategically positioned within the volute to analyze pressure distribution, followed by similar monitoring within the impeller to investigate interactions between these two components. Pressure signals were analyzed in both the time and frequency domains, with a focus on identifying the primary frequency components.

In a specific region of the impeller characterized by high flow instabilities (cut-off region), a frequency correspondence between CFD and experimental results was observed, yet the underlying physical phenomenon remained undetermined. Moreover, alterations in flow conditions may result in varying pressure fields, leading to distinct excited frequencies within the 1340-1380 Hz range (approximately 4 times the impeller frequency). This outcome suggests a potential aerodynamic correlation of this frequency peak, rather than a mechanical origin.

In the final section, an investigation into the flow structure within the impeller was conducted to assess its interaction with downstream components. This involved the identification of primary and secondary flow patterns within the impeller, with a specific focus on the region exhibiting instability. The study revealed instances of stall behavior in certain cells when interacting with volute features, such as the tongue and exit-cone, resulting in substantial blockage effects in that region. Additionally, the findings regarding flow behavior within the impeller were compared with existing literature to identify similarities and provide potential physical explanations.

It is important to note that the reference compressor under examination in this study is considerably aged, leading to uncertainties regarding the accurate replication of the compressor due to the absence of critical information such as technical drawings and performance data. Particularly, it is impossible to confirm whether the geometry of the volute and the shape of the tongue match those used in the test rig.

Nevertheless, the investigation conducted in this thesis serves as a foundational step for future research on centrifugal compressor performance and the enhancement of the existing CFD model. Specifically, it is imperative to validate or rectify the geometric representation of the reference compressor to enhance the reliability of the CFD analysis and ensure consistent comparisons between numerical and experimental results.

CFD, therefore, offers valuable tools for gaining insights into the internal flow dynamics of the compressor. However, a notable constraint is the considerable computational time required for each transient simulation, which impeded the seamless progression of this thesis work. To address this limitation, future research should expand transient simulations to additional operating points, allow-ing for a comprehensive assessment of compressor performance across its entire operational range and the potential identification of new frequency peaks or flow patterns at various flow rates.

Bibliography

[1] Meherwan P Boyce, *Gas turbine engineering handbook*, Elsevier, 2011.

[2] Theodore Gresh, *Compressor performance: aerodynamics for the user*, Butterworth-Heinemann, 2018.

[3] Nicholas A Cumpsty, “Compressor aerodynamics”, in: *Longman Scientific & Technical* (1989).

[4] James M Sorokes, Cyril J Borer, and Jay M Koch, *Investigation of the circumferential static pressure non-uniformity caused by a centrifugal compressor discharge volute*, vol. 78620, American Society of Mechanical Engineers, 1998.

[5] R Ayder Van den Braembussche and JJ Brasz, “Experimental and theoretical analysis of the flow in a centrifugal compressor volute”, in: (1993).

[6] W Stiefel, “Experiences in the development of radial compressors”, in: *Lecture Series* 50 (1972).

[7] Van den Braembussche Ayder, “Experimental study of the swirling flow in the internal volute of a centrifugal compressor”, in: *Turbo Expo: Power for Land, Sea, and Air*, vol. 78989, American Society of Mechanical Engineers, 1991.

[8] Byron W Brown and Guy R Bradshaw, *Design and performance of family of diffusing scrolls with mixed-flow impeller and vaneless diffuser*, US Government Printing Office, 1950.

[9] Roberts Whitfield, “Alternative vaneless diffusers and collecting volutes for turbocharger compressors”, in: *American Society of Mechanical Engineers, International Gas Turbine Conference and Exhibit, 28 th, Phoenix, AZ*, 1983, p. 1983.

[10] Elias Sundström, “Flow instabilities in centrifugal compressors at low mass flow rate”, PhD thesis, Kungliga Tekniska högskolan, 2017.

[11] David Japikse, “Centrifugal compressor design and performance”, in: (1996).

[12] Erian A Baskharone, *Principles of turbomachinery in air-breathing engines*, Cambridge University Press, 2006.

[13] Robert C Dean Jr and Yasutoshi Senoo, “Rotating wakes in vaneless diffusers”, in: (1960).

[14] Benvenuti, “Aerodynamic Development of Stages for Industrial Centrifugal Compressors: Part 1—Testing Requirements and Equipment—Immediate Experimental Evidence”, in: *Turbo Expo: Power for Land, Sea, and Air*, vol. 79719, American Society of Mechanical Engineers, 1978.

[15] D Eckardt, “Detailed flow investigations within a high-speed centrifugal compressor impeller”, in: (1976).

[16] Ronald H Aungier, “Centrifugal compressors: a strategy for aerodynamic design and analysis”, in: (2000).

[17] E. Greitzer et al., “Unsteady Flow Phenomena in Turbomachines”, in: (Jan. 1990), p. 195.

[18] Nicoud Franck, “Unsteady flows modeling and computation”, in: (Dec. 2007).

[19] Sinisa Krajnovic, *The role of les in unsteady ground vehicle aerodynamics.* CMFF’12, September 2012, chap. In Proceeding from Conference on Modelling fluid flow, Budapest (Hungary).

[20] Gorazd Medic et al., “Towards Large-Eddy Simulation of Turbulent Flow in a Centrifugal Impeller”, in: vol. 7, Jan. 2011, DOI: `10.1115/GT2011-45804`.

[21] Corentin Carton de Wiart, Koen Hillewaert, and Philippe Geuzaine, “DNS of a Low Pressure Turbine Blade Computed With the Discontinuous Galerkin Method”, in: vol. 8, June 2012, DOI: `10.1115/GT2012-68900`.

[22] Stefan Wallin and Arne V Johansson, “An explicit algebraic Reynolds stress model for incompressible and compressible turbulent flows”, in: *Journal of fluid mechanics* 403 (2000), pp. 89–132.

[23] Florian R Menter, “Two-equation eddy-viscosity turbulence models for engineering applications”, in: *AIAA journal* 32.8 (1994), pp. 1598–1605.

[24] Dudley B Spalding et al., “A single formula for the law of the wall”, in: *Journal of Applied Mechanics* 28.3 (1961), pp. 455–458.

[25] Ansys CFX 18.1 documentation, “Automatic Near-Wall Treatment for Omega-Based Models”, in.

[26] Patrik P. Rautaheimo, Esa J. Salminen, and Timo L. Siikonen, in: *International Journal of Turbo and Jet Engines* 20.2 (2003), pp. 155–170, DOI: `doi:10.1515/TJJ.2003.20.2.155`, URL: `https://doi.org/10.1515/TJJ.2003.20.2.155`.

[27] Chris Robinson et al., “Impeller-diffuser interaction in centrifugal compressors”, in: *Turbo Expo: Power for Land, Sea, and Air*, vol. 44748, American Society of Mechanical Engineers, 2012, pp. 767–777.

[28] Rainer Kurz et al., “Operation of Centrifugal Compressors in Choke Conditions”, in: Feb. 2016.

[29] Hideaki Tamaki et al., “Effect of circumferential static pressure non-uniformity caused by a volute on flow in high pressure ratio centrifugal compressor with vaneless and vaned diffuser”, in: *Turbo Expo: Power for Land, Sea, and Air*, vol. 55249, American Society of Mechanical Engineers, 2013.

[30] Ce Yang et al., “Detailed measurements of the static pressure characteristics around the centrifugal compressor casing wall”, in: *Journal of Thermal Science and Technology* 12.1 (2017).

[31] D. Hagelstein et al., “Experimental Investigation of the Circumferential Static Pressure Distortion in Centrifugal Compressor Stages”, in: June 1997, DOI: `10.1115/97-GT-050`.

[32] Lee Galloway et al., “An investigation of the stability enhancement of a centrifugal compressor stage using a porous throat diffuser”, in: *Journal of Turbomachinery* 140.1 (2018).

[33] R. Braembussche, *Design and Analysis of Centrifugal Compressors*, Feb. 2019, ISBN: 9781119424093, DOI: `10.1002/9781119424086`.

[34] Nobumichi Fujisawa et al., “Generation Mechanism of Diffuser Stall in a Centrifugal Compressor with Vaneless Diffuser”, in: *Journal of the Global Power and Propulsion Society* 4 (Dec. 2020), pp. 190–201, DOI: `10.33737/jgpps/128974`.

[35] Van den Braembussche Ayder Erkan, “Numerical analysis of the three-dimensional swirling flow in centrifugal compressor volutes”, in: (1994).

[36] Carlo Cravero, “A design methodology for radial turbomachinery: Application to Turbines and Compressors”, in: *Fluids Engineering Division Summer Meeting*, vol. 36150, 2002, pp. 323–330.

[37] David C Wilcox et al., *Turbulence modeling for CFD*, vol. 2, DCW industries La Canada, CA, 1998.

[38] John D Denton, “Some limitations of turbomachinery CFD”, in: *Turbo Expo: Power for Land, Sea, and Air*, vol. 44021, 2010, pp. 735–745.